THE DESIGN OF INSTRUMENTATION AND ANALYTICAL SOFTWARE TO CHARACTERIZE LOWER LEG TEMPERATURE AS A FUNCTION OF SIMULATED PARTIAL GRAVITY IN ORDER TO OPTIMIZE FUTURE SPACESUIT DESIGN

A Thesis

by

ALEXANDRA JULIANNA HEINIMANN

Submitted to the Office of Graduate and Professional Studies of
Texas A&M University
in partial fulfillment of the requirements for the degree of

MASTER OF SCIENCE

Chair of Committee,	Bonnie Dunbar
Committee Members,	John Valasek
	Nancy Currie-Gregg
	Ana Diaz Artiles
Head of Department,	Rodney Bowersox

May 2020

Major Subject: Aerospace Engineering

ABSTRACT

For nearly 60 years, astronauts have ventured outside of their spacecraft into the extreme environment of space, performing extravehicular activities (EVAs). The astronauts are protected from the harsh environment of space, including hard vacuum, micrometeroids, and large temperature variations, by an EVA suit. A critical component of the EVA suit system is the undergarment which is used to regulate body temperature by rejecting excess heat to vacuum, called the liquid cooling and ventilation garment (LCVG). The current LCVG design used on the Space Shuttle and for the International Space Station (ISS) has not changed in more than 40 years. It was designed with the assumption that the mechanisms and body locations in which heat is rejected in the microgravity environment of Low Earth Orbit (LEO) ($1x10^{-6}$g) is equivalent to that in 1g (9.81 m/s^2) on the surface of the Earth. However, this has never been verified in LEO. Dr. Bonnie J. Dunbar, Director of the Aerospace Human Systems Laboratory (AHSL), is challenging that hypothesis based on known changes in body morphology and redistribution of body fluids responsible for heat rejection, in LEO. If the location of body heat rejection does change in LEO, changes in the design of the LCVG could lead to reduced EVA suit mass and consumables (such as circulating coolant water). Prior on orbit data indicates that the lower body (e.g. leg) is the most logical focus for the research. The purpose of this research is to design and test an instrument suite which would be used for a formal study of her hypothesis using human subjects in 1g (9.81 m/s^2), but taking advantage of previously demonstrated micro- and hypo-gravity earth-based analogs. The results of this work include trade studies of IR cameras and a 3D surface scanner, the selection of the tilt table as the microgravity and hypo-gravity analog, design of the integrated system, results from a proof of concept experiment, preliminary results for registration of the IR camera images, proposed experimental procedures and recommendations for future design optimization.

DEDICATION

To my parents for all their support through the years.

ACKNOWLEDGMENTS

My sincerest thanks to Dr. Dunbar, my advisor, for her support and guidance through grad school and on this research. I would like to thank my committee members, Dr. John Valasek, Dr. Ana Diaz Artiles and Dr. Nancy Currie-Gregg, for their support and feedback. Thank you to everyone involved with the Aerospace Human Systems Laboratory, in particular Paul Burke for his support, help in debugging code, and proof-reading.

CONTRIBUTORS AND FUNDING SOURCES

Contributors

This work was supported by a thesis committee consisting of Dr. Bonnie Dunbar, Dr. John Valasek, and Dr. Ana Diaz Artiles of the Department of Aerospace Engineering and Dr. Nancy Currie-Gregg of the Department of Industrial and Systems Engineering.

All work conducted for the thesis was completed by the student independently.

Funding Sources

This project is funded and made possible by the Texas A&M Chancellor's Research Initiative (CRI) and the Aerospace Human Systems Laboratory (AHSL) at Texas A&M.

NOMENCLATURE

ASTP	Apollo-Soyuz Test Project
Degrees of Freedom	df
CBT	Core Body Temperature
CAD	Computer Aided Design
DCM	Display and Control Module
EMU	Extravehicular Mobility Unit
EVA	Extravehicular Activity
FOV	Field of View
HDT	Head Down Tilt
HUT	Hard Upper Torso
IR	Infrared
IRB	Institutional Review Board
ISS	International Space Station
JSC	Johnson Space Center
LCG	Liquid Cooling Garment
LCVG	Liquid Cooling and Ventilation Garment
LEO	Low Earth Orbit
LTA	Lower Torso Assembly
NASA	National Aeronautics and Space Administration
NUC	Non-Uniformity Correction
PLSS	Portable Life Support System
ROI	Region of Interest

TCU	Thermal Comfort Undergarment
TMG	Thermal Mirometeroid garment
USML-1	United States Microgravity Laboratory
USSR	Union of Soviet Socialist Republics
UV	Ultraviolet

TABLE OF CONTENTS

Page

LIST OF FIGURES

FIGURE Page

LIST OF TABLES

TABLE Page

1. INTRODUCTION

1.1 Need for Pressure Suits

A well known effect of increasing altitude is a decrease in atmospheric pressure, as seen in Figure 1.1 [1], [2]. Per Dalton's Law of Partial Pressures which states that the sum of partial gas pressure equals the total gas pressure, this decrease in atmospheric pressure corresponds to a decrease in partial gas pressure of oxygen [1].

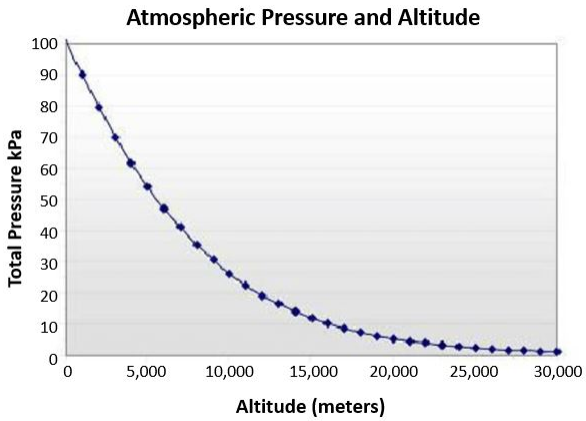

Figure 1.1: Graph of the relationship between altitude and atmospheric pressure. Reprinted from [2]

At altitudes above 28,000 ft (8,534 m, 32.9 kPa), the human body requires 100% oxygen to remain conscious [1]. Pressure breathing is required at altitudes above 43,000 ft (13,106 m, 16.2 kPa) to remain conscious [1]. As altitude continues to increase the risk of nitrogen gas bubbles forming in the body increases, commonly referred to as the bends, which can be fatal [1]. A full body pressure suit is required above 50,000 ft (15,240 m, 11.6 kPa) to minimize the risk of the bends [1]. The Armstrong Line, 60,000 ft (18,288 m) in altitude, has an average atmospheric pressure of 0.73 psi (5.04 kPa). At this pressure water boils at the average human body temperature (98.6^{o}F or 37^{o}C), including saliva and tears [1].

Therefore for a human to survive at and above these altitudes, supplemental oxygen and pressure are required, provided by a pressure suit.

1.2 Pressure Suit Development

The first known concept for a pressure garment was a submitted patent by Fred M. Sample titled 'Suit for Aviators' in July of 1918 [1]. However, the first test of a pressure suit in a hypobaric test chamber did not occur until November 16th, 1933 [1]. The tested suit was a heavily modified scuba suit developed by Mark Edward Ridge, Dr. John Scott Haldane, and Sir Robert H. Davis, that consisted of rubber and canvas sewn into an airtight coverall with a modified brass diving helmet [1]. The hypobaric test was deemed successful as Ridge, the subject, was comfortable at chamber pressures as low as 1.69 psi, that of an altitude of 50,000 ft [1].

Despite the successful testing of the Ridge, Haldane and Davis suit, Wiley Post is often considered the inventor of the pressure suit [1], [3]. Post's motivation stemmed from the desire to perform long-duration high altitude flights in his wooden fuselage airplane, Winnie Mae, but adding a pressurized cockpit would be too expensive [1], [3]. Therefore, Post turned his attention to designing a pressure suit [1], [3]. The initial design consisted of a rubber shirt and pants sealed at the waist with a metal belt [1]. However, this design leaked and did not allow sufficient mobility for flying [1]. Post eventually designed a two layer garment consisting of an inner rubber garment shaped to the body of the wearer, and an outer layer of 3-ply cloth designed to resist stretching and hold the rubber close to the body, Figure 1.2 [1]. This design is very similar to current pressure garments and extravehicular activity (EVA) suits worn by astronauts during EVA [1], [4]. Wiley Post became the first person to fly a plane in a pressurized suit on September 5, 1934, where he reported reaching altitudes of 42,000 feet over Chicago, IL, with the suit pressurized to a pressure differential of 3 psi [1].

Several other individuals were also involved in designing various pressure garments in the 1930s. For example, the Italians developed a canvas and rubber suit in 1933 designed to allow Italian Royal Air Force pilots to set altitude records [1]. In 1934, Baronessa Carina Negroni reportedly climbed to 50,583 ft in a biplane, making her the first woman to use a pressure suit [1].

Figure 1.2: Wiley Post demonstrating his fully pressurized suit in front of Winnie Mae. Reprinted from [1]

With the advent of supersonic flight, g-suits, designed to combat the physiological effects of high g-loads, were incorporated into the design of pressure suits [1].

The United States Navy continued developing pressure suits for pilots, eventually awarding a contract to B.F. Goodrich for the Mark IV, used in the 1950s and 1960s [1], [5]. This suit consisted of a two layer closely fitted garment, covering the entire body, a helmet, gloves and boots, with the inner layer of the garment consisting of an air-tight neoprene coated fabric [1]. A modified Mark IV, Figure 1.3, was selected by the National Aeronautics and Space Administration (NASA) to be the pressure suit worn by astronauts for Project Mercury [1]. This modified pressure suit was only designed for intravehicular activity [1].

Figure 1.3: Project Mercury astronauts in the modified Mark IV suits, 1960. Reprinted from [1]

1.3 Use of EVA Pressure Suit by the Soviets

On March 18th, 1965 Major General Alexei Leonov, a cosmonaut from the Union of Soviet Socialist Republics (USSR) made history as the first person to perform an EVA, lasting a total of 24 minutes during Voskhod 2, Figure 1.4, though Leonov struggled to move in his pressurized suit, the Berkut "Golden Eagle" [6]. He had difficulty reentering the inflated airlock releasing half the pressure in his suit to reenter, risking depressurization sickness and hypoxia [6], [7]. Doctors reported that his core body temperature increased by 1.8^{o}C, near the limit of heat stroke, sweat was sloshing in his suit, and he lost 6 kg [6], [7]. Despite the challenges, Leonov demonstrated the feasibility of EVAs [6], [8].

1.4 Development of US EVA Suits

Less than three months later, the first US EVA was performed by NASA astronaut Lieutenant Colonel Edward White, on June 3, 1965, Figure 1.5 [6], [9]. The EVA was performed as part of Gemini 4 and lasted a total of 23 minutes [6] [9]. During the EVA White inspected Gemini 4, tested a Hand-Held Maneuvering Unit which had 20 seconds of propellant, and attempted maneuvering using the umbilical with little success [6], [9]. Upon reentering the spacecraft, the hatch proved difficult to close, causing White to exceeded the cooling capabilities of his ventilation module and

fog to form on his visor [6]. During a two hour EVA on Gemini 9 in 1966, Eugene Cernan's exertions exceeded the cooling capabilities of his environmental life support system to remove water vapor due to sweat, fogging his face plate, effectively blinding him [6]. Three EVAs of the Gemini program were terminated prematurely due to astronauts overheating [6]. The first demonstration that a long duration, complex EVA was feasible was a two hour EVA performed by Edwin 'Buzz' Aldrin on November 13, 1966, as part of Gemini 12 [6]. Prior to the EVA Aldrin performed five training sessions in the neutral buoyancy lab and tests in the thermal vacuum chamber to become accustomed to the restricted mobility of a pressurized EVA suit, now standard practice [6]. During the EVA, his physical condition was monitored to ensure he rested when necessary to minimize fatigue [6].

Figure 1.4: Soviet Cosmonaut Alexei Leonov on March 18, 1965, during the world's first EVA on Voskhod 2. Reprinted from [7]

Figure 1.5: Edward White during the first US EVA during Gemini 4, June 3, 1965. Reprinted from [9]

1.5 Development of Liquid Cooling Garments

To prepare for EVAs on the Lunar surface, NASA developed the A7L suit [6]. This suit, unlike previous EVA suits which only relied on ventilation gas to provide cooling, incorporated a new invention under the pressure garment, the liquid cooling garment (LCG) [10]. The LCG

was developed by Burton and Collier in 1962 to cool crewmen in hot aircraft cockpits and used circulating cool water [10]. United Aircraft and Webb Associates developed a prototype LCG based on the Burton and Collier design, which was demonstrated to NASA in 1964. The addition of the LCG to the EVA suit was in part due to the overheating issues experienced during the Gemini program, and the belief that higher metabolic rates would be necessary to perform a surface EVA [6], [10]. The first test of the A7L suit was on Apollo 9, where a one hour test was performed by depressurizing and opening the external hatches of the lunar module [6]. The test was considered a success.

On July 20, 1969, Lieutenant Neil Armstrong and Colonel Edwin 'Buzz' Aldrin made history as the first humans on the moon, performing the first Lunar EVA, lasting a total of two and a half hours, Figure 1.6 [6]. The first Shuttle EVA was performed on April 7, 1983 on STS-6, by Donald Peterson and Franklin Story Musgrave [6]. The EVA was also the first EVA performed in the Shuttle extravehicular mobility unit (EMU), the first operational suit specifically built for EVA [6].

Figure 1.6: Apollo 11 astronaut Colonel Edwin 'Buzz' Aldrin on the lunar surface. Reprinted from [11]

1.6 Instrument Design Requirements

The LCG has seen very minor design changes since it was first implemented for the Apollo program and was designed to provide the necessary cooling for a human on Earth, in a 1g (9.81 m/s^2) environment. However, in microgravity a cephalad, or headward, shift of body fluids occur, which has been shown to reduce leg volume and leg blood flow. As blood circulation is the main mechanism of heat transfer within the human body, Dr. Dunbar hypothesizes that this cephalad shift will alter the locations of body heat rejection in microgravity and partial gravity. The scope of this thesis research was to develop a proof of concept instrumentation suite necessary to test this hypothesis. A tilt table will be used to simulate the effects of microgravity and partial gravity on the cardiovascular system. As the fluid shift causes a decrease in leg volume and blood flow, initial testing will focus on the lower leg. Skin temperature will be measured with an infrared (IR) camera and leg volume changes will be measured with a 3D scanner.

The tilt table shall support a weight of 180 lbs and be capable of achieving any angle between 0^o and 90^o. The IR camera and 3D scanner should mount directly to the tilt table and shall require minimal adjustment when adjusting the tilt angle. Both IR and 3D imaging of the region of interest (ROI) shall occur at each tilt angle and the IR images and 3D images will be registered.

2. BACKGROUND AND LITERATURE SEARCH

2.1 The Extravehicular Activity (EVA) Space Suit System

Space is a hazardous environment with radiation (ultraviolet (UV), gamma, and galactic cosmic rays) [12]. In low earth orbit (LEO) astronauts must be protected from man-made orbital and micrometeroid debris, a hard vacuum (5 x 10^{-10} Torr) and temperatures ranging from -250^{o}F in the shade to 250^{o}F in direct sunlight (-157^{o}C to 121^{o}C) [12]. Lunar surface hazards include lunar dust, a vacuum (2 x 10^{-12} torr), and a temperature range of -290^{o}F at night to 240^{o}F during the day (-179^{o}C to 116^{o}C) [13]. To protect themselves from this harsh environment during EVA, astronauts wear a pressurized EVA suit.

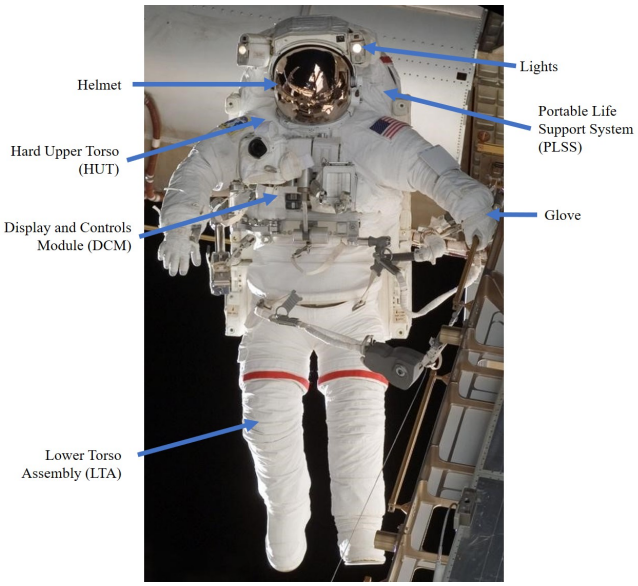

Figure 2.1: Labeled image of the NASA EMU during an ISS EVA. Modified from [14]

The current EVA suit used by NASA is the EMU, Figures 2.1 and 2.2, which was used on all Space Shuttle flights and currently on the International Space Station [15], [14]. A new suit is under development for the return to the moon [14]. The EMU consists of several major components:

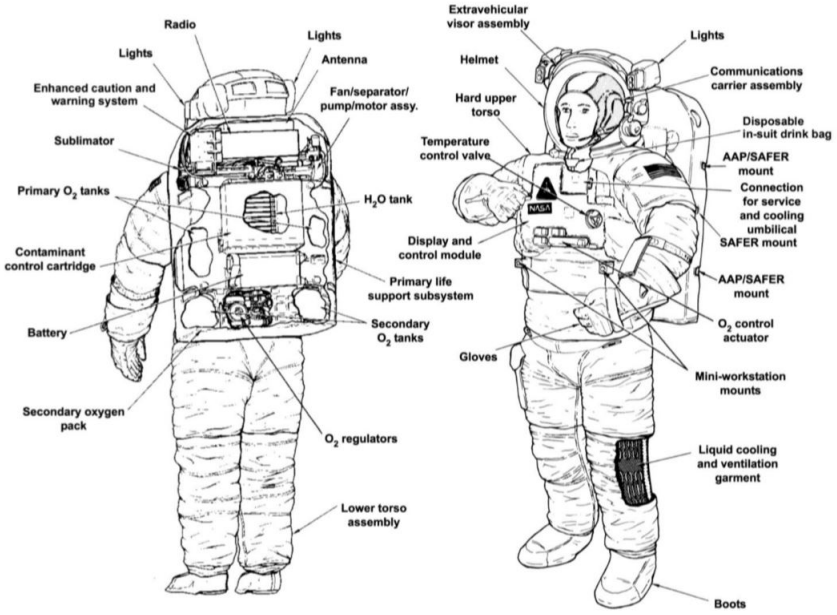

Figure 2.2: Illustration of the NASA EMU EVA suit with various components labeled. Reprinted from [15]

portable life support system (PLSS), pressure garment (including the hard upper torso (HUT) lower torso assembly (LTA), and the LCVG)) [15]. The operating pressure of the EMU is 4.3 psi $\pm$ 0.1 psi (29.6 kPa $\pm$ 0.7 kpa) of 100% oxygen [15].

2.1.1 EMU Pressure Garment

The EMU pressure garment consist of 14 layers, Figure 2.3: including two fabric layers and one tubing layer of the LCVG, the pressure bladder and restraint layer, the thermal micrometeroid garment (TMG) liner composed of Nylon Ripstop, seven layers of the TMG consisting of aluminized Mylar, and the outer layer made from a blend of Gortex, Nomex, and Kevlar which also provides fire protection [15].

The pressure bladder, impermeable to air, provides the necessary pressure to support human life, 4.3 psi of 100% oxygen [15]. This however, causes the pressure bladder to inflate and become very rigid, therefore the restraint layer is designed to minimize ballooning of the bladder [6], [15]. The seven layers of the TMG must serve two purposes: provide protection from micrometeroids

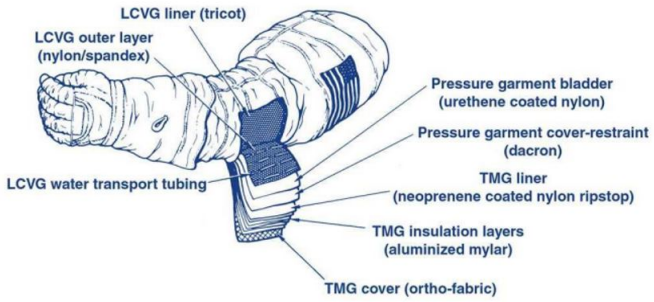

Figure 2.3: The soft goods of the EMU are composed of 14 layers, including the three layers of the LCVG. Reprinted from [15]

and provide maximum thermal insulation [15]. The outer layer provides fire protection and is designed to protect the TMG from rips and tears [15].

One major suit component, unique to the EMU, is the hard upper torso (HUT) [15]. The HUT is a fiberglass shell which provides the mounting interfaces for the majority of the EMU components including: helmet, arms, LTA, PLSS, and the display and controls module (DMC) [15]. Tubing for the cooling water and ventilation for the LCVG passes through the HUT [15].

2.1.2 Liquid Cooling and Ventilation Garment (LCVG)

The LCVG is responsible for providing cooling to an astronaut during EVA through conduction of heat from the skin to circulating cooling water, forced air convection, and sweat evaporation [10], [16].

2.1.2.1 Apollo LCG

The LCG was developed in 1962 by Burton and Collier for crewmen working in hot aircraft cockpits [10]. United Aircraft and Webb Associates presented a prototype, based on the Burton and Collier design, to NASA in 1964 to demonstrate the effectiveness of LCGs for human spaceflight [10]. The Mercury and Gemini programs utilized air circulation, though it was believed that more cooling would be required for Lunar EVAs due to higher metabolic rates from walking on the Lunar surface [10]. Therefore, the LCG was incorporated in the final design of the Apollo A7L EVA suit [10]. The Apollo LCG, shown in Figure 2.4, consisted of a Spandex over-garment with

Tygon (ethylene vinyl) tubing covering the torso, thighs, calves, and upper arms [17], [18]. Air (100% oxygen) cooling, with ducting from the helmet attached to the inner wall of the pressure garment, provided convective cooling and sweat removal [19].

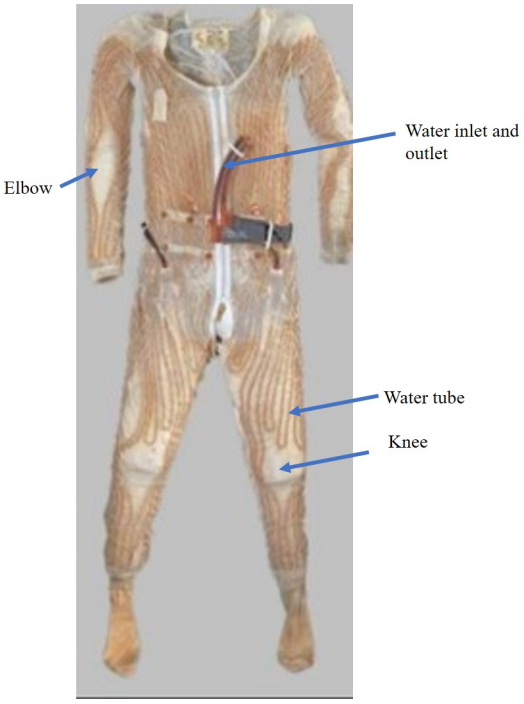

Figure 2.4: Apollo LCG with tubing covering the torso, legs and upper arms of the astronaut, 1968 to 1975. Modified from [17]

2.1.2.2 EMU LCVG

The current NASA EMU LCVG design, shown in Figure 2.5, consists of 48 Tygon tubes approximately 91.5 x 10^2 cm in length between two fabric layers, Figure 2.6 [20], [21]. Each tube has an outer diameter of 3.175 cm (1/8 in) and an inner diameter of 1.59 cm (1/16 in), with a wall thickness of 0.8 cm [20], [21]. The conductivity of the tubing is 0.252 $\frac{W}{mK}$ [22]. The tubing is evenly distributed through the entire garment, covering an astronaut from ankle and wrist to neck [23], [18]. Cooled water circulates through the tubing at a minimum rate of 1.81 liters/min with an inlet temperature ranging from 4.4^{o}C to 32.2^{o}C (40^{o}F to 90^{o}F), which is controlled by the as-

Figure 2.5: EMU LCVG A) Front and B) Back. Modified from [24]

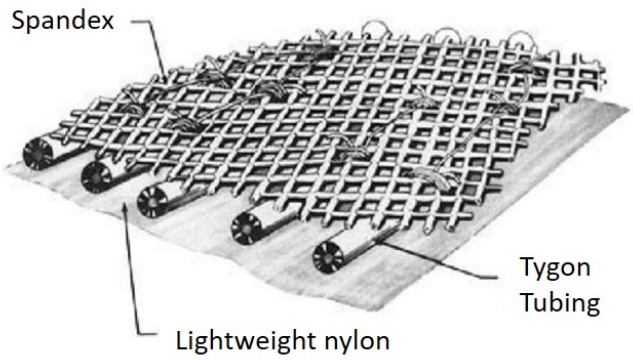

Figure 2.6: The three layers of the LCVG: lightweight nylon, Tygon tubing and spandex. Reprinted from [25]

tronauts via the temperature control valve on DCM, attached to the front of the HUT, Figure 2.7 [15], [21]. Due to the temperature differential between the circulating water and the skin, heat is conducted from the skin to the circulating water, providing sensible cooling.

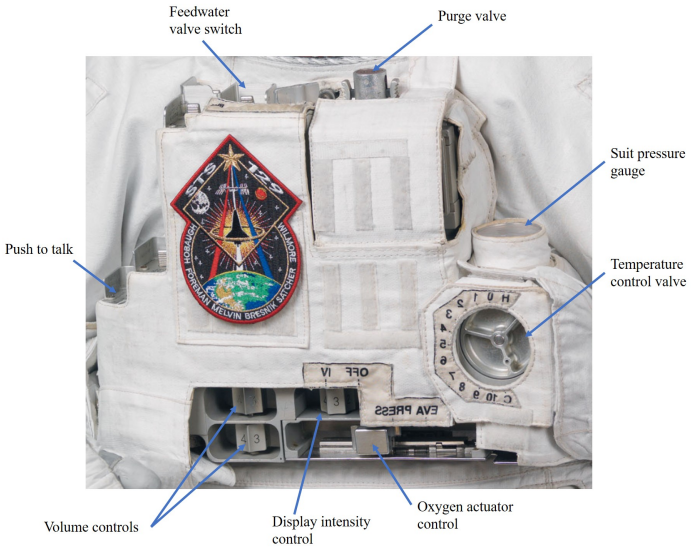

Figure 2.7: Display and Control Module (DCM) with the temperature control valve which allows the astronaut to control the temperature of the water entering the LCVG, and therefore the cooling rate. Modified from [26]

Water enters the suit through one of two manifolds above the right hip of the astronaut, Figure 2.8 A and B. The water is then separated into four separate feed tubes that attach to the garment Figure 2.8 B. Once inside the garment, each feed tube divides into 12 separate tubes that form the main tubing of the garment, Figure 2.8 C. The end of each main tube is connected to another internal manifold, Figure 2.8 C, for a feed tube that connects to the second manifold at the hip, Figures 2.8 A and B, that returns the water to the PLSS.

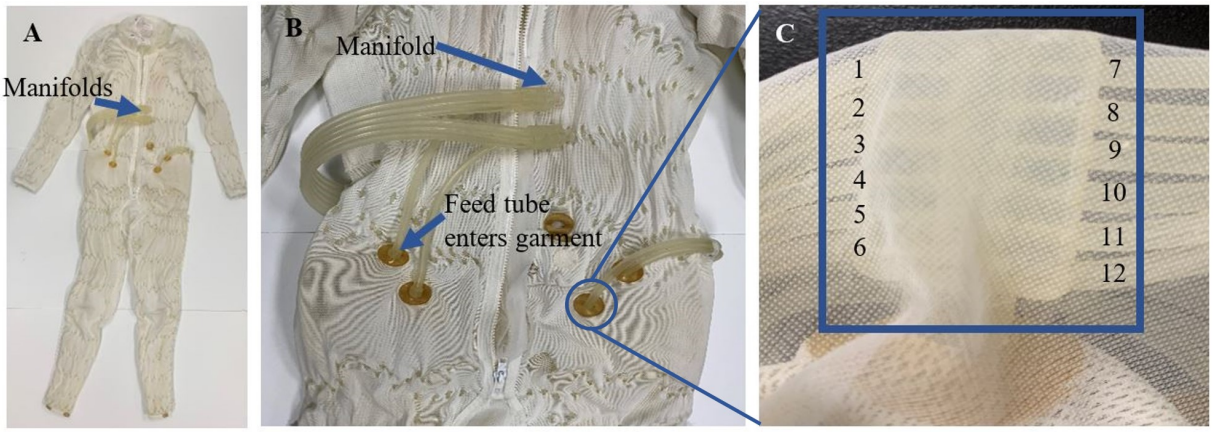

Figure 2.8: NASA surplus EMU LCVG A) Location of two manifolds and feed tubes B) Manifolds separate into 4 feed tubes that enter garment, C) Small manifold inside of garment where a feed tube is divided into 12 separate tubes

The astronaut is able to control the volume of the water that is recirculated through the garment, and therefore cooling, by adjusting the temperature control valve [15]. The remainder of the water returns to the sublimator for cooling prior to recirculation.

Oxygen is circulated from the helmet over the exterior of the LCVG, to the extremities and removed through the vent tree tubes that extend down the arms and legs and is attached to the rear of the garment [15]. The oxygen circulates at 2.83 liters/sec and at a temperature of 57^{o}F (13.9^{o}C) [15]. This circulation provides forced convective cooling and the evaporation and removal of sweat [15], [27], [16]. The EMU LCVG is capable of supporting a work rate of 580 W (500 kcal/hr) without risk of thermal stress [27].

Rhodes *et al* [21] and Koscheyev *et al* [23] report that test subject found the LCVG to be scratchy, abrasive and uncomfortable. Therefore, astronauts can elect to wear a thermal comfort undergarment (TCU) under the LCVG. However, the TCU forms an additional barrier to heat transfer [21]. Professor Dunbar stated that many astronauts benefited from this additional barrier, as they were cold when wearing only the LCVG [28], even when cooling was set on the lowest available setting, during periods of inactivity in vacuum chamber testing. Crewmembers also report being cold during ISS EVAs when they paused during periods of shadow [28]. This seemed to be particularly true for smaller crewmembers, typically female, with higher surface area to volume ratios [28].

2.1.2.3 Orlan LCG

For completeness the Russian Orlan EVA suit LCG, Figure 2.9, is included. It contains approximately 65 x 10^2 cm of flexible PVC tubing with an outer diameter of 0.5 cm [20]. The garment covers the body from the wrist to ankles, similar to the EMU LCVG, and includes a head covering hood [23], [20]. However, unlike the NASA EMU LCVG, the water cooling is provided only to the trunk, arms, thighs, and portions of the neck and head, with a focus on cooling large muscle groups [23], [20], [17]. The Orlan LCG does not include an air ventilation system but a ventilation system is likely incorporated into the Orlan suit to prevent asphyxiation [23], [19].

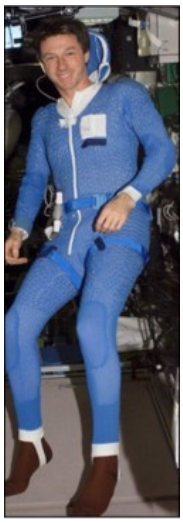

Figure 2.9: Russian Orlan LCG which includes a hood, with tubing covering the trunk, arms, thighs and portions of the neck and head. Reprinted from [17]

Table 2.1 provides a comparison the the Apollo LCG, NASA EMU LCVG, and Russian Orlan LCG.

Table 2.1: Characteristics of the Apollo LCG, EMU LCVG, and Russian Orlan LCG

	Apollo	**EMU**	**Orlan**
Number of Tubes	N/A	48 tubes [20], [21]	1 tube [20]
Total tubing length	N/A	91.5 m [20], [21]	65 m [20]
Tubing material	Tygon [17], [18]	Tygon [20], [21]	PVC [20]
Area covered by tubing	Torso, thigh, calf, upper arms [17], [18]	Entire body except hand, feet, and head/neck [23], [18]	Trunk, anterior arms, thigh, portions of neck and head [23], [20]
Total area covered	Entire body excepbt hands, feet, heat/neck [17], [18]	Entire body except hands, feet, heat/neck [23], [18]	Entire body except hands, feet, head/neck [23], [20]
Ventilation	Ducting on inner wall of pressure suit [19]	Yes, through vent tree, oxygen [15]	Not part of garment [23], [20].

2.1.3 Portable Life Support System (PLSS)

The PLSS, Figure 2.10, which attaches to the back of the HUT, is responsible for supplying the breathing oxygen to the astronaut, maintaining the suit pressure, controlling the thermal environment through the circulating oxygen and water of the LCVG, removing humidity, carbon dioxide and other contaminants from the circulating oxygen, providing communication, and monitoring system parameters [15].

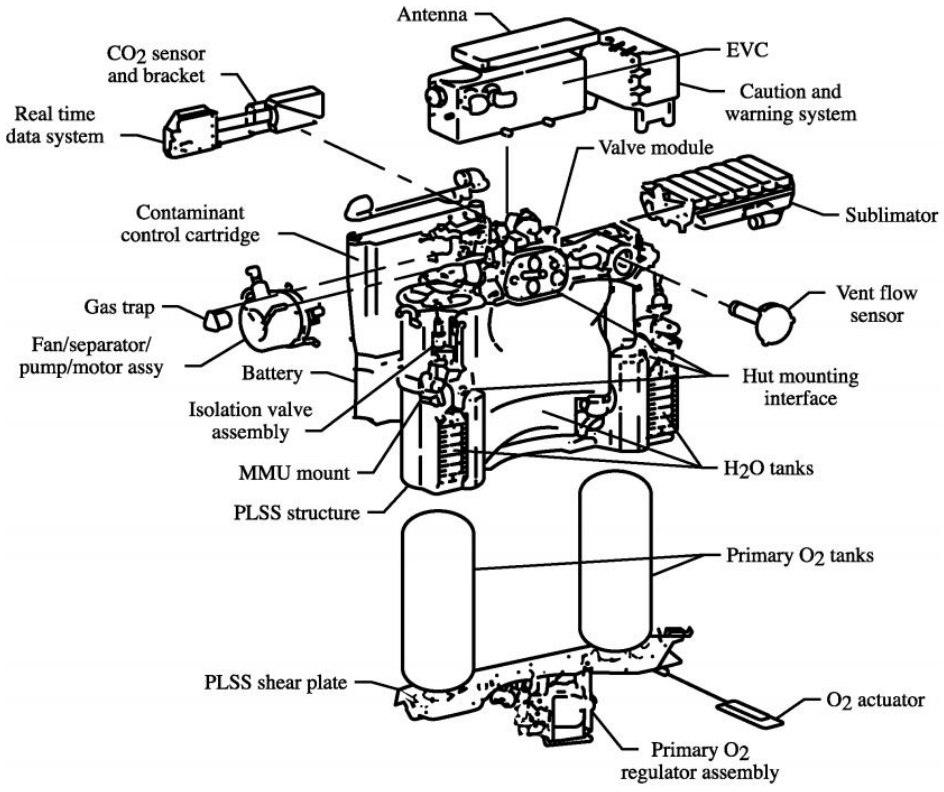

Figure 2.10: Major components of the EMU PLSS. Reprinted from [29]

Of particular interest for this research are the oxygen ventilation circuit, Figure 2.11 and liquid transport loop, Figure 2.12. The oxygen ventilation circuit provides oxygen for breathing, suit pressurization, ventilation for suit cooling, and elimination of exhaled gas [15]. After the oxygen gas passes through the suit and is filtered to remove contaminants, the gas is passed through a sub-

limator where it is cooled from 103^{o}F to 57^{o}F (39^{o}C to 14^{o}C) [15]. Water condensate is removed from the ventilation loop as it passes through the sublimator and is stored in the feedwater loop [15].

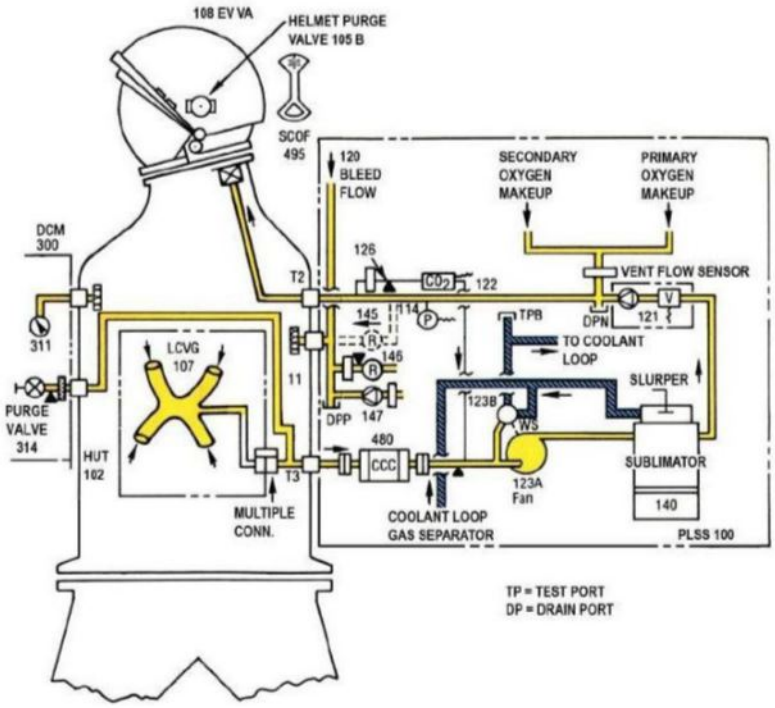

Figure 2.11: Diagram of the oxygen ventilation loop of the EMU PLSS. Reprinted from [15]. Note the oxygen entering the EMU at the helmet and removed through the LCVG vent tree. The air then passes through the containment control cartridge before arriving at the sublimator.

Similar to the ventilation system, circulating water is passed through the sublimator to reduce the temperature prior to recirculation through the LCVG. The sublimator consists of a series of feedwater fed sublimation cooled fins which convert the LCVG generated heat directly to water vapor in vacuum [15]. Sublimation is a very effective method for cooling, taking advantage of the heat of vaporization for water. However, the stored feed water in the PLSS is a consumable which limits the length of an individual EVA, as an average of 1 kg of water is vented to space for four hours of EVA, with the PLSS capable of carrying a total of 10 lbs (4.5 kg) of feedwater [16], [15].

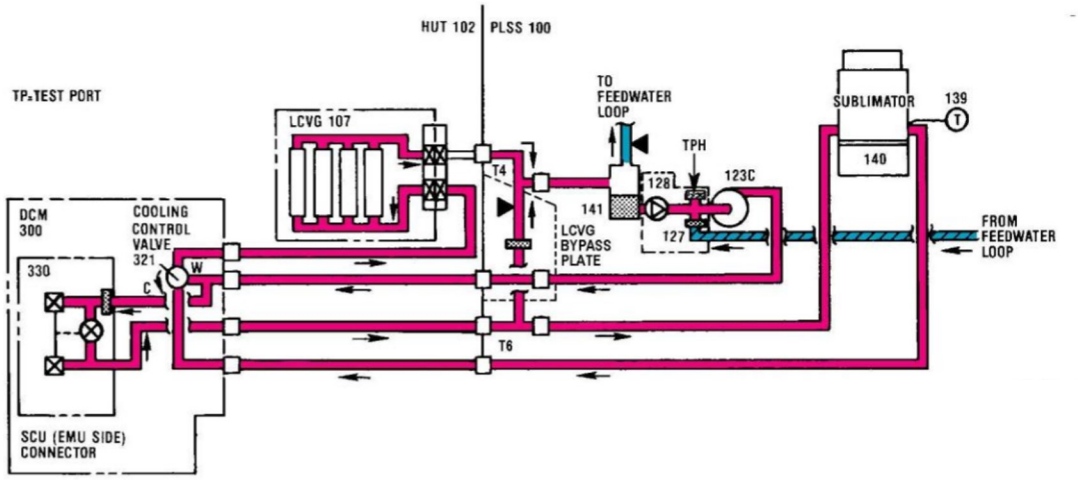

Figure 2.12: Diagram of the cooling water loop of the EMU PLSS. Reprinted from [15]. The water passes through the LCVG, to the temperature control valve on the DCM. The portion to be cooled, continues to the sublimator in the PLSS prior to recirculation

2.2 Human Thermal Management Physiology

The body continuously produces heat as a byproduct of chemical reactions, primarily from the liver, brain, heart, and working muscles [30], [31]. The human thermoregulatory system maintains the core body temperature (CBT) within a set range, 36^{o}C to 38^{o}C (96.8^{o}F to 100.4^{o}F) [30], [31]. Large deviations from the 2^{o}C temperature range (CBT < 33^{o}C or CBT > 40^{o}C) can result in life threatening conditions: hypothermia, heat stroke, and hyperpyrexia [32], [31], [30], [33]. To maintain CBT the body regulates the heat lost to or gained from the environment through the circulation of blood, which carries the heat from the core and working muscles to the skin [30], [31]. The primary mechanisms for body heat rejection are shown in Table 2.2: (1) radiation accounts for up to 60% of total heat rejection with (2) evaporation, (3) convection, and (4) conduction accounting for the remainder [30].

Table 2.2: Mechanisms of heat loss for a human at rest in a thermoneutral 1 g environment [30]

Heat transfer mechanisms	**Percentage of heat lost**
Radiation	60%
Evaporation (sweat and respiration)	22%
Convection	15%
Conduction	3%

2.2.1 Radiation

All objects above absolute zero emit thermal radiation, the strength of which is dependent on the object's surface temperature [34]. Radiation, unlike convection and conduction, does not rely on matter to transfer energy but instead uses electromagnetic waves,with a wavelength of 760 x 10^{-7} cm to 0.1 cm, and occurs most effectively in vacuum [34], [35]. Emissivity (ϵ) is a surface property ranging from 0 to 1, and refers to the ratio of energy released by the surface to the max theoretical energy released, determined by the object's temperature [34]. The accepted emissivity of dry clean human skin is reported to be 0.98, and is therefore near that of a blackbody [36], [37], [35], [38], [39].

2.2.2 Convection

Convection is the transfer of heat into a fluid from both the random motion of molecules, similar to conduction, and the bulk motion of the fluid [34]. A thermal boundary develops along a surface similar to the velocity boundary layer due to viscosity [34]. There are two types of convection: free and forced convection. Free (i.e. natural or gravity-induced) convection is naturally occurring, allowing for air circulation due to buoyancy forces caused by the density differences between air masses of varying temperatures [34]. Hot air is less dense than cooler air, and rises, allowing for the cool dense air to descend [34]. However, without gravity, buoyancy forces, and therefore free convection, cannot occur [40]. The lack of free convection in microgravity allows a layer of warm air to form around a warm object, such as an astronaut, as heat is transferred through conduction to the stationary air layer. Forced convection, unlike natural convection, does not require gravity,

as it relies on moving air [34]. In microgravity, forced convection can still occur, and must occur to prevent a layer of carbon dioxide of forming around the astronauts head, but has both mass and power requirements.

2.2.3 Conduction

Conduction is the heat transfer due to the random motion of molecules, such as vibration of atoms in the lattice network of a solid [34]. Higher temperatures correspond to higher energies and faster vibrations or random motion of molecules. This energy is transferred from molecule to molecule due to the vibration of bonds or collisions, from higher to lower energy and therefore higher to lower temperatures [34].

2.2.4 Variation in Localized Heat Transfer of the Body

A study performed by the University of Minnesota, in conjunction with NASA Johnson Space Center (JSC), showed that, in a 1g (9.81 m/s^2) environment, the lower body had a lower heat exchange rate than its large surface area would indicate [41]. It is hypothesized that this is due to the large muscle groups in the legs which have a lower conductance than other tissue, and less superficial blood flow than other body regions [41]. The same study showed that the torso and hands have the highest physiological ability to absorb or reject heat [41]. The lower body (thigh, shin, calf, and foot) has lower skin temperature values than the torso, head, and arms for a human at rest in a thermoneutral environment (an environment where the net heat transfer from the body is zero, on average an atmospheric temperature of 26^{o}C to 27^{o}C) in a 1g (9.81 m/s^2) environment [42], [43].

2.3 Human Anatomy of the Lower Body

Figure 2.13 shows the network of arteries and veins of the leg. Arteries are the vessels which carry the oxygenated blood from the heart to the extremities and are deep vessels [44]. From the arteries, blood flows into capillaries which provide the blood flow to the dermis, or skin [30], [31]. Heat conducts through the walls of the capillaries, and the layers of the dermis and epidermis to the skin surface [30]. When the body is overheated, capillaries dilate to allow more more blood

flow to the dermis and during periods of cold, heat is preserved at the core by constricting dermis capillaries [31], [45]. The capillaries then connect to a series of superficial and deep veins, which carry the blood from the dermis and returns it to the heart [31], [46], [47]. The superficial veins, such as the great saphenous vein which passes anteriorly to the medial malleolus and the small saphenous vein which passes the lateral malleolus, run through the subcutaneous tissue [46], [48]. The deep veins often run parallel to the arteries, such as the femoral vein in the thigh, and anterior tibial vein [44], [46], [47]. A general diagram of cutaneous circulation is shown in Figure 2.14.

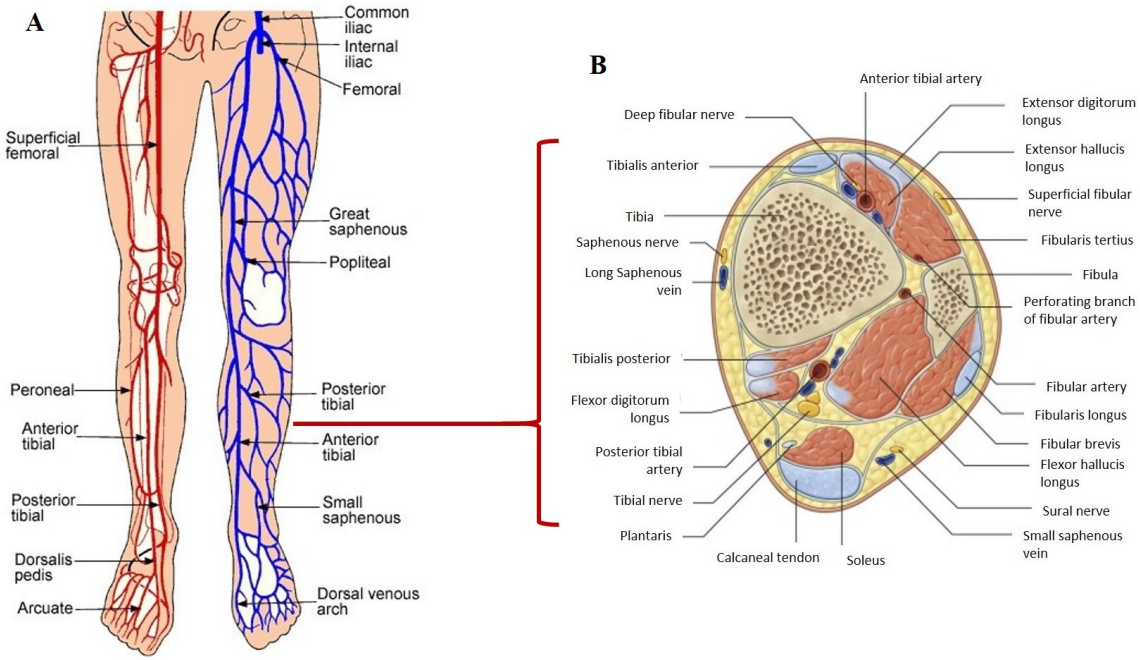

Figure 2.13: A) Vessels of the leg , B) Cross section of the lower leg. Reprinted from A) [49] and B) [47]

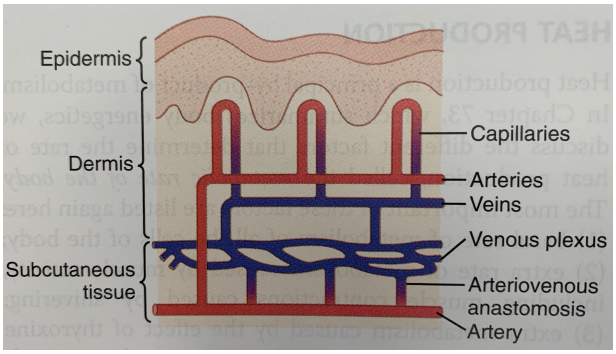

Figure 2.14: Diagram of general cutaneous circulation. Reprinted from [30]

2.4 Microgravity Effects on the Human System: The Fluid Shift and Fluid Loss

2.4.1 Cardiovascular Pressure Changes

One effect of microgravity on the human body is the cephalad, or headward, body fluid shift, which can be observed nearly immediately upon exposure to microgravity. During the first day, astronauts exhibit puffy faces. Fluid, including blood, that normally pools in the legs due to the pull of gravity, shifts headward into the chest cavity and head [50]. Figure 2.15 illustrates the fluid redistribution and changes in intravascular pressure due to loss of hydrostatic pressure which is due to the weight of the fluid, in microgravity compared to a 1g (9.81 m/s^2) environment [51]. The hydrostatic column can exert a pressure differential as high as 130 mmHg between the feet and head of a standing person in 1g (9.81 m/s^2), compared to the equal pressure across the body of microgravity [52]. The increased pressure in the chest cavity and head activate a series of physiological responses which result in an increased water output from the kidneys for the first several days in microgravity [53]. This results in a subsequent decrease in total fluid volume of 1.5 to 2 liters, which is most evident in the legs [54].

2.4.2 Changes in Lower Body Volumes as a Function of Microgravity

Several different flight experiments, starting with Skylab, and Earth-based analogs have recorded a leg volume decrease in microgravity [55], [51], [56], [57], [58], [59], as well as a decrease in leg blood flow [60], [61]. An average dominant (non-dominant) leg volume decrease of 0.808 liters (1.090 liters), 10.8% (14.8%), compared to preflight levels was reported for the three crewmem-

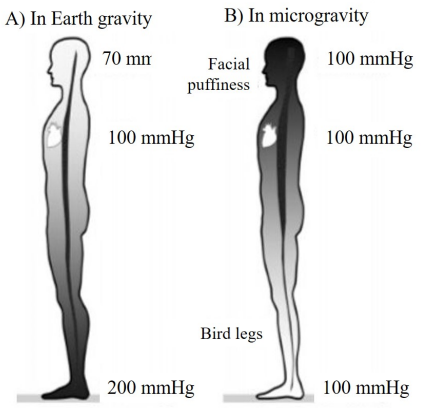

Figure 2.15: Fluid redistribution A) in Earth gravity compared to B) microgravity. Reprinted from [52]

bers of Skylab 4 [51]. It was also reported that a shift of approximately equal magnitude for both the thigh and calf in microgravity occurred, though the change in cross sectional area was larger for the calf due to its smaller dimensions [55]. During the Apollo-Soyuz Test Project (ASTP), all three crewmembers reported a decrease in leg volume of 5% to 10% compared to preflight levels within 32 hours in flight [56]. Shuttle leg volume decrease was reported at an average of 1.026 liters (11.6% per leg), as measured by stocking plethysmograph compared to preflight supine level, higher than both Skylab and ASTP. Figures 2.16 and 2.17 show a stocking plethysmograph, which is used to record leg circumference at fixed locations [57]. The volume is calculated based on these circumferences by treating the leg as a series of truncated cones [57]. Figure 2.18 shows astronaut Larry De Lucas wearing the stocking plethysmograph on United States Microgravity Laboratory 1 (USML-1) (STS-50) in 1992. The majority of the volume loss was seen from the thigh (63.2% of the total change, 0.619 liters) as compared to the lower leg (36.8% of the total change, 0.279 liters) [57].

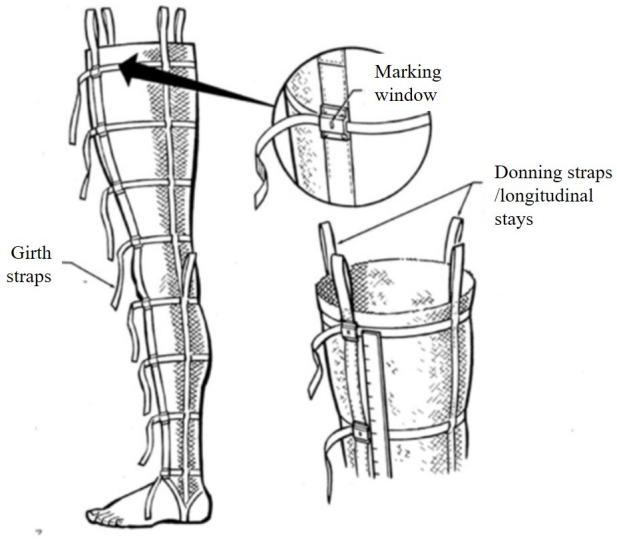

Figure 2.16: Illustration of the stocking plethysmograph. Reprinted from [51]

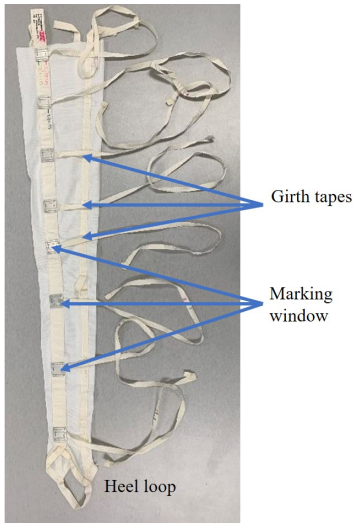

Figure 2.17: NASA stocking plethysmograph

Figure 2.18: Astronaut Larry DeLucas wearing stocking plethysmograph on United States Microgravity Laboratory 1 (USML-1) (STS-50) in 1992. Reprinted from [62]

Impedance was used on a Mir flight and recorded a decrease of 15.3% in thigh circumference, and a volume reduction of 1.6 liters and 1.8 liters from the calf and thigh respectively [63]. Louisy reported a decrease of 0.100 liters from the leg within the first 24 hours of bed rest, with a final average leg volume decrease of 13% by the 41st day of the study [59]. Watenpaugh reported a decrease of 41% in resting calf blood flow in microgravity for four to 12 days, compared to

preflight supine levels as measured on Space Lab Life Sciences 1 and 2 (STS-40 and STS-58) on a total of seven subjects [60]. A 4-hour bed rest study performed by Panferova and Kabesheva from the USSR reported, in 1987, the blood influx to the thigh decreased 21.2% for a supine subject compared to ambulatory baseline values [61]. Table 2.3 presents a summary of the volume changes.

Table 2.3: Summary of leg volume changes in microgravity [55], [56], [57], [63], [59]

Authors	Year	Flight	Method	Results
W. E. Thornton et al	1977	Skylab 4	Series of 25 circumferences	Decrease in dominant (non-dominant) leg volume of 0.808 L (1.09 L) or 10.8% (14.8%). Equal volume was lost from the thigh and lower leg
G. W. Hoffler et al	1977	Apollo-Soyuz Test Project	Series of 12 circumferences	Average leg volume decreae of 5% to 10%
T. P. Moore and W. E. Thornton	1987	Shuttle (STS-7, 8, 51-D, 51-B, 61-B)	Stocking plethysmograph	Average leg volume decrease of 1.026 L (11.6%) with 63.2% of the loss from the thigh and 36.8% of the loss from the calf
F. J. Baisch	1993	MIR	Impedance	Recorded a loss of 1.6 L from the calf and 1.8 L from the thigh, 15.3% decrease in thigh circumference
F. Louisy et al	1997	N/A	Optoelectronic sensor plethysmograph	Average decrease of 0.1 L within the first 24 hours of bed rest, total volume decrease of 13% over 41 days

2.5 Microgravity Analogs

Several different Earth-based analogs for microgravity exist to facilitate studying the effects of microgravity on the human body, including bed rest, parabolic flights, and tilt table. Each method minimizes the G_z loading, the force of gravity along the subject's spine, for varying time periods.

2.5.1 Bedrest

Before the 1970s, the majority of bed rest studies were conducted with the subject lying horizontally. However, the use of 6^o head down tilt (HDT) has grown in prevalence with the majority of modern tests conducted using HDT [64]. The difference in fluid distribution between the two bed

rest analogs is shown in Figure 2.19. However, some in the research community are reevaluating the use of HDT as the cardiovascular pressure distribution in flight is 0 mmHg, not the -10 mmHg seen in HDT, per a personal conversation with Dr. John Charles, recently retired Associate Director of Exploration Research Planning, and former Chief Scientist for NASA's Human Research Program.

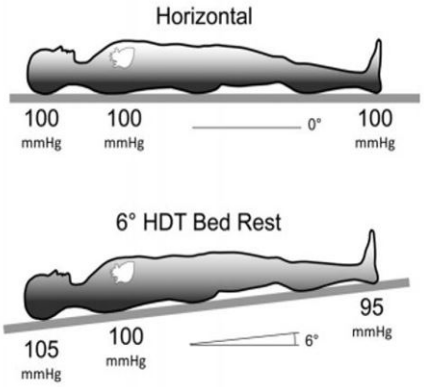

Figure 2.19: Fluid redistribution in horizontal and 6^o HDT bed rest. Reprinted from [52]

Acceptance of HDT was driven by several studies from Roscosmos, the Russian space agency [65], [66]. These studies reported, for some subjects, similar discomforts to those of astronauts and cosmonauts during the first several days of spaceflight, including: head-fullness, nasal congestion, spatial illusions, and symptoms of motion sickness [66], [65]. However, a joint United States and USSR study in 1979 reported that although both HDT and horizontal subjects showed a significant drop in lower leg volume ($p < 0.05$), the difference between the two groups was not significant [67]. Deconditioning and recovery exercise responses for HDT more closely replicated findings from spaceflight [67]. Alternatively, HDT did not show a significantly greater decrease in plasma volume, red cell mass, or blood volume [67]. Both horizontal and HDT bed rest allow for long duration mission simulation, anywhere from an hour to several weeks, with the longest reported bed rest duration of 370 days in 1986-1987 in the USSR [68]. Long duration bed rest studies, beyond studying the effects of the fluid shift, have included characterizing the drop in bone density,

change in bone architecture, and increase of calcium in urine, all of which are seen in flight [52].

2.5.2 Parabolic Flights

Parabolic flight exposures are about 20 seconds of microgravity followed by a 2g (20 m/s^2) pull out. During a parabolic flight, an aircraft flies a steep parabolic flight path, a pitch of 47^o for microgravity, varying in both altitude and speed [69]. During the peaks of the parabola, 20 seconds of microgravity, or if desired partial gravity, can be achieved, conversely, at the bottom of a parabola 40 seconds of 1.8g to 2g are produced [69]. The majority of parabolic flights include 30-40 parabolas [69]. Parabolic flights provide actual microgravity environments, unlike other analogs which simply reduce the G_z component of gravity. However, the short intervals of microgravity followed by periods of hypergravity restrict the types and duration of possible experiments [69]. Most physiological experiments conducted on parabolic flights have rapid physiological responses, such as eye pressure as measured by a tonometer.

2.6 Microgravity and Partial Gravity Analog: Tilt Tables

Tilt tables are short term experiment platforms which are used in hospitals to evaluate cardio-vascular health. Bed rest and HDT minimize the G_z loading with respect to gravity [64]. Partial gravity levels can be simulated by adjusting the angle of the tilt (θ), and therefore G_z loading, as shown in Figures 2.20 and 2.21 and Equations 2.1 and 2.2.

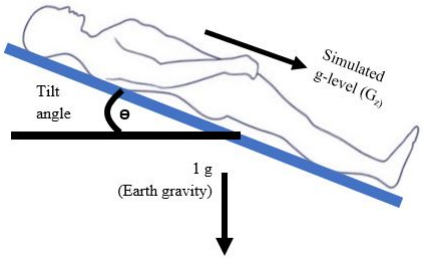

Figure 2.20: Effective g level, G_z, as a function of tilt angle

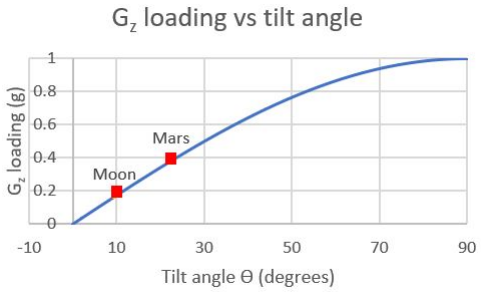

Figure 2.21: Graph of G_z loading as a function of tilt angle

$$sin^{-1}(G_z) = \theta \tag{2.1}$$

$$sin(\theta) = G_z \tag{2.2}$$

A tilt of 9.5^o, as measured from horizontal, creates a G_z loading of 1/6 g (1.62 m/s^2), that of Lunar gravity [69]. Similarly, 22.4^o creates a G_z loading of 3/8 g (3.71 m/s^2) to simulate Martian gravity [69].

A tilt table will allow measurements of skin temperature as a function of tilt angle, in order to determine if there are any thresholds and to define resulting parametric relationships.

2.7 Infrared (IR) Thermography

IR light is emitted by all objects through radiation, and therefore can be used to determine the surface temperature of an object [35]. This method is particularly effective for determining skin temperature values, which has been shown to be useful in evaluating blood flow and diagnosing diseases such as diabetes more accurately than the standard methods [70], [35], [37], [71], [22], [72], [73]. As previously stated, the accepted emissivity of human skin is 0.976 ± 0.006, [70], [35], [71], [37], [74], [75]. It should be noted that this value is only valid for clean, dry skin, as it has been demonstrated that a substance, such as a gel or water, on the skin causes a change in emissivity as more energy is reflected from the skin, though Tanda [36] reported a near constant emissivity which was unaffected by sweat [35].

Many different factors must be considered when using IR thermography due to their influence on skin temperature. The circadian rhythm influences skin temperature, with peak values measured at approximately 3 pm, with the largest variation in the extremities and the smallest variation in the trunk most likely due to the major organs being the main heat produces for a subject at rest [71]. Exercise can also affect skin temperature. Reports of skin temperature during a run and ergometer bike exercise both showed a drop in skin temperature with exercise and a rapid increase once exercise ceased, typically in the form of hyperthermal spots, as shown in Figure 2.22 [36], [70]. Beckmann *et al* reported an increase in skin temperature with exercise, however, the

subject was asked to remain still for the images to be taken, and were therefore at rest, allowing for vasodilation to occur and higher skin temperatures [76]. Consuming alcohol, eating, smoking, room temperature and relative humidity can also impact the IR readings [37], [75], [77].

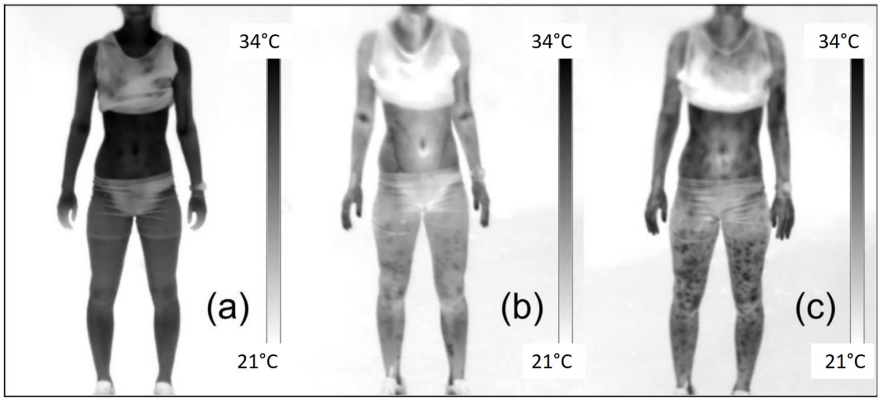

Figure 2.22: IR images of a subject: a) prior to running exercise b) immediately after end of run c) during recovery from exercise. Reprinted from [36]

There has been some discrepancy on the accuracy of IR technology versus the more traditional contact measuring devices such as thermistors and thermocouples. A 2015 report analyzed the results of 16 studies and advises against IR thermography as there was insufficient agreement between measurements from IR and contact devices, however the authors also state that there was a high risk of bias and the conclusions many not be definitive [38]. A 2007 study by Buono *et al* showed a high correlation between an IR thermometer and contact thermometer at both rest and during exercise, with r values of 0.95 and 0.98 respectively [39]. The r value indicates the strength of a linear relationship between two parameters, with an r of -1 indicating a perfect negative linear relationship, and an r of 1 indicating a perfect positive linear relationship. Matsukawa *et al* reported, in 2000, that infrared thermometers were comparable to a thermocouple to measure changes in skin temperature [78]. A study of 16 healthy young men showed that IR cameras had a high reproducibility within a short time frame, but day to day measurements were much more variable, with the largest variability in the extremities and the lowest in the core [79]. The authors state that there may be several causes for the variability including structural asymmetry and insuf-

ficient time for thermo-equilibrium to be achieved [79]. Nor does the paper specify if the images were taken at the same time of day to rule out the effects of the circadian rhythm [79], [37].

One large advantage to IR cameras over contact devices is that the IR camera allows for temperature data to be collected over an entire surface area and not just at predetermined point values. This allows for a full temperature distribution of the leg to be acquired with a few images and to determine areas of altered heat transfer.

2.7.1 IR Camera Accuracy

The most common reported accuracy for an uncooled IR camera is $\pm 2^o$C or 2%, with the best reported accuracy for an uncooled camera of $\pm 1^o$C or 1% [80]. This accuracy is determined by performing a root-sum-of-squares analysis that includes all the partial errors of the terms used in the temperature measurement equation, including: emissivity, reflected temperature, atmosphere temperature, and calibrator temperature accuracy [80]. In many cases, particularly indoors or less than 20 m outside, a much higher accuracy is achievable [80]. The actual accuracy of the resultant images can also be improved by setting the correct emissivity for the object to be imaged, setting atmospheric temperature and relative humidity, setting distance, and allowing the camera sufficient time to warm up prior to the first image being taken [80]. Despite the accuracy of $\pm 1^o$C, this does not mean that two pixels imaging an object at the same temperature would record temperatures 2^oC apart, only that the reported value will be accurate within 1^oC. To prevent drift in pixel temperatures recordings, the camera will automatically normalize the temperature readings of all pixels through a process called non-uniformity correction (NUC) [81]. The NUC process involves the camera software correcting pixel temperature values recorded of an internal screen of uniform temperature [81]. Therefore IR accuracy is critical in cases where the absolute temperature is the main focus, but in cases where the focus is variation in temperature, such as checking wire insulation, IR sensitivity is critical [80], [81].

2.8 3D Scanning of Skin with Portable Scanners

Similar to IR thermography, as the technology becomes more readily available, interest in the use of 3D scanning of the human has increased, particularly in the use of 3D scanners in the medical and attire industries. For example, quantitative descriptions of feet are highly useful, as they can be used by the footwear industry in the design of new shoes, to assist in creating insoles, and in the assessment of foot deformities such as those caused by rheumatoid arthritis [82]. A study of the 3D scans of the feet of 2,876 children (aged 2 to 14) was performed to create a new categorization for children's feet as they differ from adult feet [82]. A set of five measurements were made on each 3D scan, chosen as they are important to the fit of a shoe and not highly correlated [82]. The feet were classified, within a shoe size, as slender, intermediate or robust [82]. As anticipated, as the shoe size increased the foot narrowed [82].

3D scanning has also grown in the medical industry, particularly for prosthetic and orthotics. The particular scanner to be used varies based on the application [83]. The Artec EVA is considered a high-end, versatile, handheld scanner, capable of being used to assist in designing prosthetic covers, braces for the spine and limbs, and more precise applications such as prosthesis for the head and face where more detailed 3D images are required [83]. The use of 3D scanning to produce a prosthetic ear and nose was evaluated and showed that the scanning system was capable of accurately capturing overall anatomical form, but was not able to detect the details of delicate skin folds, wrinkles and texture [84]. However, another study that compared the use of 3D scanning (Artec MH scanner) to photogrammetry, showed that the 3D scanner, though more expensive was a much more accurate and efficient system and did not require carving anatomical details into a 3D model as is required with photogrammetry [85].

2.9 Image Registration

While IR images provide a 2D representation of the temperature distribution of a 3D object, image registration of the IR images to a 3D image of the object can allow for a 3D representation of surface temperature. Image registration involves determining a transformation between two

separate images that can relate corresponding features of an image to a second image [86], [87]. Once images have been registered, information pertaining to the intensity (ex. temperature) of corresponding features can be mapped onto the second image [86]. The majority of the medical literature focuses on registering 3D to 3D images, such as magnetic resonance imaging (MRI) and computed tomography (CT) [88], [87]. Many registration methods relay on landmark matching either using an extrinsic or intrinsic method [87], [86], [88]. The extrinsic method uses foreign, highly visible objects as landmarks, such as glued on landmarks, and are computationally efficient and easily automated [88], [87]. The intrinsic method uses pre-existing landmarks (ex anatomical landmarks) such as edges and curves [88], [87]. The issue with intrinsic matching is the method often requires the user to select the corresponding landmarks which can lead to inaccuracies in the transformation [87], [89], [90].

Several different transformations exist dependent on the number of degrees of freedom (DOF) within the transformation. The simplest transformation is that of a rigid body which is useful for features that do not distort or deform [88], [86]. A rigid body transformation consists of six DOF, three translations and three rotations, and is most applicable in the vicinity of bone, such as the spine and skull [86], [88]. An affine transformation has 12 DOF: six DOF of a rigid body transformation, three DOF from scaling factors in each direction, and three DOF to correct for image skewing or shearing [86], [88]. Transformations can also be global, applied to the entire image, or local, applying to a subset of the full image [87].

There has been some research in 2D/3D registration, specifically looking at the registration of an IR image on a 3D surface. A method was developed that applied IR data to the edges of MRI slices of the leg and face [90], [89]. This method stacked a series of MRI slices and created a 2D projection of the imaged object at four 90 degree angles (0^o, 90^o, 180^o, and 270^o) [89], [90]. IR images (Agema Thermovision 470 and FLIR ThermaCAM P65HS) of the object were taken at the same angles [89], [90]. A series of six reference points were selected on the edge of the MRI projections, with corresponding point selected on the IR images [89], [90]. An affine transformation was determined that aligned the reference points, which resized the IR image to

match the MRI projection [89], [90]. The IR data was then, line by line, added to the MRI slices [89], [90]. The issue with this method is that selected reference points manually is a very difficult task, particularly as the reference points are not clearly defined in either image set [89], [90].

Doremalen *et al* developed a method to register IR images to 3D images of subjects' feet to help detect inflammation due to diabetic foot disease [91]. The method uses a 3D imaging device that uses photogrammetry to stitch together digital images from three separate cameras to create a 270^o model of the foot. IR cameras (FLIR One for Android) were placed with the digital cameras and aligned to have the same field of view. A set of four corresponding boundary points, visible in both the IR and digital texture map of the 3D image, were identified. An affine transformation was determined for each foot in each of the image frames (a total of six transformations) to align and size the IR image to that of the 3D image texture map. The transformed IR images were saved and applied to the 3D image as a texture map [91]. There were several errors detected with this method in that background temperatures and colors were seen in the IR texture map on the boundaries and fault lines [91]. Similar to the IR to MRI registration method, this method relied on manually selecting corresponding points between the two images which, as previously mentioned, is a very difficult task [91], [90], [89].

A method of IR to 3D image registration that does not rely on matching corresponding points was developed by Dr. Chromy [92]. This method relies on knowing the exact location of the IR camera relative to the origin of the 3D image, several camera parameters, including the camera field of view and focal distance, the direction the camera is pointed, and up in the image frame [92]. This is used to determine the location of the image corners in space [92]. The vector between the camera and each point on the 3D model is tested to determine if it is within the camera field of view and not blocked by other points of the model (ie. on the other side of the imaged object) [92]. If the point is found to be visible to the camera, the corresponding location on the IR image is determined and it's temperature value assigned ot the 3D object point [92]. Another benefit of this method compared to the others presented is that it can work with any instrument set-up.

3. METHODOLOGY

3.1 Human Body Region of Interest

The region of interest (ROI) chosen for an initial subject test was the right lower leg, specifically from the inferior edge of the patella (knee) to the medial malleolus (ankle), Figures 3.1 and 3.2. This region was chosen due to the fluid shift out of the leg, which, due to the smaller dimensions of the lower leg compared to the thigh, will have a larger cross sectional area and surface area change [55], [51], [56], [57], [58], [59], [61].

Figure 3.1: ROI chosen: right lower leg

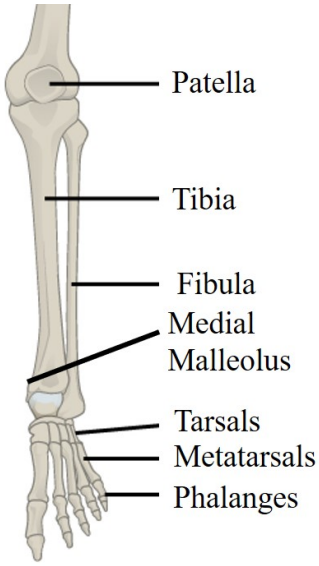

Figure 3.2: Reference of the bones of the lower leg. Modified from [93]

3.2 Hardware Selection

3.2.1 System Requirements

The requirements of the instrument suite and software are listed in Table 3.1.

Table 3.1: List of requirements and rationale for the instrumentation and software

Number	Requirements	Rationale	Met
1	Tilt Table shall at a minimum support a weight of 180 lbs	Ensure the safety of the subject and operator	Yes
2	Tilt table shall be capable of achieving any angle between 0° and 90°	The test range to simulate microgravity, partial gravity, and an Earth baseline is 0° to 90°	Yes
3	Selected instruments should mount directly to tilt table	Ease of use for the operator, ensure as consistent of measurements between subjects as possible	Yes
4	Mounted instruments shall require minimal adjustment when adjusting tilt angle	Ease of use for the operator, ensure as consistent of measurements between subjects as possible	Yes
5	3D imaging of the ROI shall occur at each test angle	Measure changes in volume as a function of tilt angle	Yes
6	IR imaging of the ROI shall occur at each test angle	Measure changes in skin temperature as a function of tilt angle	Yes
7	Registration shall be performed of the IR images to the 3D images	Determine underlying physiology of regions of varied heat transfer	Yes

3.2.2 IR Camera

Two different IR cameras from FLIR were used in this project, a FLIR E60 and FLIR T650sc, selected after an extensive trade study. Both IR cameras' detector consists of an uncooled microbolometer, which adsorbs wavelengths in the IR spectrum, 7.5 x 10^{-7} cm to 14 x 10^{-7} cm [94], [95], [96]. This heats the detector, varying the electrical resistance [96]. This variation is converted to temperature based on the inputted parameters including: distance, emissivity, room temperature, relative humidity, and reflected temperature [94], [95], [96]. The final images are saved as JPEGs.

3.2.2.1 FLIR E60

In order to determine the requirements for selecting an IR camera for the human subject test, a FLIR E60 IR camera, Figure 3.3, was borrowed from the Texas A&M University College of

Engineering Spark! PK-12 Engineering Education Outreach program. The FLIR E60 IR camera was used for a proof of concept test, presented in Section 3.2.2.2. The E60 has an IR resolution of 76,800 pixels (320 pixels x 240 pixels), sensitivity of 0.05^{o}C at 30^{o}C, and an accuracy of $\pm 2^o$C or $\pm 2\%$ of the reading, a common accuracy for an uncooled IR camera [94].

Figure 3.3: FLIR E60 IR camera

3.2.2.2 Proof of Concept: Measurement of Thermal Changes due to Posture Using IR Camera

3.2.2.2.1 Procedures An initial proof of concept test was performed with the FLIR E60 IR camera. The purpose of this test was to determine if an IR camera was sufficiently sensitive to detect variations in lower leg skin temperature due to postural changes.

A total of seven subjects, six male and one female, participated in the evaluation. Two horizontal landmark lines were drawn with a Sharpie pen to delineate a ROI on the subject's right lower leg, Figure 3.4. The distance between the landmark lines, given in Table 3.2, was consistent within 0.32 cm for five of the subject (Subjects 1-4 and 6). The distance was shorter on Subject 7 as this subject had a shorter lower leg than the other subjects. One IR image was taken of the ROI with the subject in a standing posture. The subject was then asked to lie supine for 30 minutes with IR images of the ROI taken every two minutes, Figure 3.5. For all images, the E60 was maintained at an absolute distance of one meter from the center of the landmark lines on the subject's shin,

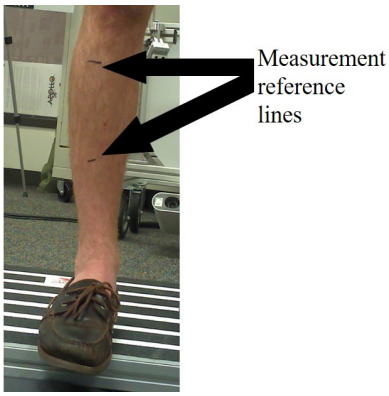

Figure 3.4: Sharpie pen landmarks to delineate ROI

Figure 3.5: Proof of Concept experimental layout for supine subject

as measured by a Komelon Gripper 8 m tape measure. Prior to data collection, the room temperature and relative humidity were measured and recorded with the Perfect Prime Data Logger. The IR camera settings are listed below, and presented in Table 3.3: A) emissivity equal to 0.98, the accepted value for clean dry human skin [36], [37], [35], [38], [39], B) reflected temperature equal to 20^{o}C as recommended by the FLIR manual when the exact value is unknown [95], C) relative humidity equal to the value measured with the data logger at the test start, D) atmospheric temperature set to the value measured with the data logger at the test start, E) distance equal to 1 m, and F) image mode set to Thermal MSX.

Table 3.2: Distance between landmark lines and area of ROI for each subject

	Distance between Landmark Lines	Area of ROI
Subject 1	15.24 cm	120.3 cm^2±4.4 cm^2
Subject 2	15.24 cm	96.8 cm^2±16.8 cm^2
Subject 3	15.56 cm	113.3 cm^2±9.8 cm^2
Subject 4	15.56 cm	117.0 cm^2±10.2 cm^2
Subject 5	N/A	N/A
Subject 6	15.56 cm	121.5 cm^2±6.0 cm^2
Subject 7	12.7 cm	93.3 cm^2±9.5 cm^2

Table 3.3: FLIR E60 camera settings used for proof of concept test

	Parameter	Camera Setting
A	Emissivity	0.98
B	Reflected Temperature	20^{o}C
C	Relative Humidity	As measured
D	Atmospheric Temperature	As measured
E	Distance	1 m
F	Image Mode	Thermal MSX

The FLIR E60 has a feature that allows the user to draw a box ROI, and the camera determines the average, maximum, and minimum temperature within the selected region. This feature was employed on each of the images taken, with the height of the ROI defined by the landmark lines and the width made as wide as possible while still containing only skin temperature. As the size of the subjects' legs varied, so did the total area of the box ROI.

3.2.2.2.2 Results The mean decrease in ROI average skin temperature after 30 min supine across the seven subjects was 0.5^{o}C, shown in Figures 3.6 and 3.7. Five subjects showed a decrease in skin temperature, as hypothesized. Two subjects showed an immediate increase in skin temperature, one of which subsequently decreased. There were several uncontrolled factors in this test. Subjects 1 through 6 were tested at a room temperature of 23.9^{o}C$\pm$0.37^{o}C and a relative humidity of 49.8%$\pm$4.9%, however Subject 7's test occurred at a room temperature of 28.4^{o}C and a relative humidity of 52.3%. The time the subject remained standing prior to data collection varied as did the time the leg was exposed to the room environment. Subjects were asked to remain still during the supine portion of the test. However, some subjects struggled to remain still, in particular Subject 4, which may have influenced the skin temperature results.

This test series did demonstrate that there is a downward trend in skin temperature with the change in posture from standing to supine, as hypothesized. The IR camera was shown to be capable of detecting changes in skin temperature. The test also aided in determining various factors to be controlled in future studies including: subject stillness, providing sufficient time for thermal homeostasis to occur prior to imaging, and standardizing the size of the ROI. For repeated tests

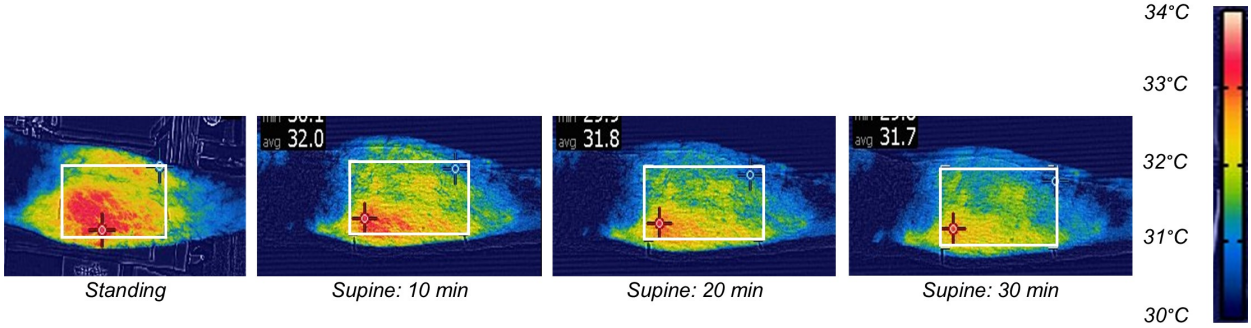

Figure 3.6: IR images of ROI of Subject 1 showing temperature drop from standing to 30 min supine

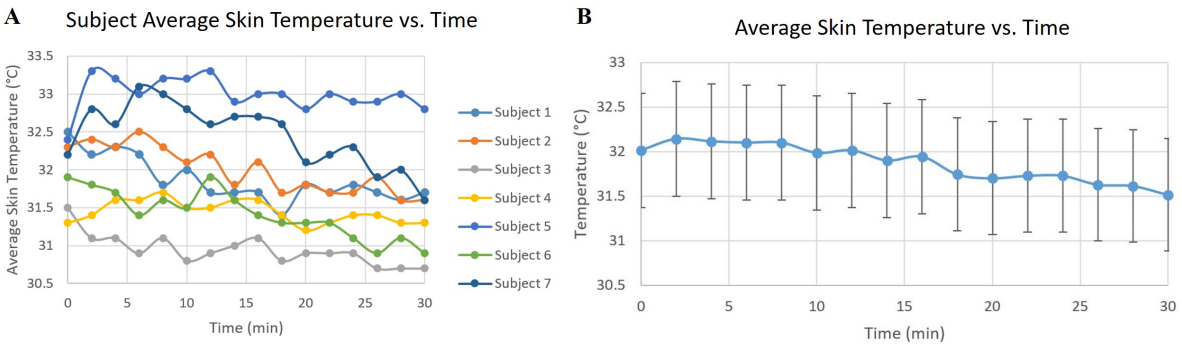

Figure 3.7: A) Average skin temperature in ROI variation as a function of time supine, and B) Average skin temperature in ROI across all seven subjects as a function of time supine. Note the downward trend in skin temperature

of the same subject, the test time will need to remain consistent to avoid circadian rhythm effects [37].

3.2.2.3 Developing Performance Requirements for the IR Camera

Following discussions with the technical staff of the camera division of Infratec Infrared, LLC. and FLIR Systems, Inc., coupled with recommendations from Dr. Kaitlyn E. Crawford (Assistant Professor, University of Central Florida) [97], as well as the results from the proof of concept test, a set of preferred performance specifications were developed for an IR camera. It was decided that the system should have a minimum resolution of 640 x 480 pixels to allow for a large data set to calculate the average temperature over the lower leg and sufficient detail to observe minor variations in skin temperature, as little as 0.5^{o}C as seen during the proof of concept. To ensure

the repeatability of the measurements, the sensitivity should be less than 0.03^{o}C and the accuracy $\pm 1^o$C or $\pm 1\%$, the highest accuracy achievable without a cooled sensor. For the camera to be versatile and ensure the repeatability and accuracy of the results, the emissivity should be user defined, not a fixed value nor estimated by software in the camera.

3.2.2.4 FLIR T650sc

Table 3.4 presents the results of the trade study. Based on the trade study, the FLIR T650sc, Figure 3.8, was purchased. The FLIR T650sc is from a series of IR cameras specifically designed for use in research labs and has been used in the medical industry to measure skin temperature. The camera has an IR resolution of 307,200 pixels (640 pixels x 480 pixels), sensitivity of less than 0.02^{o}C at 30^{o}C, and an accuracy of $\pm 1^o$C or $\pm 1\%$ of the reading [95]. The angular field of view (FOV) of the camera is 25^o x 19^o with a minimum focus distance of 25 cm, a focal length of 2.5 cm, and a pixel pitch of $17*10^{-4}$ cm. Table 3.5 provides a comparison of the E60 and T650sc specifications.

Table 3.4: IR camera trade study

Company	**Model**	**Resolution**	**Accuracy**	**Sensitivity**	**Angular Field of View**	**Emissivity Settings**
FLIR	E85	384 x 288	±2°C or ±2% for 15°C to 35°C	0.04°C at 30°C	24° x 18°	Variable from 0.01 to 1
FLIR	T640	640 x 480	±2°C or ±2% whichever is greater at	0.03°C at 30°C	15° x 11°	Variable from 0.01 to 1
FLIR	T650sc	640 x 480	±1°C or ±1% of reading	< 0.02°C	25° x 19°	Variable from 0.01 to 1
InfraTec	VarioCAM HDx	640 x 480	±2°C or ±2% of reading	< 0.03°C	n/a	Internal correction
Optris	PI 640	640 x 480	±2°C or ±2%	0.075°C	4 different options	n/a
Infrared Cameras Inc.	P series	640 x 512	±1°C or ±1%	< 0.02°C at 30°C	Based on lens	Not controllable
Fluke	TiX580	640 x 480	±2°C or ±2% whichever is greater at	< 0.05°C at 30°C	34° x 24°	Variable from 0.01 to 1

Figure 3.8: FLIR T650sc IR camera

Table 3.5: FLIR E60 and T650sc Camera Specifications [94], [95]

Parameter	**FLIR E60**	**FLIR T650sc**
IR Resolution	320x240 pixels	640x480 pixels
Sensitivity	<0.05^{o}C @ 30^{o}C	.02^o @ 30^{o}C
Accuracy	$\pm$2^{o}C or $\pm$2%	$\pm$1^{o}C or $\pm$1%
Angular Field of View	25^o x 19^o	25^o x 19^o
Min. Focus Distance	40 cm	25 cm

3.2.2.5 ResearchIR Max

A license to the FLIR ResearchIR Max software was included in the purchase of the FLIR T650sc. ResearchIR Max is used for post-processing of IR images. This includes exporting the images as a radiometric JPEG (a JPEG with embedded temperature information in each pixel) and .mat files (640 x 480 matrices of temperature values corresponding to the pixels of the image which can be used in MATLAB), and changing the color palette of the IR image.

3.2.3 3D Scanner

A 3D scanner was chosen as the method of measuring changes in leg volume. Unlike a stocking plethysmograph, no assumptions are made in the calculations such as treating the leg as a truncated cone [57]. While water displacement can provide an accurate volume measurement, this is not practical when testing at various tilt levels. 3D scanning also provides a full 3D image of the leg, which can be used to determine if there are specific locations with a larger relative fluid shift, than only total volume data provided by other methods. The final 3D image also allows for registration of IR images.

3.2.3.1 Requirements

The 3D scanner system must be capable of outputting a standard 3D image file, such as an OBJ or STL. The scanner must be under 1 kg to allow for the scanner to easily be used either manually or mounted to the tilt table or on a tripod. A high frame rate and point per second rate is essential as the scans should be performed quickly and accurately. As the images will be used to measure

changes in leg volume as little as 0.1 liters, a high resolution and accuracy, at least 0.1 mm, are required. The scanner should collect color data as well because skin color variation could indicate a change in blood circulation. The results of the trade study are presented in Table 3.6.

Table 3.6: 3D scanner trade study

Company	**Model**	**Resolution**	**Accuracy**	**Points per Second**	**Frames per Second**	**Color Scanning**
Shining 3D	EinScan Pro+	n/a	0.1 mm	550,000	n/a	n/a
Shining 3D	EinScan Pro+ 2X+	n/a	0.05 mm	110,000	20	n/a
3D	Sense 3D	1 mm	1 mm	n/a	30	2 Mpx
ScanTech	iReal 3D	n/a	0.1 mm	550,000	15	Yes
Artec 3D	Eva	0.5 mm	0.1 mm	2,000,000	16	1.3 Mpx
Artec 3D	Space Spider	0.1 mm	0.05 mm	1,000,000	7.5	1.3 Mpx

3.2.3.2 Artec 3D Space Spider

Of the scanners reviewed, the Artec 3D Space Spider, Figure 3.9, met all the requirements and was recommended by the Human Research Program group at NASA JSC. The Space Spider is used in the medical industry to assist in designing custom prosthetics [98]. It has a FOV of 30^o x 21^o and a working distance from 20 cm to 30 cm [99]. The scans can be saved as seven different 3D mesh formats, including OBJ and STL, as well as two 3D point cloud formats.

Figure 3.9: Artec 3D Space Spider 3D scanner

3.2.3.2.1 Artec Studio A license to the Artec Studio software was included with the purchase of the Artec 3D Space Spider. This software works with the Artec 3D Space Spider to perform scans and integrate a series of scans into a final 3D image. The final 3D image is a very fine, closed mesh structure and texture map, as shown in Figure 3.10. Several tools are included in the software such as editing the model (translate, rotate, scale, erase points, relocate origin, etc.), fixing holes in the model, and exporting the model as various file types including STL and OBJ.

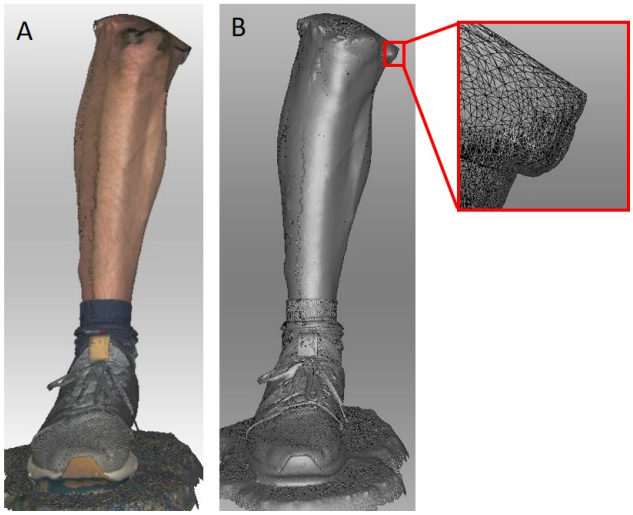

Figure 3.10: A) 3D image of subject leg with texture mapping produced in Artec Studio, B) Mesh structure of 3D image shown in A

3.2.4 Tilt Table

A tilt table was chosen as the method of simulating micro- and partial gravity levels. This was chosen as tilt, as previously stated, is a good analog, allowing for steady-state simulated gravity levels to be tested with minimal hardware requirements [69], [64], [52].

3.2.4.1 Requirements

As the subject studies will require a 1g (Earth, 9.81 m/s^2) baseline, the tilt table must be capable of a vertical, standing position. This requirement eliminated the Exerpeutic tilt tables which allowed for a max angle of 165^o. The study also requires the table to be held at fixed angles from 0^o to 90^o, therefore the table must be able to assume any angle within that range. If necessary, a method for fixing the angle can be designed. A full trade study of tilt tables was conducted. A condensed study is presented in Table 3.7

Table 3.7: Tilt table trade study

Company Name	**Product Name**	**Length Range**	**Achieve Vertical?**	**Angle Lock**	**Max Weight**
Teeter	FitSpine X3	56" to 78"	Yes	Tether with markings for 20^o, 40^o, and 60^o	300 lbs
Exerpeutic	225SL inversion table	57" to 78"	No	3 angle adjustable cross bar	250lbs
Exerpeutic	575SL Foldaway Mobile Inversion Table	n/a	No	4 angle control pin	300 lbs
Innova	ITX9800	58" to 78"	Yes	6 angle control pin	300 lbs
Harrison	HR-407	58" to 77"	Yes	n/a	350 lbs

3.2.4.2 Teeter FitSpine X3

Based on the aforementioned requirements, the Teeter FitSpine X3 was chosen, Figure 3.11. This tilt table has the widest height range supported, therefore encompassing the largest portion of the percentile range for future EVA suits. The table can achieve a vertical posture, and any angle between the 0^o and 90^o, Figures 3.12 and 3.13. It comes with a tether with markings for 20^o, 40^o and 60^o, which can be removed.

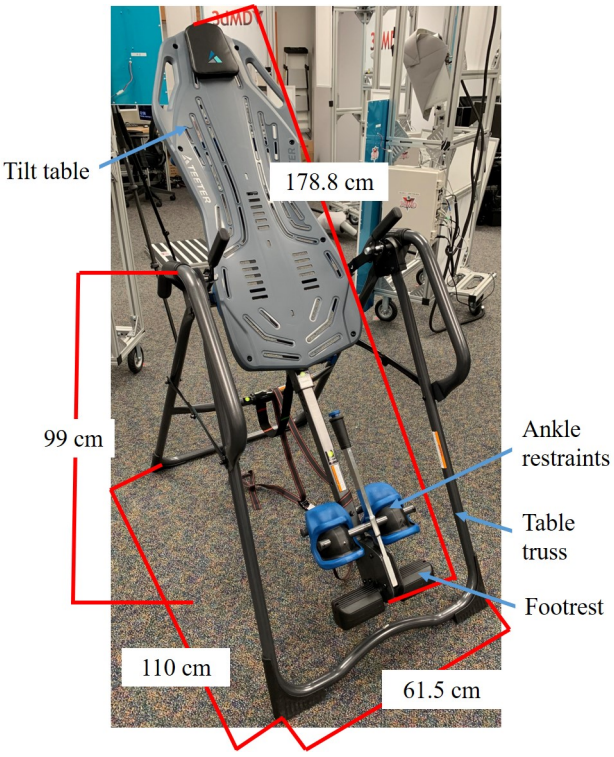

Figure 3.11: Teeter FitSpine X3 tilt table

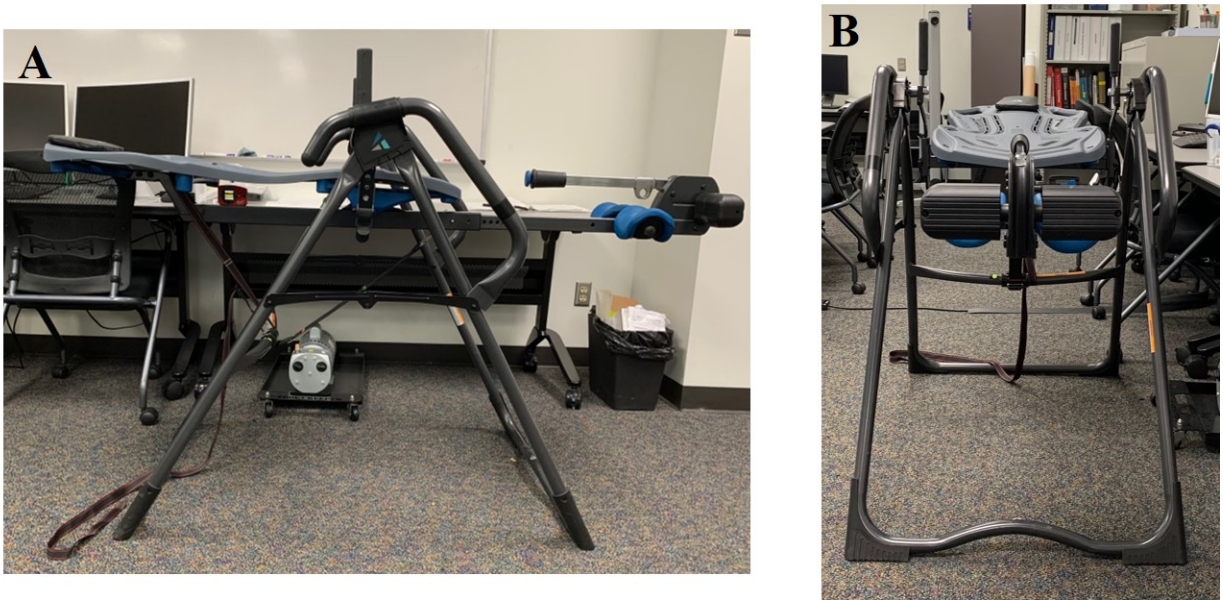

Figure 3.12: Teeter FitSpine X3 tilt table at an angle of 0^o, horizontal, A) side view, and B) front view

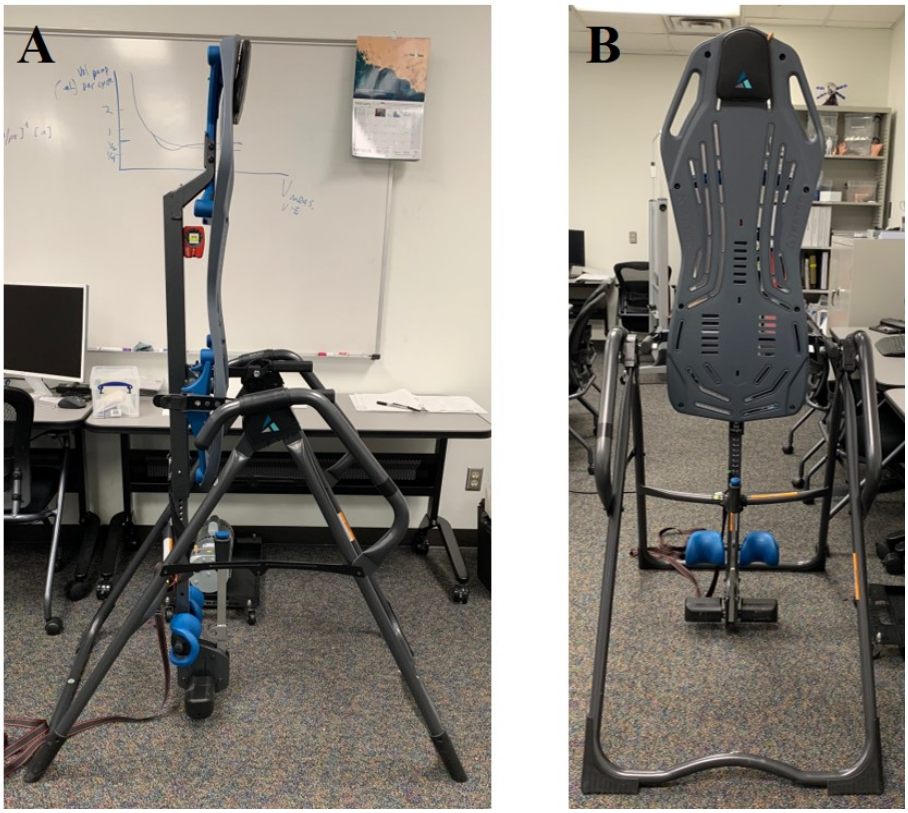

Figure 3.13: Teeter FitSpine X3 tilt table at an angle of 90^o, vertical, A) side view, and B) front view

3.2.4.2.1 Instrument Mount A method of mounting the IR camera and 3D scanner that allowed the instruments to move with the tilt table, therefore ensuring a consistent imaging location, was required. The chosen system must be simple to use and require minimal manual adjustments, capable of supporting the weight of both instruments, and ensure the front of the subject's right lower leg is within their FOV, listed in Table 3.8. To assist with the design of the mounting system, a computer aided design (CAD) model of the tilt table and truss were created in SOLIDWORKS. Several different methods were considered including a tripod, an external structure (Figure 3.14A), commercial camera arms attached to the handrails (Figure 3.14B), and designing a structure that mounts directly to the table.

Table 3.8: Weights and working distances of the IR camera and 3D scanner

Instrument	**Weight (lbs)**	**Weight (kg)**	**Working Distance**
FLIR T650sc	2.87	1.3	$\geq$ 25 cm
Artec 3D Space Spider	1.9	0.85	20 cm to 30 cm

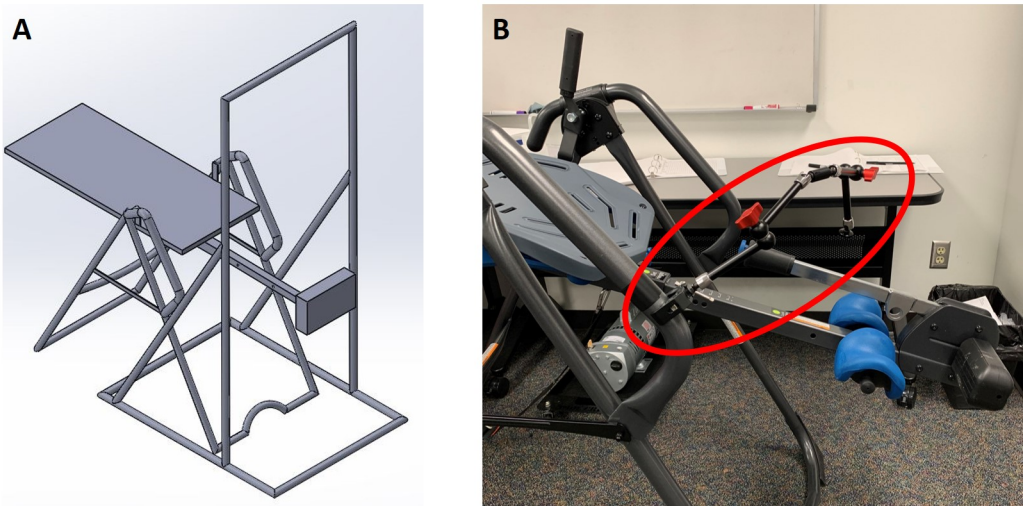

Figure 3.14: Considered instrument mount designs: A) External structure, and B) Camera arms

3.2.4.2.2 Fix Tilt Angle As the Teeter FitSpine X3 does not have a method to fix the table angle beyond the tether, a more substantial method must be developed that can fix the angle of the tilt table from 0^o to 90^o in 10^o increments and the analog angles for Lunar (9.5^o) and Martian (22.4^o) gravity. The method must be simple to implement and cannot contain components that could stretch with loading and use, such as straps. The end points of the system should be fixed relative to the structure, to minimize the workload of the operator. If an end point was allowed to move relative to the structure, the exact location of the end point could vary between test, adding uncertainity to the tilt angle.

3.3 Experimental Design

3.3.1 IR Camera FOV

While the angular FOV of an IR camera is fixed, the size of the FOV varies with distance by Equations 3.1 and 3.2, shown in Figure 3.15. The number of image pixels to a 1 cm span of the imaged object is inversely proportional to the image distance, Equations 3.3 and 3.4 and Figure 3.16.

$$Horizontal\ FOV = 2 * depth * tan(\frac{25^o}{2}) \tag{3.1}$$

$$Vertical\ FOV = 2 * depth * tan(\frac{19^o}{2}) \tag{3.2}$$

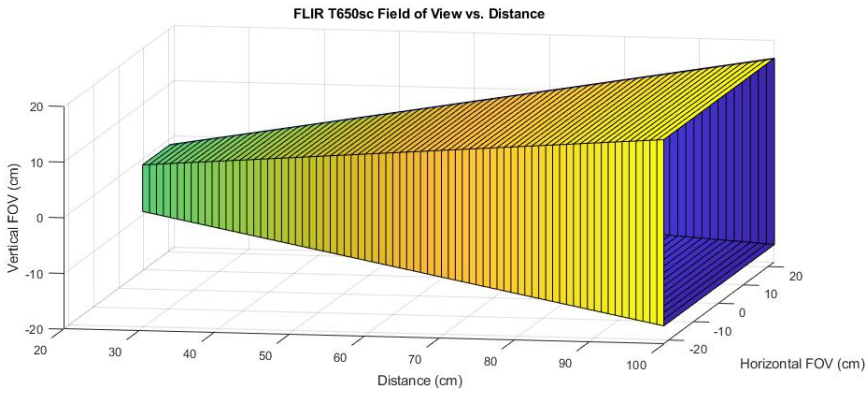

Figure 3.15: Field of view of the FLIR T650sc from 25cm to 100cm

$$Horizontal\ number\ of\ pixels/cm = \frac{horizontal\ resolution * grid\ size}{horizontal\ FOV(cm)}) \tag{3.3}$$

$$Vertical\ number\ of\ pixels/cm = \frac{vertical\ resolution * grid\ size}{vertical\ FOV(cm)}) \tag{3.4}$$

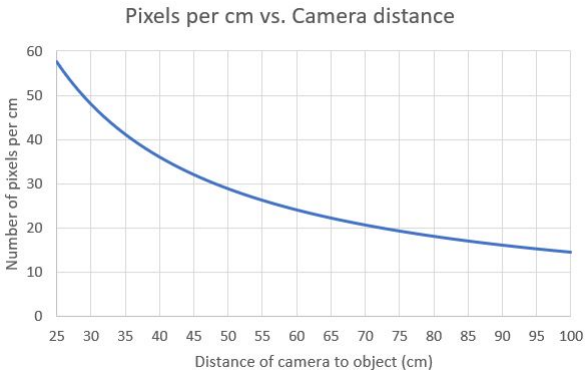

Figure 3.16: Graph of the relationship between the image distance and size of a pixel

For the final subject study, the IR camera should be placed sufficiently far from the lower leg to minimize the number of images to be taken, while ensuring sufficient resolution. As blood is the main mechanism of heat transfer within the body [31], [30], and a decrease in blood flow to the legs has been shown in microgravity [60] and simulated microgravity [61], areas around superficial vessels, such as the great and small saphenous veins, are of particular interest. These regions

might provide a larger role in heat transfer than other regions of the leg. Therefore, the resolution of the images must be sufficient to distinguish superficial vessels. To assist with determining the minimum resolution requirements, and therefore maximum distance, a series of grids of varying sizes was chosen. The grid allows determination of what distance is required to see a change in the average skin temperature that would indicate the presence of a vessel within a square known to contain a superficial vessel.

The Johnson's Criteria, a standard in IR thermography, can be used to determine the max imaging distance for an object to be recognized and identified in an IR image via Equation 3.5 [100], [101], [102]. For recognition, the Johnson Criteria states that an object must be spanned by 6 pixels and for identification of the object, it must be spanned by 12 pixels [100], [101], [102].

$$distance = \frac{object\ size}{number\ of\ pixels} * \frac{focal\ length}{pixel\ pitch} \tag{3.5}$$

3.3.1.1 ResearchIR ROI Grid

The first method used to create the grid used ResearchIR Max. Within the software, there is a ROI tool that will provide the average, minimum, and maximum temperatures, standard deviation, and number of pixels within the specified ROI. Using this tool, a series of square ROI were drawn with a side length of 57 pixels, or 1 cm for an image taken 25 cm away, to form a 1 cm grid pattern. The temperature data can then be manually transferred into a spreadsheet for future use.

The initial 1 cm grid, as shown in Figure 3.17A with the varying thickness and misalignment of the grid lines, was not very consistent with an average pixel count per box of 3,210.9$\pm$59.2 pixels. Once more experience with the software was acquired, a second 1 cm grid was created, with each box containing 3,249$\pm$0 pixels, that of a 57 pixel by 57 pixel square, Figure 3.17B. The squares in the new pattern are more accurately placed to form a perfect grid. To test the sensitivity of the grid pattern, a second grid was created with 0.5 cm boxes for an image taken at 25 cm, Figure 3.18

There are several disadvantages to this method of obtaining the temperature data from a grid pattern. Creating the grid pattern takes several hours and each grid pattern is only valid for a

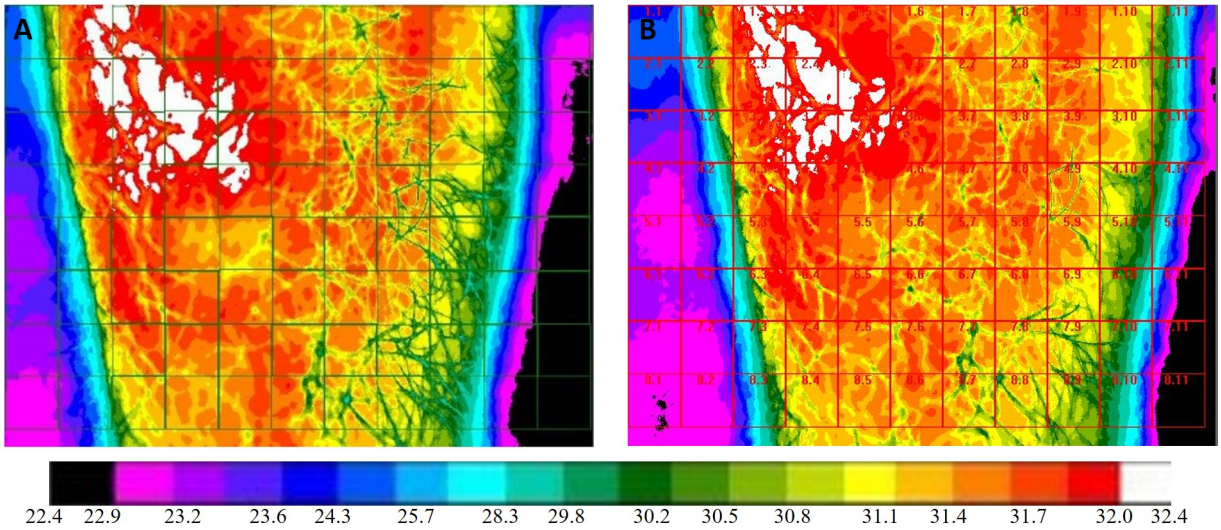

Figure 3.17: 1 cm grid pattern for image taken at 25 cm created with the ROI tool within ResearchIR Max on an IR image of a subject's lower leg taken at 25 cm, A) first attempt, note the uneven grid pattern by the varying lines thickness and uneven lines and B) second grid created, note the much more consistent grid pattern. All temperatures given in degrees Celsius

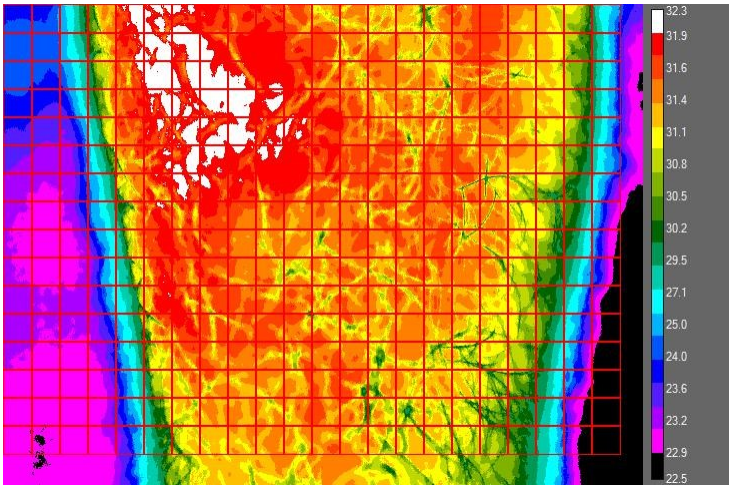

Figure 3.18: 0.5 cm grid pattern for image taken at 25 cm created with the ROI tool within ResearchIR Max on an IR image of a subject's lower leg taken at 25 cm. All temperatures given in degrees Celsius

specific image distance. If a different grid size or image distance is required, a new grid must be created. Once the grid has been created, it can be saved and applied on images in the future. However, the 0.5 cm grid pattern had to be saved as two separate ROI patterns, as the software would not load the file if it contained more than 11 rows of the 0.5 cm grid. Transferring the

data from the ResearchIR Max software to a spreadsheet is very time consuming as well, as the information must be inputted manually.

3.3.1.2 MATLAB Grid Code

Based on the disadvantages previously mentioned for the grid ROI in ResearchIR Max, a MATLAB code was developed to provide a more versatile method to acquire the same information. The code uses the temperature information from a .mat file, a 480 x 640 matrix, exported from ResearchIR Max. The code allows the user to specify the desired grid size and the image distance. The code then determines the maximum, minimum, and average temperature within each grid square. The information is stored in a text file which can be saved and imported into a spreadsheet within a few minutes.

Within the code are the relevant IR camera parameters: resolution (640 pixels x 480 pixels) and FOV (25^o x 19^o). These parameters can be quickly altered, as needed, by changing two lines of code. This, combined with the user inputs of grid size and image distance, allows the code to be very versatile, working with any IR camera, IR image, image distance, and desired grid size.

The original IR image is displayed with the overlaid grid, followed by a series of three separate images with the color within each grid square reflecting the spatial average, minimum, and maximum temperature of the square. An example of all four images created by the code are shown in Figure 3.19. The three modified images were added to the code to assist with visualizing the temperature information provided.

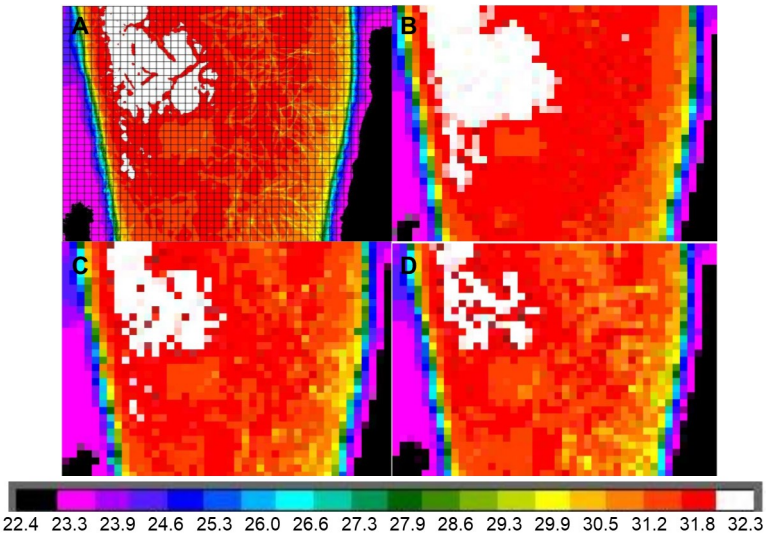

Figure 3.19: Sample image at 25 cm with a 0.25 cm grid from MATLAB with A) grid displayed over sample image, B) grid square color corresponding to maximum temperature in square, C) grid square corresponding to the spatial average temperature in square, D) grid square color corresponding to minimum temperature in square. All temperatures given in degrees Celsius

3.3.2 IR to 3D Image Registration

A MATLAB code was developed to register a series of IR images from the FLIR T650sc to a 3D image from the Artec 3D Space Spider. The code was developed using the principles established by Dr. Adam Chromy of Brno University, Czech Republic [92], [103]. This method for IR to 3D image registration was chosen as it is a versatile system, working with any 3D image and IR camera, and it does not rely on the user to select corresponding points. For each IR image, the following parameters are needed: location of the camera in space relative to the origin of the 3D image ($\vec{p}_{from}$), direction of the camera view ($\vec{d}_{to}$), direction defining 'up' in the camera image ($\vec{d}_{up}$), the camera angle FOV (δ_H and δ_V), camera focal distance (f_c), and camera resolution (w_1 and h_1).

Based on these parameters, the location of the image plane and image frame corners (P_{BL}, P_{BR}, P_{TL}, P_{TR}) relative to the camera location are determined, as shown in Figure 3.20 and Equations 3.6 to 3.9 [103].

$$P_{BL} = f_c * \vec{d}_{to} - \vec{d}_{CU} + \vec{d}_{CL} + \vec{d}_{shift} \tag{3.6}$$

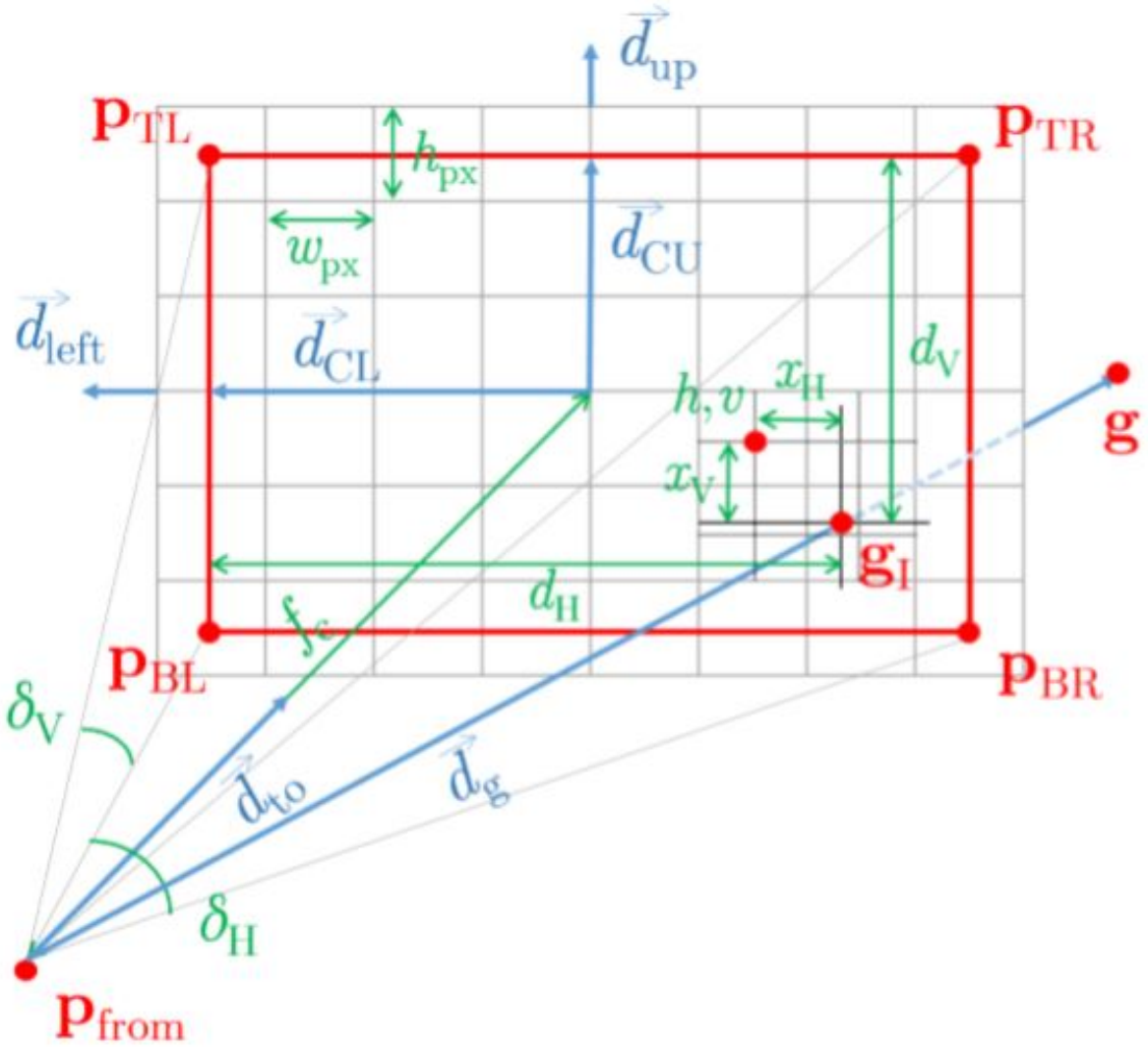

Figure 3.20: Illustrations of main vectors and variables used in IR 3D image registration. Reprinted from [103]

$$P_{BR} = f_c * \vec{d}_{to} - \vec{d}_{CU} - \vec{d}_{CL} + \vec{d}_{shift} \tag{3.7}$$

$$P_{TL} = f_c * \vec{d}_{to} + \vec{d}_{CU} + \vec{d}_{CL} + \vec{d}_{shift} \tag{3.8}$$

$$P_{TR} = f_c * \vec{d}_{to} + \vec{d}_{CU} - \vec{d}_{CL} + \vec{d}_{shift} \tag{3.9}$$

The vectors $\vec{d}_{CL}$ and $\vec{d}_{CU}$, Equations 3.10 and 3.11, represent the vectors from the center of the

image frame to the left edge and top edge of the image frame, respectively [103].

$$\vec{d}_{CL} = \vec{d}_{left} * tan(\frac{\delta_V}{2}) * norm(f_c * \vec{d}_{to}) * (1 - \frac{1}{w_1}) \tag{3.10}$$

$$\vec{d}_{CU} = \vec{d}_{up} * tan(\frac{\delta_H}{2}) * norm(f_c * \vec{d}_{to}) * (1 - \frac{1}{h_1}) \tag{3.11}$$

$$\vec{d}_{left} = (\vec{d}_{up} \times \vec{d}_{to}) \div norm((\vec{d}_{up} \times \vec{d}_{to})) \tag{3.12}$$

The vector between each point (g) of the 3D image and the camera is calculated, ($\vec{d}_g$). If the vector intersects the image plane, the intersection point is determined (g_1), if not the point is rejected. The location of g_1 is tested to determine if it is within the image frame. The point is rejected as not being in frame if it fails one of the following tests [103]:

$$\frac{P_{BR} - P_{BL}}{norm(P_{BR} - P_{BL})} \times \frac{g_1 - \vec{p}_{from} - P_{BL}}{norm(g_1 - \vec{p}_{from} - P_{BL})} < 0 \tag{3.13}$$

$$\frac{P_{TR} - P_{BR}}{norm(P_{TR} - P_{BR})} \times \frac{g_1 - \vec{p}_{from} - P_{BR}}{norm(g_1 - \vec{p}_{from} - P_{BR})} < 0 \tag{3.14}$$

$$\frac{P_{TL} - P_{TR}}{norm(P_{TL} - P_{TR})} \times \frac{g_1 - \vec{p}_{from} - P_{TR}}{norm(g_1 - \vec{p}_{from} - P_{TR})} < 0 \tag{3.15}$$

$$\frac{P_{BL} - P_{TL}}{norm(P_{BL} - P_{TL})} \times \frac{g_1 - \vec{p}_{from} - P_{TL}}{norm(g_1 - \vec{p}_{from} - P_{TL})} < 0 \tag{3.16}$$

If the point is within the camera FOV, it must then be determined if the point is hidden behind other points of the 3D model. This is determined by testing if $\vec{d}_g$ intersects a face of the 3D image. To reduce the computational time required to iterate through the faces of the 3D image, a modified Octree data structure was used. An example of the Octree data structure is shown in Figure 3.21. The first level of the structure is a single cube that encompasses the entire 3D image. This cube is divided into eight 'children', or smaller cubes one eighth of the size of the original cube. The number of levels within the structure is dependent on the minimum cube size. The final layer, instead of children, lists the faces contained within the cube. If a cube does not contain any faces of the 3D image, the cube is removed from the structure.

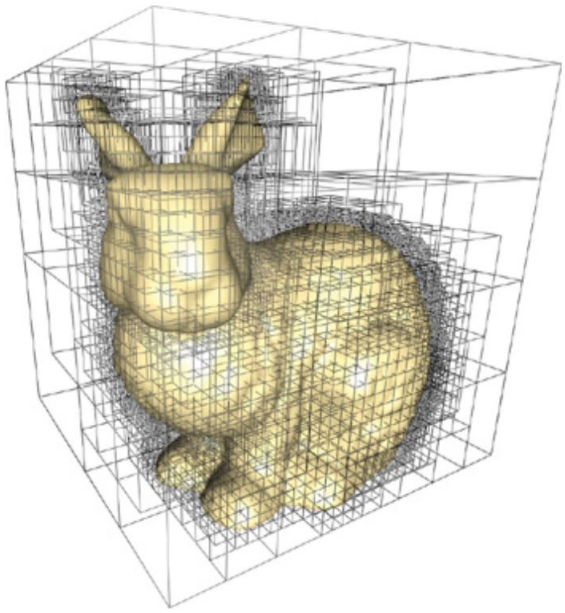

Figure 3.21: Example of the Octree cube structure. Reprinted from [104]

The program iterates through cubes from the highest layer to the lowest, determining the cubes $\vec{d_g}$ intersects. If the vector intersects a cube, it's children are tested for an intersection. If more than one cube is intersected by the vector at the lowest level, the cubes are tested to determine if a cube contains the point g. If so the cube is removed from the list, and its children are not tested for further intersections. Once all cubes are tested at one level, the code proceeds to test the children of the intersected cubes. Only the faces contained in the intersected cubes at the lowest level are tested for intersection points. If an intersection is detected, the point is rejected and the code continues onto the next point in the 3D image.

If no intersection is detected, the point on the 3D image is within the image frame and visible to the camera. The nearest pixel to the intersection point in the image frame is determined, and an interpolation of surrounding pixel temperatures is used to determine the temperature of the point on the 3D image (t_g), using Equations 3.17 and 3.18.

$$t_g = f_{interp}(f_{interp}(t_{h,v}, t_{h,v+1}, x_H), f_{interp}(t_{h+1,v}, t_{h+1,v+1}, x_H), x_V) \tag{3.17}$$

$$f_{interp}(t_1, t_2, d) = (1 - d) * t_1 + d * t_2 \tag{3.18}$$

Once the code has processed all the images, the average of the calculated temperature values for each point is determined. The RGB triplet is assigned to each point corresponding to the nearest known temperature-color combination. The points are then displayed as a 3D point cloud.

4.1 FLIR T650sc IR Camera FOV

The distance between the IR camera and the imaged object has an effect on the resolution of the resultant images, as shown in Figure 4.1. The FOV increases as the distance is increased per Equations 4.1 and 4.2, as was shown in Figure 3.15. For an image taken at 25 cm with the FLIR T650sc, the camera FOV is 11.1 cm by 8.4 cm, which is increased to 41.7 cm by 31.5 cm if the camera is moved to 1 m from the imaged object. The number of image pixels in a centimeter of the object decreased from 57 pixels/cm to 15 pixels/cm for the same distance increase, per Equations 4.3 and 4.4, a decrease of 93% in the number of image pixels per squared centimeters, as was shown in Figure 3.16.

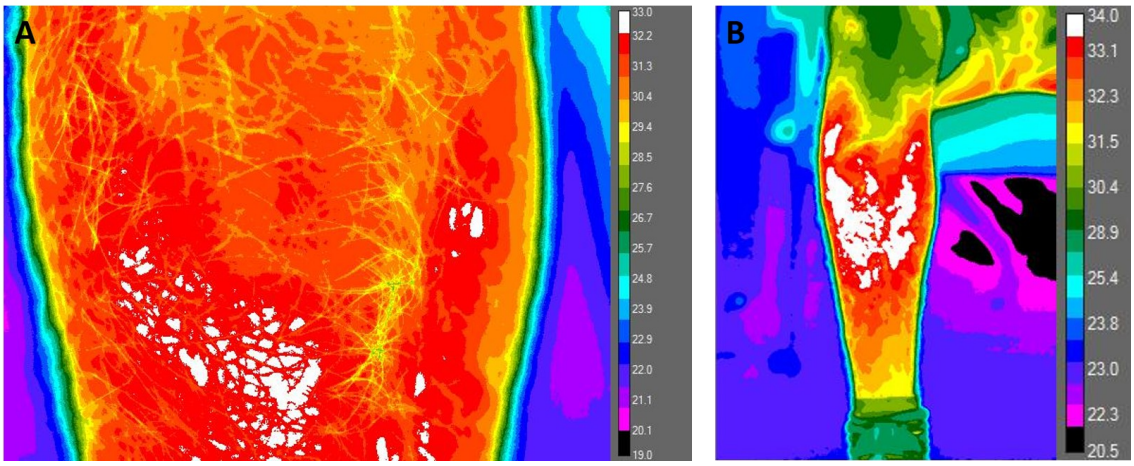

Figure 4.1: IR images of subject's right lower leg A) at 25 cm and B) at 94 cm. Temperature scales in degrees Celsius

$$Horizontal\ FOV = 2 * depth * tan(\frac{25^o}{2}) \tag{4.1}$$

$$Vertical\ FOV = 2 * depth * tan(\frac{19^o}{2}) \tag{4.2}$$

$$Horizontal\ number\ of\ pixels/cm = \frac{horizontal\ resolution * grid\ size}{horizontal\ FOV(cm)} \tag{4.3}$$

$$Vertical\ number\ of\ pixels/cm = \frac{vertical\ resolution * grid\ size}{vertical\ FOV(cm)} \tag{4.4}$$

As blood is a main conductor of heat within the human body [31], [30] and studies have shown simulated microgravity causes a decrease in blood flow [60], [61], regions of superficial vessels may display different temperature characteristics than other regions of the leg. Therefore, the pixel size should be determined by ensuring superficial vessel, such as the great and small saphenous veins, are detectable. The size should be sufficiently small to allow detection of the vessel, while minimizing the number of images required to capture the entire leg.

4.1.1 IR Grid

4.1.1.1 Comparison of ResearchIR ROI Grid to MATLAB Grid Code

Three IR images (FLIR T650sc) were run through both the corrected ResearchIR 1 cm grid and the MATLAB code, and the average temperatures within each grid square recorded, Figure 4.2, and the difference between the two methods was determined, Table 4.1.

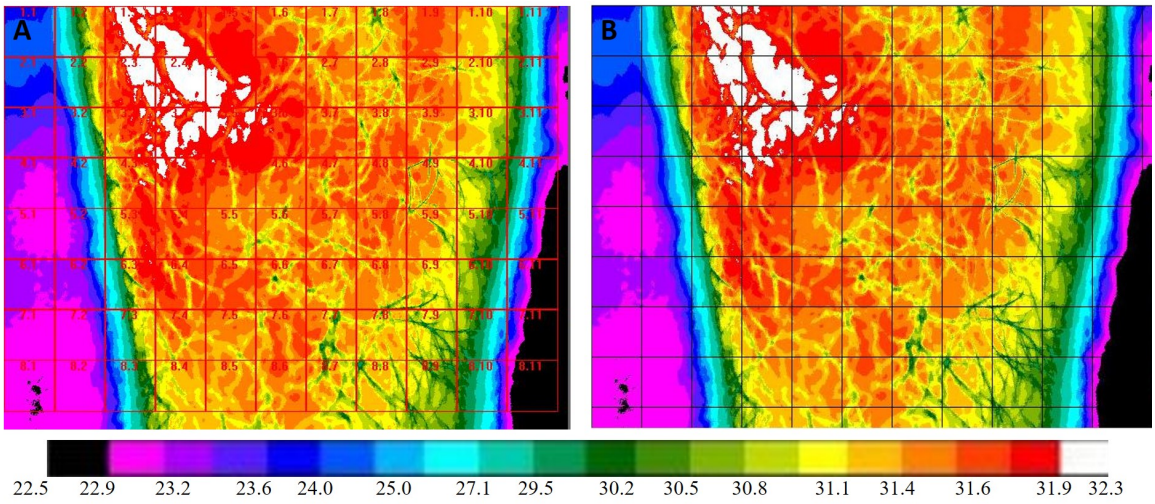

Figure 4.2: IR image with overlaid 1 cm grid for an image distance of 25 cm from A) ResearchIR Max and B) MATLAB. All temperatures given in degrees Celsius

Table 4.1: Sample average 1 cm grid square temperature data from ResearchIR, MATLAB, and the difference between the two methods for the images shown in Figure 4.2

	1.1	**1.2**	**1.3**	**1.4**	**1.5**	**1.6**	**1.7**	**1.8**	**1.9**	**1.10**	**1.11**
ResearchIR (°C)	24.0	28.9	31.9	31.8	31.7	31.4	31.3	31.2	31.5	31.1	27.1
MATLAB (°C)	24.0	28.9	31.9	31.8	31.7	31.4	31.3	31.2	31.5	31.1	27.1
Difference (°C)	0	0	0	0	0	0	0	0	0	0	0
	2.1	**2.2**	**2.3**	**2.4**	**2.5**	**2.6**	**2.7**	**2.8**	**2.9**	**2.10**	**2.11**
ResearchIR (°C)	23.8	27.9	31.8	31.9	31.9	31.6	31.3	31.2	31.4	31.1	27.0
MATLAB (°C)	23.8	27.9	31.8	31.9	31.9	31.6	31.3	31.2	31.4	31.1	27.0
Difference (°C)	0	0	0	0	0	0	0	0	0	0	0
	3.1	**3.2**	**3.3**	**3.4**	**3.5**	**3.6**	**3.7**	**3.8**	**3.9**	**3.10**	**3.11**
ResearchIR (°C)	23.3	26.1	31.6	31.9	31.8	31.7	31.5	31.4	31.3	31	26.6
MATLAB (°C)	23.3	26.1	31.6	31.9	31.8	31.7	31.5	31.4	31.3	31	26.6
Difference (°C)	0	0	0	0	0	0	0	0	0	0	0
	4.1	**4.2**	**4.3**	**4.4**	**4.5**	**4.6**	**4.7**	**4.8**	**4.9**	**4.10**	**4.11**
ResearchIR (°C)	23.0	24.7	31.2	31.7	31.6	31.5	31.4	31.4	31.2	30.6	25.4
MATLAB (°C)	23.0	24.7	31.2	31.7	31.6	31.5	31.4	31.4	31.2	30.6	25.4
Difference (°C)	0	0	0	0	0	0	0	0	0	0	0
	5.1	**5.2**	**5.3**	**5.4**	**5.5**	**5.6**	**5.7**	**5.8**	**5.9**	**5.10**	**5.11**
ResearchIR (°C)	23.0	23.7	30.7	31.6	31.3	31.2	31.3	31.4	31.2	30.3	24.2
MATLAB (°C)	23.0	23.7	30.7	31.6	31.3	31.2	31.3	31.4	31.2	30.3	24.2
Difference (°C)	0	0	0	0	0	0	0	0	0	0	0
	6.1	**6.2**	**6.3**	**6.4**	**6.5**	**6.6**	**6.7**	**6.8**	**6.9**	**6.10**	**6.11**
ResearchIR (°C)	23.0	23.3	29.5	31.5	31.5	31.3	31.3	31.3	31	29.5	23.2
MATLAB (°C)	23.0	23.3	29.5	31.5	31.5	31.3	31.3	31.3	31	29.5	23.2
Difference (°C)	0	0	0	0	0	0	0	0	0	0	0
	7.1	**7.2**	**7.3**	**7.4**	**7.5**	**7.6**	**7.7**	**7.8**	**7.9**	**7.10**	**7.11**
ResearchIR (°C)	22.9	23.0	28.2	31.3	31.3	31.4	31.1	31.1	30.8	28.2	22.8
MATLAB (°C)	22.9	23.0	28.2	31.3	31.3	31.4	31.1	31.1	30.8	28.2	22.8
Difference (°C)	0	0	0	0	0	0	0	0	0	0	0
	8.1	**8.2**	**8.3**	**8.4**	**8.5**	**8.6**	**8.7**	**8.8**	**8.9**	**8.10**	**8.11**
ResearchIR (°C)	22.8	22.9	26.9	31.1	31.3	31.3	31.1	30.9	30.6	27.2	22.6
MATLAB (°C)	22.8	22.9	26.9	31.1	31.3	31.3	31.1	30.9	30.6	27.2	22.6
Difference (°C)	0	0	0	0	0	0	0	0	0	0	0

The largest difference for the 1 cm grid between the average temperature from the two methods was 0.1^{o}C, likely due to rounding. A total of six of the 264 grid square compared had a nonzero difference. The .mat file includes temperatures listed to the thousandths of a degree Celsius, therefore the MATLAB code provides averages to the thousandths, which are then rounded to the nearest tenth of a degree. However ResearchIR presents averages to the tenth of a degree Celsius, therefore it is possible, that ResearchIR rounds the temperature values at a different step in the calculations.

A 0.5 cm grid was created in ResearchIR, though as the full grid ROI file would not open, the pattern was saved as two separate ROIs, a top (rows 1 to 11) and a bottom (rows 12 to 16). The average temperature per 0.5 cm grid square was compared to the results obtained with MATLAB for one IR image. All 352 grid squares had the same average between the two methods.

As only 2% of the 1 cm grid squares had a difference between the methods and then by only

$\pm 0.1^{o}$C, and none with the 0.5 cm grid, it is recommended to utilize the MATLAB grid program. The program is a more versatile system, capable of providing comparable average temperature results to the ResearchIR grid. It also provides additional information, through the visual representation of the average, minimum, and maximum temperature in each grid square, as was shown in Figure 3.19. Finally, the MATLAB code does not require using multiple different ROI files for a grid size of 0.5 cm or smaller to obtain information for the entire image.

4.1.1.2 Maximum Distance to Distinguish Superficial Vessel

A series of IR images (FLIR T650sc) of superficial vessels on two different subjects were run through the MATLAB grid code with varying grid sizes from 0.05 cm to 1 cm. Some example images are shown below in Figures 4.3 and 4.4.

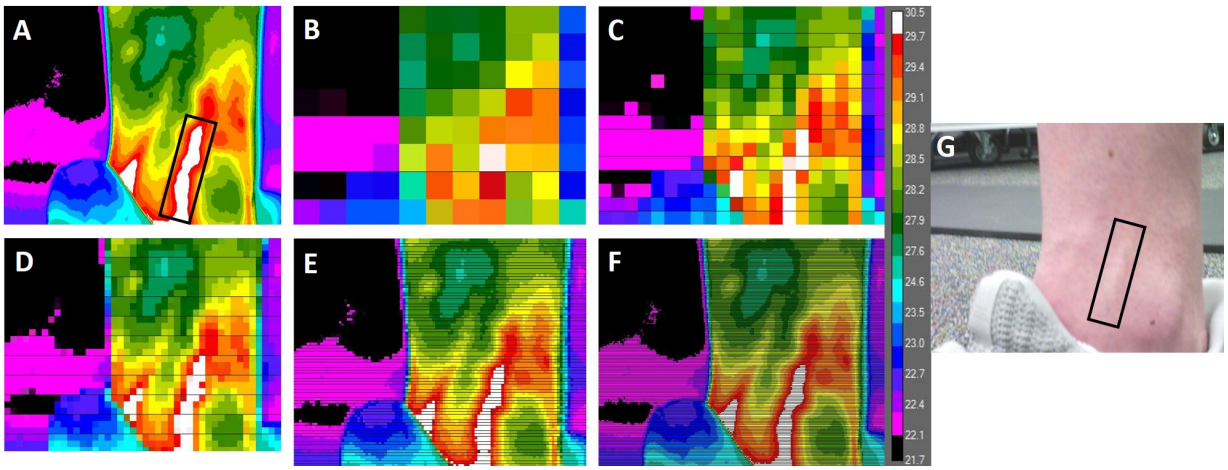

Figure 4.3: IR image of subject's inner ankle with the great saphenous vein (in black box) taken at 25 cm, A) original image, and with average grid squares of a B) 1 cm grid, C) 0.5 cm grid, D) 0.25 cm grid, E) 0.1 cm grid, F) 0.05 cm grid, and G) digital image of same region. All temperatures given in degrees Celsius

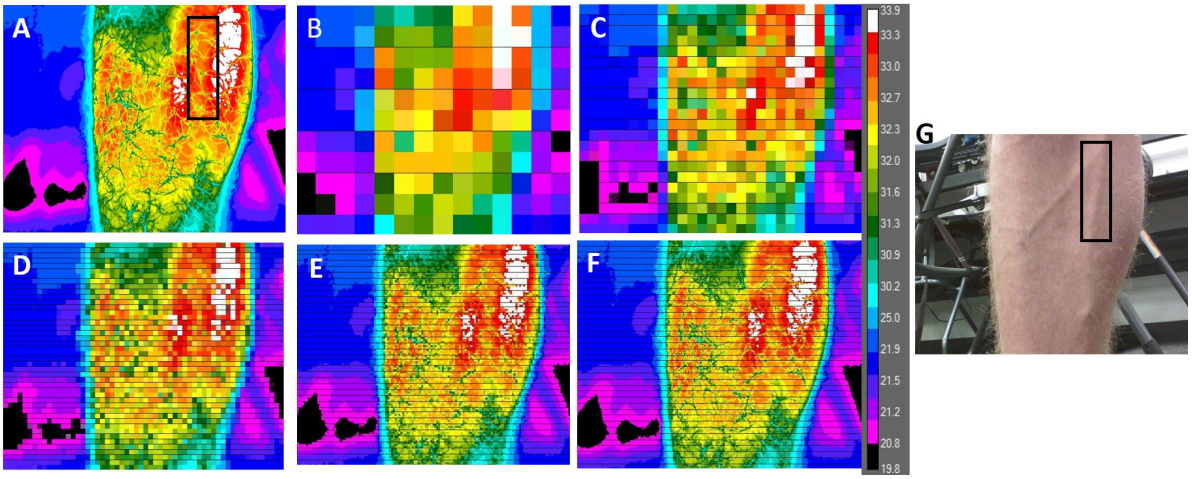

Figure 4.4: IR image of subject's leg with superficial vessels (in black box) taken at 33 cm, A) original image, and with average grid squares of a B) 1 cm grid, C) 0.5 cm grid, D) 0.25 cm grid, E) 0.1 cm grid, F) 0.05 cm grid and G) digital image of same region. All temperatures given in degrees Celsius

Figure 4.3A shows the localized heat distribution near the superficial great saphenous vein on the subject's inner ankle. The localized heat distribution begins to become visible with a grid square size of 0.25 cm and distinct for a grid size of 0.1 cm. Similarly, Figure 4.4E shows the distinct temperature distribution of the leg for a grid size of 0.1 cm.

The Johnson's Criteria, a standard in IR thermography, can be used to determine the max imaging distance for an object to be recognized and identified in an IR image via Equation 4.5 [100], [101], [102]. For recognition, the Johnson Criteria states that an object must be spanned by 6 pixels and for identification of the object, it must be spanned by 12 pixels [100], [101], [102].

$$distance = \frac{object\ size}{number\ of\ pixels} * \frac{focal\ length}{pixel\ pitch} \tag{4.5}$$

The great saphenous vein for the subject, visible in Figure 4.3, has a diameter of 0.952 cm $\pm$ 0.10 cm. Therefore, with the FLIR T650sc, for recognition of the vein, each pixel should image 0.16 cm, corresponding to an image distance of 233 cm. For identification, each pixel should image 0.08 cm, or a distance of 116 cm.

For the superficial vessel in Figure 4.4, with a diameter of 0.804 cm $\pm$ 0.074 cm, a max image distance of 197 cm, or a pixel imaging 0.13 cm is required. For identification a pixel should image

0.07 cm, or a maximum image distance of 98 cm.

4.2 Proof of Concept: Accuracy of 3D Image

A series of reference points were drawn on the right lower leg of a subject using a Sharpie pen. The markings were made to create upper and lower circumferential bands, and to ensure four dots were visible on the leg when viewed from any angle. A series of 3D scans were performed with the Artec 3D Space Spider of the leg, and, using the Artec Studio software, a 3D image of the leg was created. A series of five measurements, Figure 4.5, were made in Artec Studio and by hand, using the Lufkin Anthropometirc tape measure, with the reference points ensuring consistent start and end points for the measurements. The results are presented in Table 4.2.

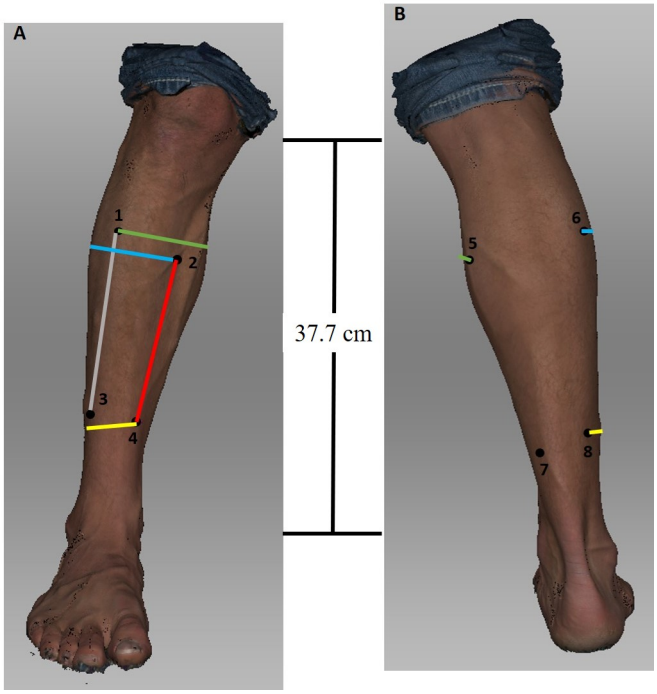

Figure 4.5: 3D image of subject's lower right leg with the eight reference dots and measurements lines A) front of the leg, and B) back of the leg

Table 4.2: Comparison of the 3D image and the real measurement values

Measurement	Line Color	3D Image (cm)	By Hand (cm)	Absolute Difference (cm)
1 to 3	grey	17.510	17.5	0.01
1 to 5	green	15.773	15.75	0.023
2 to 6	blue	18.024	18.0	0.024
4 to 8	yellow	11.554	11.6	0.046
4 to 2	red	15.769	15.8	0.031

Though there is not enough data to perform a statistical analysis of the results, there is an obvious close correlation between the the hand measurements and the 3D image measurements.

4.3 IR to 3D Image Registration

The initial IR to 3D registration ran into difficulty with the temperature of the background surroundings being registered to the 3D image, Figure 4.6.

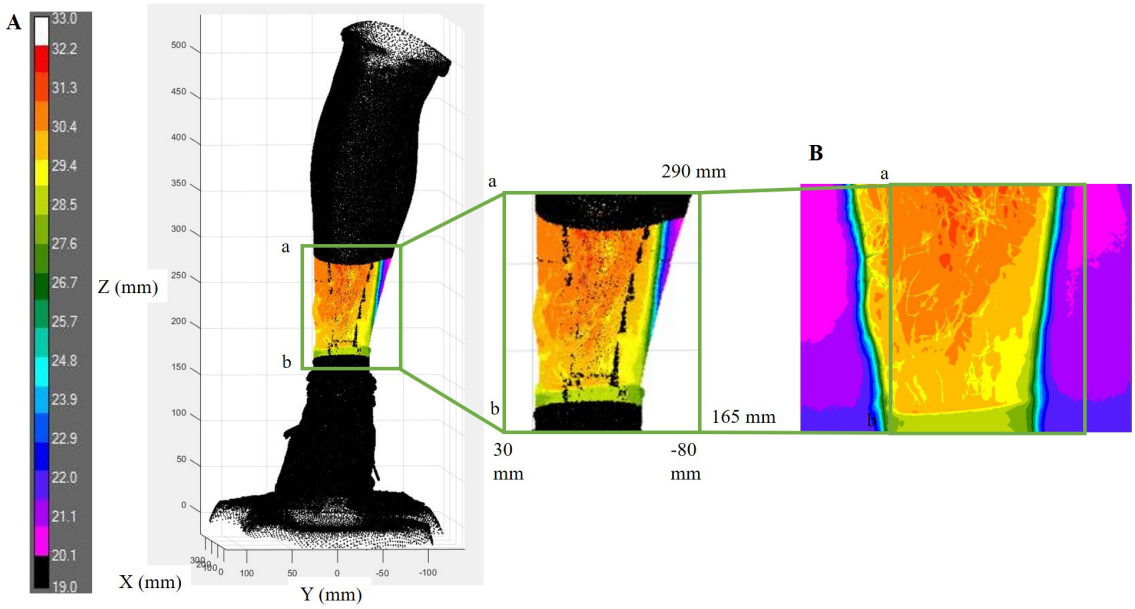

Figure 4.6: A) Result of IR to 3D image registration with background temperature errors and B) the original IR image. The green boxes contain the same region within each image. Note the background temperatures in B appearing in A. All temperatures given in degrees Celsius

Therefore a function that allows the user to crop the images, Figure 4.7, was developed. The

original IR image is displayed and the user is asked if they wish to crop the image. Once the image is cropped, the code determines the reduced temperature matrix and the magnitude and direction of the shift of the center of the cropped image relative to the original image center (h_{shift} and w_{shift}). This information is returned to the main code. The shift parameters are used in determining the $\vec{d}_{shift}$, Equation 4.6, that is used in calculating the image's corners, Equations 3.6 to 3.9.

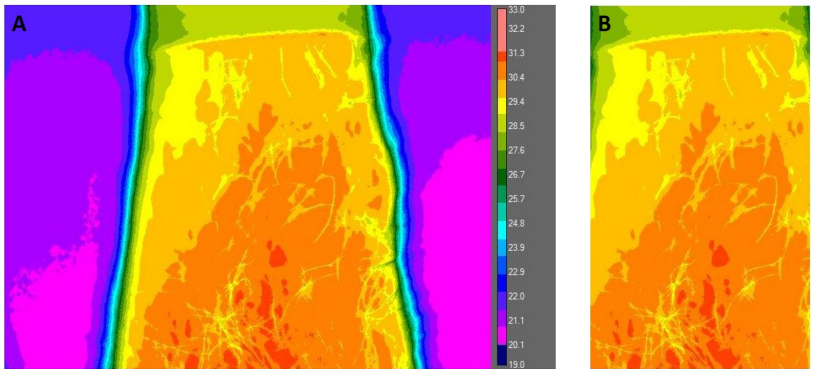

Figure 4.7: IR image A) before and B) after cropping to remove background temperature information. All temperatures given in degrees Celsius

$$\vec{d}_{shift} = h_{shift} * h_{px} * \vec{d}_{up} + w_{shift} * w_{px} * \vec{d}_{left} \tag{4.6}$$

Figures 4.8 and 4.9 show the results of the modified code for the case of a textbook and a right lower leg.

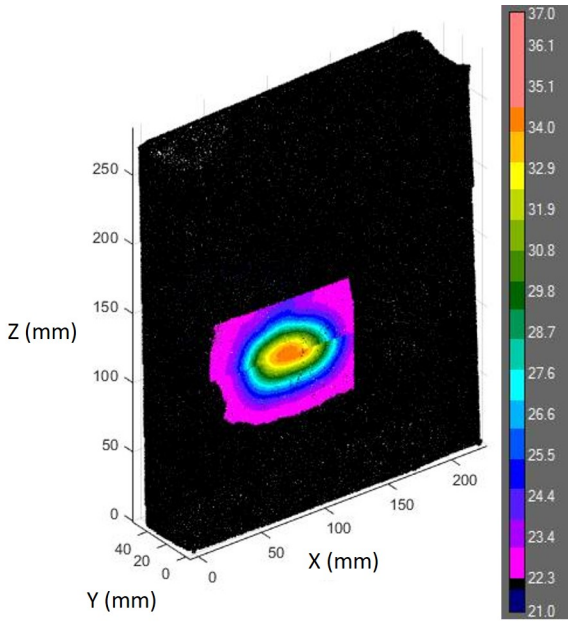

Figure 4.8: Result of developed registration code for two IR images on a 3D image of a textbook. All temperatures given in degrees Celsius

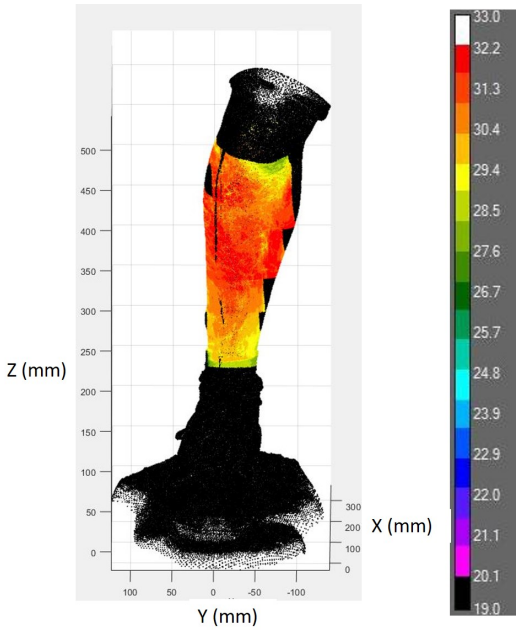

Figure 4.9: Result of developed registration code for four IR images on a 3D image of a right lower leg. All temperatures given in degrees Celsius

Cropping the IR images prior to registration for highly curved surfaces can be expanded to additionally remove potentially inaccurate data. IR images of surfaces more than 60^o from the image view direction can cause errors due to reflected background temperatures [100]. This reflection is the cause of the visible temperature gradient levels between the leg and background, appearing similar to a thermal boundary layer.

4.3.1 Optimize Size of Octree Grid

To increase the operating speed of the code while maintaining the accuracy of the system, a modified Octree data structure was employed. However, there is one parameter that is user defined, the minimum cube size. This determines the number of levels within Octree structure. If the cube size is too large, a significant time is spent determining the faces contained within a cube and testing the face intersections, but if the cube size is too small, a large portion of time is spent iterating through the cube layers. To determine the minimum cube size that allows the code to run

the most efficiently, a series of timed tests with two models of different sizes and various minimum cube sizes. Table 4.3 and Figure 4.10, show the results of the time tests. As the table and graph show, a minimum cube size of 5 appears to be the most efficient. A minimum cube size of 250 was attempted for the leg 3D image, however the run was ended at 13 hours without having completed iterating through the first IR image.

Table 4.3: Number of vertices and faces for each test case and the time for the code to run for each minimum cube size

	Book: 2 images	**Leg: 4 images**
Number of Vertices	385,386	496,477
Number of Faces	771,314	995,501
Minimum Cube Size (mm)	**Code Run Time (min)**	**Code Run Time (min)**
25	18.70	100.92
20	19.34	52.25
15	19.07	47.70
10	11.67	26.07
5	9.64	18.10
1	10.41	24.02
0.5	12.14	25.16

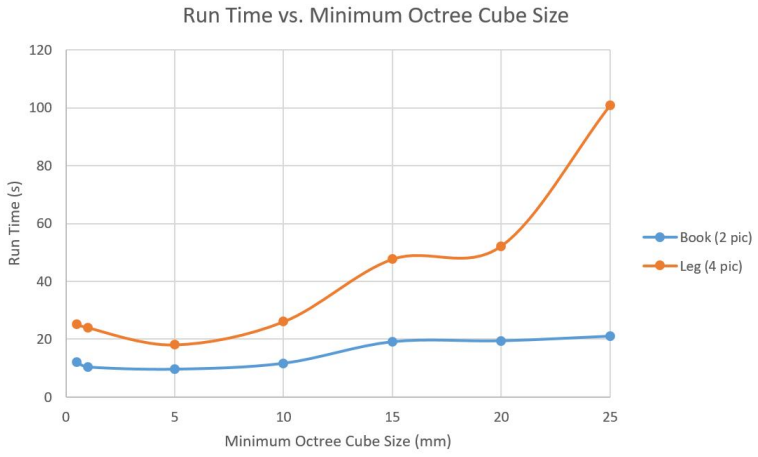

Figure 4.10: Graph of the run time of the IR to 3D registration code for a book with two IR images and a lower leg with four IR images versus the minimum size of the Octree cube

4.4 Fix Tilt Angle

The chosen method to fix the angle of the tilt table is a series of concentric square bars. The full design is shown in Figures 4.11 and 4.12.

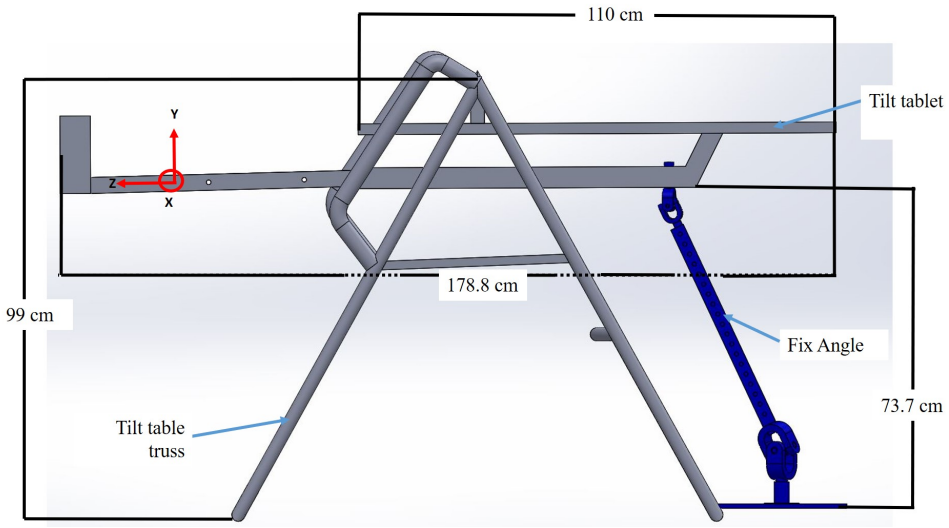

Figure 4.11: Side view of the SOLIDWORKS CAD model of the tilt table and the fix angle device set to 0^o, with relevant dimensions

The bars will be extended to the desired height and a locking rod inserted to fix the length, and therefore tilt angle, Figure 4.13. Table 4.4 provides the distance between the two connection points for all relevant angles. As the distance between the connection points for 90^o (148.2 cm) is more than twice the distance at 0^o (73.7 cm), three bars are required. All three square bars are commercially available. The outer rod has a width of 1.25 in (3.81 mm), a wall thickness of 5/64 in (14 gauge, 0.2 cm) and a series of 3/8 in (0.9525 cm) diameter holes evenly spaced 1 in (2.54 cm) apart down the length of the rod. The middle and inner rods have a width of 1 in (2.54 cm) and $\frac{3}{4}$ in (1.948 cm), respectively, and a thickness of 1/16 in (0.16 cm). A series of holes will be drilled into the middle and inner tube to correspond with the outer rod holes and the proper height for the desired angle. The lock pin is a 4 in (10.16 cm) section of solid steel rod with a diameter of 3/8 in (0.9525 cm), that of the outer rod pre-cut holes.

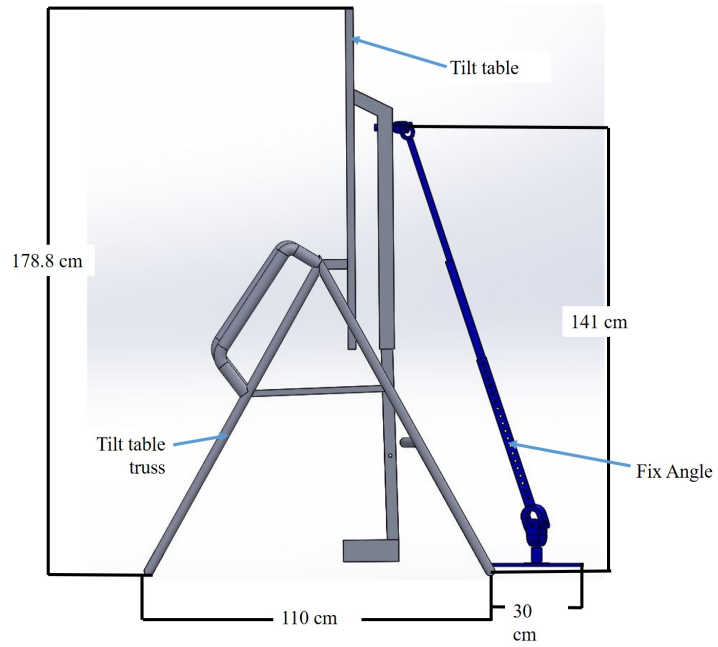

Figure 4.12: Side view of the SOLIDWORKS CAD model of the tilt table and the fix angle device set to 90^o, with relevant dimensions

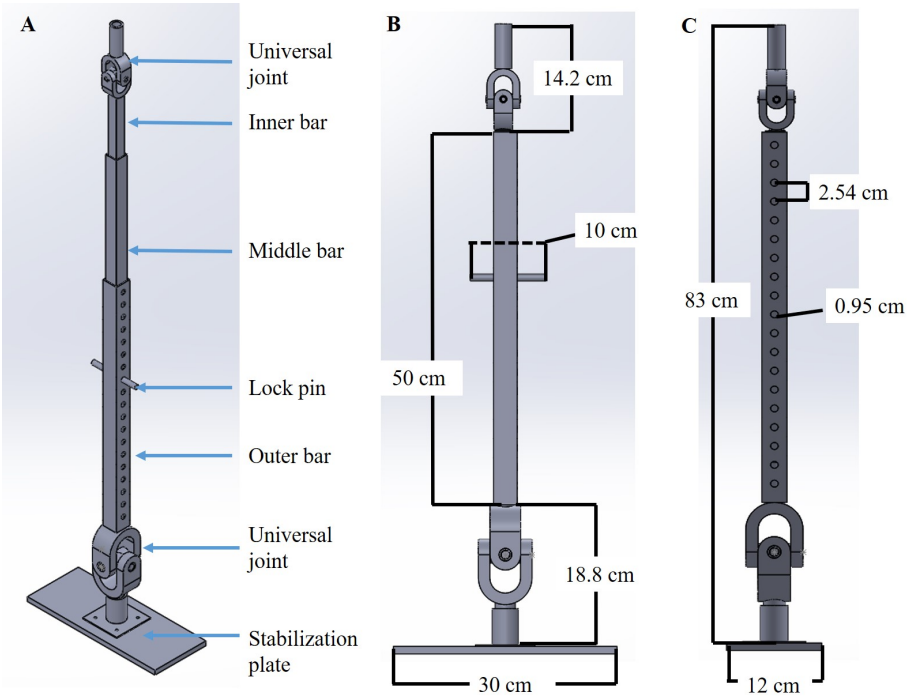

Figure 4.13: SOLIDWORKS CAD of the device to fix the tilt angle of the tilt table. A) CAD with all labeled components, B) Front view of CAD at shortest height with relevant dimensions, and C) Side view of CAD at shortest height with relevant dimensions

Table 4.4: Distance between connection points on the tilt table for angles of interest to simulate microgravity and partial gravity

Tilt Angle	0°	9.5°	10°	20°	22.4°	30°	40°	50°	60°	70°	80°	90°
Distance (cm)	73.7	80.6	81.6	90.9	92.5	100.2	110.3	118.7	128.4	135.8	142.9	148.2

The inner and outer bars connect to universal joints. The upper universal joint connects to a hole in the tilt table metal support bar, and the lower universal joint is fixed with the stabilization plate. To verify the angle for each test, a Milwaukee 4 in Pocket Level will be used, Figure 4.14. Unlike more convectional torpedo levels, this level can be rotated relative to its casing, allowing the operator to set the desired angle. The casing base contains a magnet that allows the level to attach directly to the center metal support bar of the tilt table.

Figure 4.14: The Milwaukee 4 in Pocket Level will be attached to the center metal support bar of the tilt table through magnets, and will allow the operator to verify the tilt angle

4.5 Instrument Mount

Several instrument mount designs were considered. An instrument mount that attaches directly to the table was chosen, Figures 4.15, 4.16, and Figure 4.17, as it allows the instruments to move

with the table.

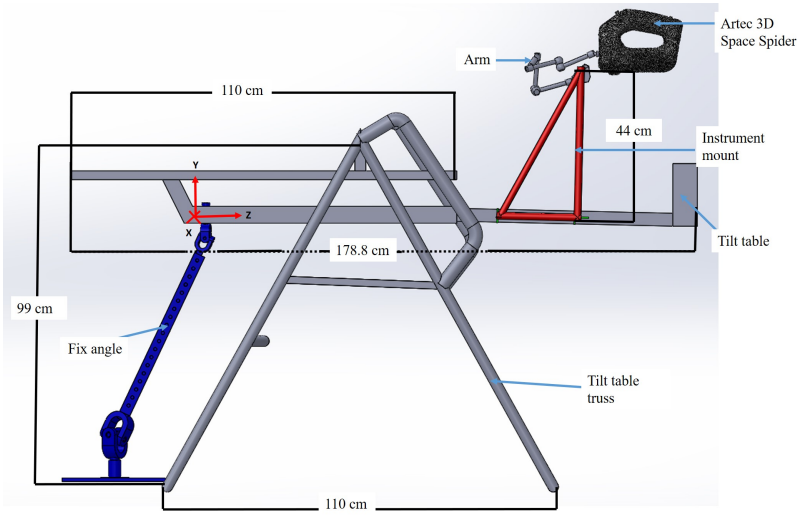

Figure 4.15: SOLIDWORKS CAD of the tilt table, fix angle device, and instrument mount with Artec 3D Space Spider, horizontal

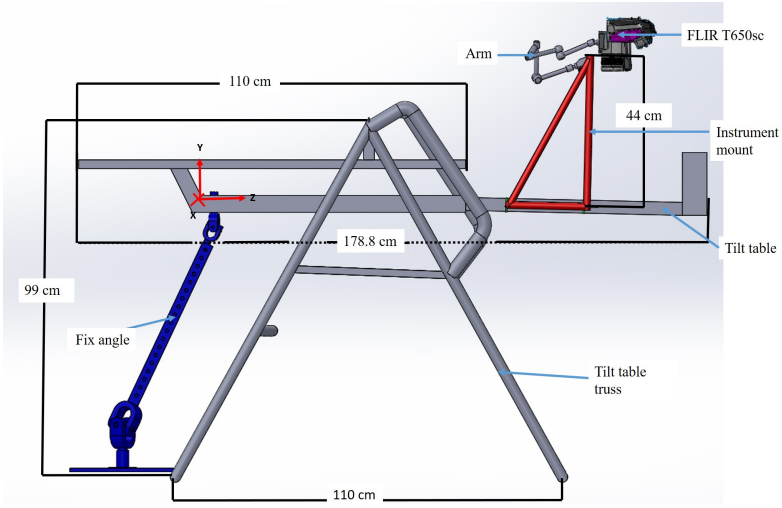

Figure 4.16: SOLIDWORKS CAD of the tilt table, fix angle device, and instrument mount with FLIR T650sc IR camera, horizontal

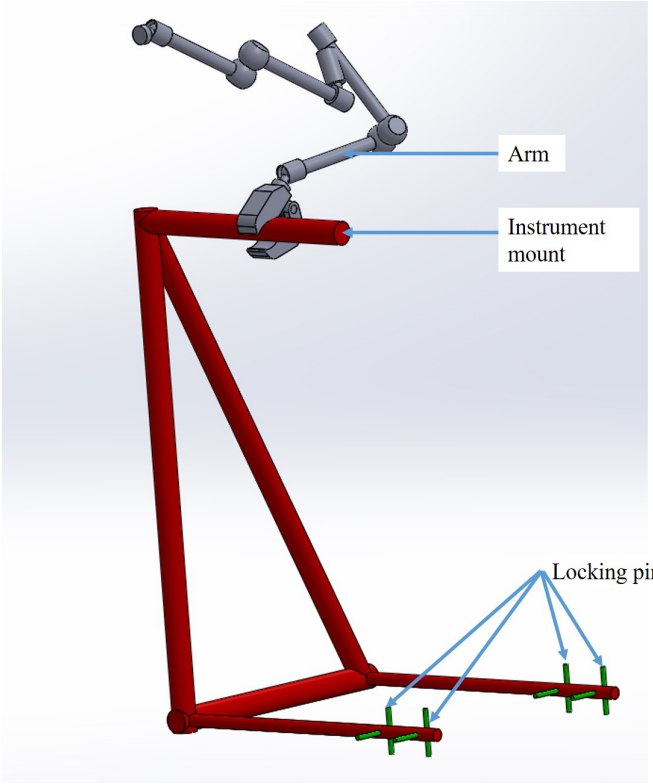

Figure 4.17: SOLIDWORKS CAD design of the instrument mount

The design attaches directly to the center bar of the tilt table in two separate locations to distribute the load and ensure the mount is in a fixed location for all tests. Two rods with a diameter of 1.05 cm fit into pre-existing holes in the center bar with locking pins on either side to hold the mount in place. To allow the IR camera and 3D scanner to be positioned at the desired height over the ROI regardless of the subject, two GryoVu heavy duty dual 11" articulated arms will be used 4.18. The arms consist of four arm sections which can be locked into any position desired with a maximum extended length of 55 cm. The arm attaches to the main structure of the instrument mount via an adjustable clamp, designed to attach to a rod with a diameter of 0.5" to 1.5" (1.2 to 3.8 cm). The mount point of the arm is a $\frac{1}{4}$ in-20 screw, that is required to mount both the FLIR T650sc and Artec Space Spider.

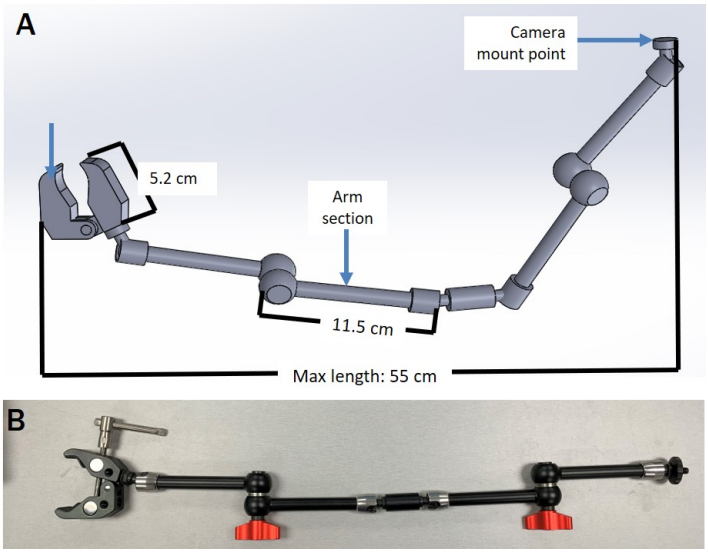

Figure 4.18: A) SOLIDWORKS CAD of the articulated arms and B) picture of a GyroVu articulated arm

The main structure of the instrument mount is shown in Figure 4.19. The diameter of the thin rods that connect the mount to the tilt table was fixed by the existing holes in the center bar of the tilt table to 1.05 cm. The other portions of the mount have a diameter of 1.905 cm (0.75"), chosen to be strong and to be a diameter in the middle of the range onto which the adjustable clamp of the articulating arm could attach. From past experience, similar clamp designs struggle to firmly attach to diameters on the extremes of the listed diameter range. The mount was designed to ensure the triangular brace structure was far enough to the side of the center bar to not interfere with the subjects leg, and extended far enough to not be within either imagers FOV when placed at the desired distance.

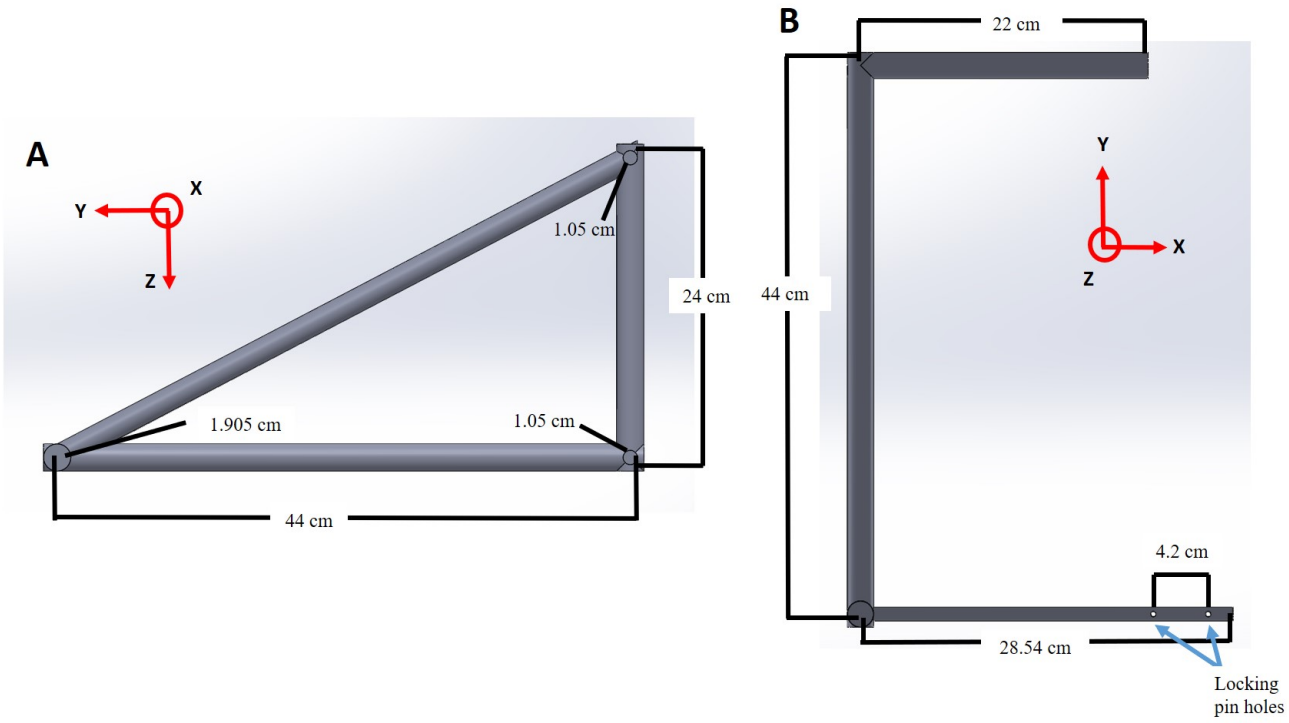

Figure 4.19: SOLIDWORKS CAD of the main structure of the instrument mount with main dimensions A) side view and B) top view

5. DISCUSSION

5.1 IR Camera

The initial proof of concept test with the borrowed FLIR E60 demonstrated that an IR camera is capable of detecting changes in skin temperature (0.5^oC in 30 min) due to a posture change. There were several sources for error in this study. While the temperature and relative humidity were recorded and set as camera parameters at the start of each test period, any variation in these values during the test period could affect the IR readings. During the test period the camera performed multiple NUC processes, which does have an affect on the reported temperature for some pixels. This could have a minor affect on the reported temperatures. All subjects were placed in as consistent of location as possible, however, some variation in location and therefore incident lighting are probable. The potential affects of gender and individual anthropometrics were not considered and are potential sources for uncertainty in the test. The results from the test, along with advice from experts, were used to develop requirements for an IR camera for use in the subject study. After an extensive trade study, the FLIR T650sc was chosen, a high end FLIR IR camera, with a higher resolution, sensitivity, and accuracy than the original FLIR E60 used in the proof of concept. Therefore, the FLIR T650sc should be capable of measuring the change in skin temperature. As previously stated, IR cameras are sensitive to environmental factors, therefore for the subject test the room temperature and relative humidity should be controlled and the lights turned off during IR imaging to reduce the potential reflectivity of the surface and background radiation.

The comparison between the ResearchIR and MATLAB grids showed minimal variation between the two systems, with the largest variation of $\pm 0.1^o$ likely due to rounding. Six of the 264 tested 1 cm grid squares had a variation of $\pm 0.1^oC$ (three images), and none of the 352 0.5 cm grid squares (one image) had a nonzero difference between the two methods. This test served to validate the developed code, which along with the average, maximum, and minimum temperature per grid square, provides additional information in the form of the colored grid square images representing

the average, minimum, and maximum within the grid square. The code reduces the time required to perform the analysis compared to the ResearchIR grids. Though not a deciding factor, this is advantageous. The MATLAB code is more versatile working with any gird size, image distance, and IR camera.

Comparing the results for a series of grid sizes to the original IR image, indicated a pixel should image a 0.1 cm square area of the leg to see the changes in skin temperature due to the presence of superficial vessels, corresponding to a maximum image distance of 144 cm. This test was followed by applying the Johnson's Criteria, which states that for recognition, an object must be spanned by 6 pixels and for identification, by 12 pixels [101], [102], [100]. The criteria was applied to two different vessels and indicated a maximum image distance for recognition of 197 cm and for identification of 98 cm. Therefore for the subject study to ensure identification of a superficial vessel, the operating range of the FLIR T650sc should be constrained from 25 cm to 98 cm.

5.2 3D Scanning

The chosen 3D scanner, the Artec 3D Space Spider, is capable of producing an accurate 3D image. The Artec Eva, a 3D scanner a step below the Space Spider, has been used in the medical industry in the design of facial prostheses [83]. A comparison of measurements performed by hand of a subject's leg and the same measurements on the 3D image were very similar, with a max difference of 0.046 cm. One advantage of the system is the ability to extract any dimensional data desired from the 3D image including: surface distance, straight distance, circumference, cross sectional area, surface area, and volume. This is critical as measuring the leg volume change with tilt is a key component of the human subject study.

5.3 IR to 3D Registration

A code was developed in MATLAB to register IR images onto the 3D image produced by the Artec 3D Space Spider. There is one minor flaw in the code. As Figure 5.1 shows, the code is currently plotting temperature values the sides of the leg, beyond the FOV of the camera when imagining the front of the leg. The exact cause is still unknown, though it is believed to be an error

in the portion of code that determines if the vector between the test point and the camera intersects faces of the 3D image. It should be noted that this error only occurs on the side of the legs, not the back of the leg, nor the book test case. This however, is not a current problem, as the focus is on imaging the front of the subject's leg. Should the lab desire to image other portions of the leg, or the entire leg, this issue will need to be resolved.

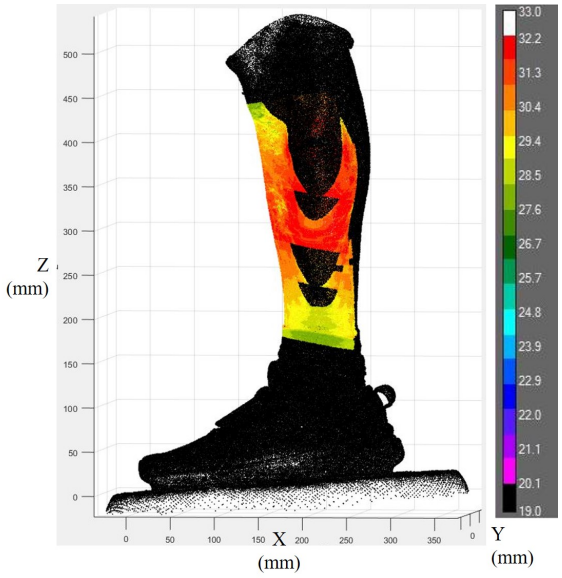

Figure 5.1: Side view of leg 3D image after IR image registration. The color currently wraps around 270^o of the leg due to an error with the face intersection sub routine in the code. All temperatures given in degrees Celsius

Though some work has been performed on reducing the run time of the code without reducing the accuracy of the code, including the minimum cube size of the Octree optimization that was previously discussed, the code currently requires 18 minutes to register four IR images to a 3D image of the leg for a minimum cube size of 5 mm. While speed is not a requirement of the system, should a future project desire more images be registered to a 3D image, a more efficient code would be beneficial. As it is faster for the main code to call functions than to run scripts, portions of the code which are repeatedly called have been transformed into functions [105]. To date, ten functions have been created for portions of the code which are repeatedly use. Where

possible, variables have been preallocated with the max needed size as this is more efficient than resizing arrays as they are created [105].

Ideally, a subfunction of the code would be developed that allows for measurements (circumference, cross sectional area, and volume) of the 3D image to be calculated, post registration. While the Artec Studio software is capable of performing these calculations, it would be advantageous to have the ability to select the desired location for the measurements based on the results of the registration, such as the circumference of a region of localized reduced skin temperature.

Currently, the operator inputs the vectors: $\vec{p}_{from}$, $\vec{d}_{to}$, and $\vec{d}_{up}$. This can be time intensive as the number of images increases as does the risk of mistyping a variable. This could be avoided by creating a function that reads all the needed vectors from a text file.

5.4 Tilt Table

The ideal tilt table for the desired experiment would allow imaging of a subject's entire leg, both the lower leg and thigh, either right or left, mount imaging equipment anywhere, include a digital level, and motor to set the tilt angle as desired. Medical tilt tables, such as Figure 5.2, are available that use electric motors and a digital level for angles ranging from -15^o of head down tilt to 90^o of head up tilt [106]. These systems, however, are expensive and bulky, nor do they include many potential mount points for the instruments directly to the moving potion of the table. Therefore medical tilt tables would require an external structure to be designed that allows the instruments to be normal to the leg surface at all desired test angles, that is simple to operate and ensures consistent instrument placement between tests.

Figure 5.2: Commercially available medical tilt table. Reprinted from [106]

The tilt table, from the modified commercial inversion table, does allow for a larger portion of the leg to be imaged than the flat, standard medical tilt table. Ideally an instrument mount would be designed to take advantage of this, allowing the instruments to move around the leg, imaging a larger portion than the current mount allows. One design challenge is the tilt table truss obscuring portions of the leg when imaging the side of the leg. The distance between the center bar of the tilt table to the side of the truss is 28.5 cm and from the center of a subject's leg to the truss is 22 cm. This does not allow room for the IR camera to be mounted a minimum of 25 cm from the imaged object without the truss obscuring portions of the leg when imaging the side of the leg.

Currently the angle of the tilt table is measured via the Milwaukee 4 in pocket level. To determine the current tilt angle, the operator would be required to rotate the torpedo level in it's casing until bubble is centered in it's tube and then reading the corresponding angle on the scale. This method is imprecise and does not provide exact tilt angle values. Future work might include a trade study and selection of a digital level that will provide the operator with a precise and simple method of verifying the tilt angle.

While the Teeter FitSpine X3 is designed to support a range of heights (56" to 78"), several taller test subjects have commented that the tilt table is painful as the top edge of the table hits their neck, leaving their head unsupported. For the table to achieve a standing posture, the table cannot be extended beyond the setting designed for a height of 62". If extended beyond this setting the foot rest impacts the floor, preventing the table from rotating. Prior to the human subject test, a

simple device to extend the top of the table needs to be designed, providing the necessary support for subject comfort. Similarly, the foot rest, designed for short periods of use with the majority of the user's time spent in a head down tilt position, is uncomfortable for extended periods of standing. A replacement of the foot rest, or at a minimum an extension of the current rest, will be required prior to the human subject study, as the subject will be required to stand for a period of time to acquire the 1g (9.81 m/s^2) baseline, and the higher partial gravity levels (higher angles) will require the subject to support a portion of their weight. Similar to medical tilt tables, a system of straps might be required to hold the subject in place against the table.

5.5 Recommendations for Subject Study

Through the literature review, and development of instrumentation and software to be used in the final subject study, some requirements and limitations of the study were determined.

All subject's will be required to wear shorts during all tests, as the IR camera detects surface temperatures, and the temperature of clothing does not reflect that of the skin. Those subjects required to change into shorts must do so prior to the start of the experiment to ensure sufficient time for the subject to acclimate to the room environment.

The study should allow sufficient time in each posture for a new thermoequilibirum to be established, including the initial baseline standing posture. Based on the temperature trend data from the IR camera proof of concept, this time limit should be on the order of 30 min, as a portion of the subject's skin temperature had started to plateau between 24 and 30 min, though not all subjects.

As Figure 5.3 demonstrates, the FLIR T650sc, particularly at close distances, occasionally records the temperature of hair and not the skin surface. Therefore to avoid these errors, subjects will be asked to shave the ROI (right lower leg) prior to the test.

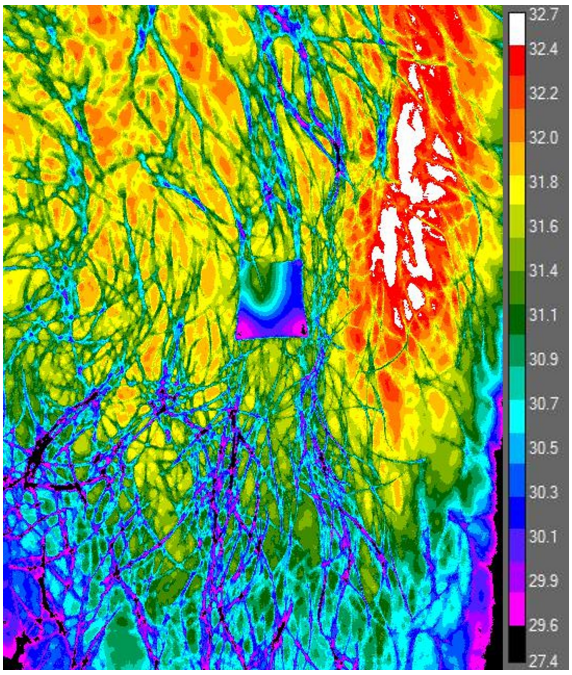

Figure 5.3: IR image of subject's leg at a distance of 25 cm, note the large temperature errors caused by the IR camera detecting the hair temperature, not the skin temperature. All temperatures given in degrees Celsius

Should multiple testing days of a single subject be required, the tests will occur at the same time of day to minimize the effects of the circadian rhythm on skin temperature, which is largest in the extremities, such as the lower leg [37], [77]. Subjects will be asked to refrain from exercise on the day of the test, not eat the two hours prior to testing, drink alcohol the eight hours prior to testing, and not consume caffeine the six hours prior to testing [37], [75], [77]. Individuals with a history of smoking or any known circulatory abnormalities should be restricted from participating as both have been shown to have an effect on skin temperature [75]. The room environment should be controlled including: room temperature, relative humidity, ambient light, and air circulation.

To ensure that the IR camera is capable of detecting temperature variation due to superficial vessels, the IR camera shall not be placed more than 98 cm from the subject's leg. Multiple IR images should be taken over a period of time in the standing posture to ensure accurate baseline skin temperatures are achieved prior to introducing tilt. Prior to IR imaging, the camera should be turned on and allowed to warm up, typically requiring five minutes.

5.5.1 Power Analysis to Determine Optimum Sample Size for Future Research

A two-sided t-test power analysis was performed to determine the minimum number of subjects to include in the study to achieve statistically significant results. The null hypothesis for the analysis and subject study is that the difference between the standing and supine leg skin temperature is zero. The alternate hypothesis is that there is a difference between the two skin temperatures.

The power analysis method uses the effect size, desired significance level (α), associated Student t-scores, and power level to calculate the number of subjects required per Equation 5.1 [107], [108]. The analysis was run with both an α of 0.01 and 0.05, and the power level varied from 0.8 to 0.95. The effect size can be calculated by Equation 5.2, where μ is the mean of the data set, μ_o is the hypothesized mean, and σ is the standard deviation of the data set [108]. If these values are unknown, the standard is to set the effect size to 0.8 [107], [108]. The analysis is initially run with the degrees of freedom (df) set to infinity, and then iterated through with the df set to one less than the previous iteration's number of subjects until the number of subjects remains constant.

$$Number\ of\ subjects = \frac{(t_{(1-\frac{\alpha}{2}),df} + t_{power,df})^2}{(effect\ size)^2} \tag{5.1}$$

$$Effect\ size = \frac{\mu - \mu_o}{\sigma} \tag{5.2}$$

Table 5.1 presents the results of the power analysis with the standard effect size of 0.8. To achieve a power of 0.95, corresponding to a Type II error, or not rejecting the null hypothesis when it is incorrect, risk of 0.05 [107] and a Type I error of 0.01, a minimum of 31 subjects is required.

Table 5.1: Results of a power analysis to determine the minimum number of subjects required for the study with recommend effect size of 0.8 if the value is unknown

Power	Alpha	Effect Size	Number of subjects
0.8	0.01	0.8	22
0.9	0.01	0.8	27
0.95	0.01	0.8	31
0.8	0.05	0.8	15
0.9	0.05	0.8	19
0.95	0.05	0.8	23

Table 5.2 presents the results of the same analysis, however the effect size was calculated based on the results from the proof of concept test performed with the FLIR E60. The calculated mean change in skin temperature was 0.5^{o}C with a standard deviation of 0.507^{o}C. The hypothesized mean is 0^{o}C as the purpose of the test is to determine if a change in skin temperature occurs. Equation 5.2, with the given parameters, gives an effect size of 0.987. A minimum of 22 subjects is required for a power of 0.95 and an alpha of 0.01.

Table 5.2: Results of a power analysis to determine the minimum number of subjects required for the study with estimated effect size based on results from the proof of concept

Power	Alpha	Effect Size	Number of subjects
0.8	0.01	0.987	16
0.9	0.01	0.987	19
0.95	0.01	0.987	22
0.8	0.05	0.987	11
0.9	0.05	0.987	13
0.95	0.05	0.987	16

Based on the analyses of the proof of concept in Table 5.2 and anticipated future studies which will require IRB and peer review, it is recommended that measurements be made on a minimum sample size of 22, assuming a power of 0.95, alpha of 0.01 and an assumed effect size of 0.987. It is also assumed that the temperature distribution will be no less than that of the proof of concept

experiment.

5.6 Future work

5.6.1 IR to 3D Registration

As previously discussed, though not currently a problem, the registration code maps portions of the back of the leg, though not visible to the IR camera. This is likely due to a minor bug in the portion of the code that detects face intersections. Interestingly, the error only appears on the leg test case, not the book.

The code currently requires 18 min to register four IR images to the 3D image of the lower leg. Should future work including mapping the skin temperature of the entire lower leg, work on further optimizing the code may be required. A function may be developed that reads a text file with all the relevant input parameters including image specific vectors.

5.6.2 Tilt Table

The device to fix the tilt angle of the table and the instrument mount will be construted. Several minor tilt table modifications are necessary prior to the final subject study. An extension of the top of the tilt table will need to be designed to provide the necessary neck and head support for taller subjects whose heads extend beyond the top of the tilt table. The current foot rest was designed for a person to stand on them for a short periods, but are uncomfortable for extended periods. Therefore, the foot rest will need to be extended or redesigned to be comfortable for extended periods of the subject standing.

6. CONCLUSIONS

The intent of this thesis research was to design a suite of instruments and software which could be applied to collecting human lower body thermal data in variety of 'postures' which simulate altered gravity conditions. This data could then be used to inform the redesign of the LCVG through both ground based research as well as the future development of a flight experiment on board the International Space Station (ISS). The following conclusions can be made with respect to this research.

6.1 IR Camera

An initial proof of concept test was performed with a borrowed IR camera (FLIR E60) to test if an IR camera can detect changes in skin temperature due to a change in posture. The test demonstrated that an IR camera could detect a skin temperature change, with an average drop in skin temperature of 0.5^{o}C after 30 min supine compared to a standing baseline. Based on the results of this test and suggestions from experts, a series of requirements for an IR camera were established and an extensive trade study was performed, which determined the FLIR T650sc was the best IR camera for the purpose of our experiment.

A method to determine the average temperature within a 1 cm grid square was initially developed in ResearchIR Max, a software developed by FLIR. This method, however, required separate grids to be created, by hand, for any grid size and image distance. For smaller grid sizes, the pattern had to be saved as multiple separate files. A MATLAB code was developed to be a more versatile tool capable of producing the same results as a grid developed in ResearchIR. The code calculates the maximum, minimum and average temperature within a grid square of any size, any image distance, and any IR camera. The results are published in a text file for future reference which can easily be exported into Excel for further analysis. A series of images are displayed with a grid square colored to correspond to the maximum, minimum, and average temperature, providing a visual representation of the data not achievable with ResearchIR. A comparison of grid tempera-

ture average values for multiple images for both a 1 cm and a 0.5 cm grid was used to validate the MATLAB code with a max difference between the two results of $\pm 0.1^o$ due to rounding.

A series of varying grid sizes were applied to two IR images of superficial vessels and indicated a grid size of 0.1 cm was sufficient to see a temperature variation across the vessel, equivalent to a maximum image distance of 144 cm. This result is similar to that obtained with the Johnson's criteria for the same vessels, which indicated a maximum image distance of 197 cm for recognition and 98 cm for identification.

6.2 3D Scanner

An extensive trade study was performed on 3D scanners, and the Artec 3D Space Spider was selected. A comparison of five measurements calculated by the associated Artec Studio software of a 3D image of a subject's leg and hand measurements indicated a close correlation between the values. This served to verify the ability of the scanner and software to create an 3D image of a scanned object. The Artec Studio is capable of calculating a variety of measurements including: surface distance, straight line distance, circumference, cross sectional area, and volume.

6.3 IR to 3D Registration

A MATLAB code was developed to register IR images to a 3D image based on the work of Dr. Adam Chromy. To reduce the potential for error due to background temperature registering to the 3D image and inaccurate temperature values due to the curvature of the leg, a subfuction was created that allows the user to crop an IR image. This does not affect where the temperature values are registered. A series of timed tests of the code with two different 3D images with varied minimum cube size was performed. The tests indicate a minimum Octree cube size of 5 mm is the most efficient.

6.4 Tilt Table

The Teeter FitSpine X3 tilt table was chosen for the subject test to simulate the fluid shift due to microgravity and partial gravity. As the tilt table did not have a method of fixing the angle from 0^o and 90^o a system was designed. A series of three concentric square tubes with fixed ends can

be extended and held to a set length by a locking pin. A device to mount the IR camera and 3D scanner was developed, Figure 6.1, allowing imaging of a subject's right lower leg, the chosen ROI.

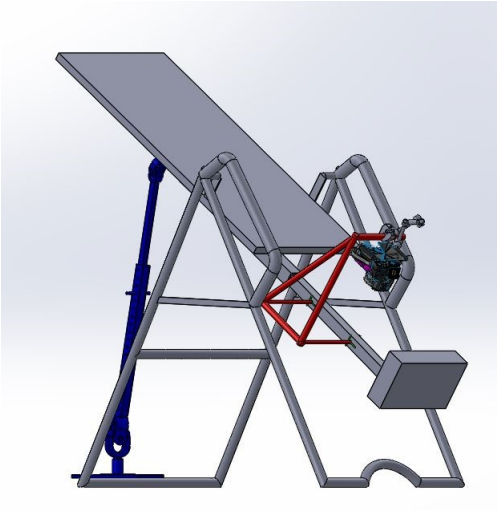

Figure 6.1: The SOLIDWORKS CAD of the tilt table, fix angle device, and instrument mount with the FLIR T650sc

6.5 Sample Size for Human Subject Data Collection

While the proof of concept measurements with an IR camera indicated a decreasing trend in skin temperature as a function of posture changes from vertical to horizontal, it was clear from the means and standard deviations that future studies will benefit from a larger sample size and perhaps a longer duration in the horizontal posture. A statistical analysis suggests that if the temperature range change remains the same, a sample size of at least 22 subjects will provide data which is more statistically significant.

REFERENCES

[1] D. R. Jenkins, *Dressing for Altitude: U.S. Avation Pressure Suits–Wiley Post to Space Flight*. National Aeronautics and Space Administration, 2012, accessed on Feb. 13, 2020. [Online]. Available: https://www.nasa.gov/pdf/683215main_DressingAltitude-ebook.pdf

[2] A.-L. Paul and R. J. Ferl, "The biology of low atmospheric pressure - implications for exploration mission design and advnaced life support," *Gravitational and Space Biology*, vol. 19, no. 2, pp. 3–18, 2006.

[3] R. Connor, "Remembering wiley post and will rogers," Webpage, Smithsonian National Air and Space Museum, 2013, accessed on Feb. 13, 2020. [Online]. Available: https://airandspace.si.edu/stories/editorial/remembering-wiley-post-and-will-rogers

[4] W. Ayrey, "Ilc space suits & related products," 2007, accessed on Feb. 13, 2020. [Online]. Available: https://www.hq.nasa.gov/alsj/ILC-SpaceSuits-RevA.pdf

[5] National Air and Space Museum, "Pressure suit, mark iv, united states navy," Internet, Smithosonian National Air and Space Museum, accessed on Feb. 13, 2020. [Online]. Available: https://airandspace.si.edu/collection-objects/pressure-suit-mark-iv-united-states-navy-1

[6] D. S. F. Portree and R. C. Trevino, *Walking to Olympus: An EVA Chronology*. NASA History Office, 1997, accessed on Feb. 13, 2020. [Online]. Available: http://aresinstitute.org/spacepdf/EVACron.pdf

[7] P. Rincon, "The first spacewalk: How the first human to take steps in outer space nearly didn't return to earth," Webpage, BBC News, 2014, accessed on Feb. 13, 2020. [Online]. Available: https://www.bbc.co.uk/news/special/2014/newsspec_9035/index.html

[8] "Eva at 50: Comsmonaut alexei leonov took first spacewalk 50 years ago," Webpage, 2015, accessed on Feb. 13, 2020. [Online]. Available: http://www.collectspace.com/news/

news-031815a-spacewalk-50th-alexei-leonov.html

[9] D. R. Williams, "The first u.s. spacewalk - gemini 4," Webpage, NASA Space Science Data Coordinated Archive, 2015, accessed on Feb. 13, 2020. [Online]. Available: https://nssdc.gsfc.nasa.gov/planetary/gemini_4_eva.html

[10] Midwest Research Institute, "Liquid cooled garment," 1975.

[11] NASA. (2018) Buzz aldrin on the moon. NASA. Accessed on Feb. 24, 2020. [Online]. Available: https://www.nasa.gov/mission_pages/apollo/40th/images/apollo_image_12.html

[12] E. Mahoney. (2019) Spacewalk spacesuit basics. NASA. Accessed on Jan. 6, 2020. [Online]. Available: https://www.nasa.gov/feature/spacewalk-spacesuit-basics

[13] D. R. Williams. (2020) Moon fact sheet. NASA Space Science Data Coordinated Archive. Accessed on Feb. 13, 2020. [Online]. Available: https://nssdc.gsfc.nasa.gov/planetary/factsheet/moonfact.html

[14] M. Valladares. (2019) Suits through the eras, part ii: The builder. National Aeronautics and Space Administration. Accessed on Feb. 17, 2020. [Online]. Available: https://roundupreads.jsc.nasa.gov/pages.ashx/1315/Suits%20Through%20the%20Eras%20Part%20II%20The%20Builder

[15] UTC Aerospace Systems, *NASA Extravehicular Mobility Unit (EMU) LSS/SSA Data Book*, 2017, publicly released per JSC-E-DAA-TN55224, Accessed on Feb. 17, 2020. [Online]. Available: https://www.lpi.usra.edu/lunar/constellation/NASA-EMU-Data-Book-JSC-E-DAA-TN55224.pdf

[16] M. Izenson, W. Chen, S. Philips, A. Chepko, G. Bue, J. Ferl, and D. Cencer, "Multifunctional cooling garment for space suit environment control," in *45th International Conference on Environmental Systems*, 2015.

[17] L. van Broock and P. de Leon, "Development of a liquid cooling garment for the ndx-1 prototype," in *42nd International Conference on Environmental Systems*, 2012.

[18] G. Bue, C. Watts, R. Rhodes, I. Anchonod, D. Westheimer, C. Campbell, M. Vogel, B. Conger, and J. Stein, "Experimentally determined overall heat transfer coefficients for spacesuit liquid cooled garments," in *45th International Conference on Environmental Systems*, 2015.

[19] B. Webbon, L. Montgomery, L. Miller, and B. Williams, "A comparision of three liquid-ventilation cooling garments during treadmill exercise," *Aviation Space and Environmental Medicine*, vol. 52, no. 7, pp. 408–415, 1981.

[20] J. Rugh, C. Kind, H. Paul, L. Trevino, and G. Bue, "Phase ii testing of liquid cooling garments using a sweating manikin, controlled by a human physiological model," in *36th International Conference on Environmental Systems*, 2006.

[21] R. Rhodes, G. Bue, I. Meginnis, M. Hakam, and T. Radford, "Thermal performance testing of emu and csafe liquid cooling garments," in *43rd International Conference on Environmental Systems*, 2013.

[22] M. Kesterson, G. Bue, and L. Trevino, "Wissler simulations of a liquid cooled and ventilation garment (lcvg) for extravehicular activity (eva)," in *36th International Conference on Environmental Systems*, 2006.

[23] V. S. Koscheyev, J. Warpeha, G. R. Leon, J.-H. Kim, B. Fink, M. L. Gernhardt, and N. G. Skytland, "The advaned design of a liquid cooling garment through long-term research: implications of the test results on three different garments," in *39th International Conference on Environmental Systems*, 2009.

[24] B. Dunbar, "Learn about spacesuits," Webpage, 2014, accessed on Feb. 13, 2020. [Online]. Available: https://www.nasa.gov/audience/foreducators/spacesuits/home/clickable_suit_nf.html

[25] C. T. O. J. Goser, "Results of a dynamic liquid cooling garment simulation in v-suit," in *44th International Conference on Environmental Systems*, 2014.

[26] A. Kauderer, "Sts-129 shuttle mission imagery: Astronaut randolph j. (randy) bresnik, mission specialist," Webpage, National Aeronautics and Space Administration:

Human Spaceflight, 2009, accessed on Feb. 13, 2020. [Online]. Available: https://www.spaceflight.nasa.gov/gallery/images/shuttle/sts-129/html/jsc2009e173054.html

[27] S. M. Fortney, "Exercise thermoregulation: Possible effects of spaceflight," in *21st International Conference on Environmental Systems*, 1991.

[28] "Personal conversations with professor bonnie j. dunbar, ph.d. professor dunbar is a 5-time space shuttle astronaut (sts-61-a, sts-32, sts-50, sts-71, and sts-89)."

[29] B. M. Anderson, J. E. Nealy, G. D. Qualls, P. J. Staritz, J. W. Wilson, M.-H. Y. Kim, F. A. Cucinotta, W. Atwell, G. D. Angelis, J. Ware, and A. E. Persans, "Shuttle spacesuit (radiation) model development," *SAE Technical Papers*, 2001.

[30] J. E. Hall, *Body Temperature Regulation and Fever*, 13th ed. Elsevier, Inc., 2016.

[31] E. Arens and H. Zhang, *The skin's role in human thermoregulation and comfort*. Woodhead Publishing Limited, 2006, ch. 16, pp. 560–597.

[32] A. C. Stahn, A. Werner, O. Opatz, M. A. Maggioni, M. Steinach, V. W. von Ahlefeld, A. Moore, B. E. Crucian, S. M. Smith, S. R. Zwart, T. Schlabs, S. Mendt, T. Trippel, E. Koralewski, J. Koch, A. Chouker, G. Reitz, P. Shang, L. Rocker, and H.-C. G. K. A. Kirsch, "Increased core body temperature in astronauts during long-duration space missions," *Scientific Reports*, no. 7, 2017.

[33] J. M. Waligora, "The physiological basis for spacecraft environmental limits," pp. 57–67, 1979.

[34] T. L. Bergman and A. S. Lavine, *Fundamentals of Heat and Mass Transfer*, 8th ed. John Wiley & Sons, Inc., 2017.

[35] V. Bernard, E. Staffa, V. Mornstein, and A. Bourek, "Infrared camera assement of skin temperature-effect of emissivity," *Physica Medica*, vol. 29, no. 6, pp. 583–591, 2013.

[36] G. Tanda, "Skin tempreature measurements by infrared thermography during running exercise," *Experimental Thermal and Fluid Science*, vol. 71, pp. 103–113, 2016.

[37] C. M. A. Costa, D. G. Moreira, M. Sillero-Quintana, C. J. Brito, G. de A. Pussieldi, A. de A. Fernandes, S. P. Cano, and J. C. B. Marins, "Daily rhythm of skin temperature of women evaluated by infrared thermal imaging," *Journal of Thermal Biology*, vol. 72, pp. 1–9, 2018.

[38] A. Bach, I. B. Steward, G. M. Minett, and J. T. Costello, "Does the technique employed for skin temperature assessment alter outcomes? a systematic review," *Physiological Measurements*, vol. 6, no. 9, pp. 27–51, 2015.

[39] M. J. Buono, A. Jechort, R. Marques, C. Smith, and J. Welch, "Comparision of infrared versus contact thermometry for measuring skin temperature during exercise in heat," *Physiological Measurement*, vol. 28, no. 8, pp. 855–859, 2007.

[40] R. R. Gonzalez, "Problems of heat exchange and exercise during long-term space operations: use of a thermoregulatory model to describe physiologic response," in *Proc. of 32nd International Conference on Environmental Systems*, 2002.

[41] V. S. Koscheyev, G. R. Leon, and R. C. Trevino, "Maximal conductive heat exchange through different body zones in a liquid cooling/warming space garment," in *30th International Conference on Environmental Systems*, 2000.

[42] H. Zhang, "Human thermal sensation and comfort in transient and non-uniform thermal environments," Ph.D. dissertation, 2003.

[43] B. W. Olesen and P. O. Fanger, "The skin temperature distribution for resting man in comfort," *Archives des sciences physiologiques*, vol. 27, p. A385 to A393, 1973.

[44] O. Jones, "Arteries of the lower limb," Webpage, TeachMeAnatomy.com, 2018, accessed on Jan. 11, 2020. [Online]. Available: https://teachmeanatomy.info/lower-limb/vessels/arterial-supply/

[45] A. A. Romanovsky, "Skin temperature: its role in thermoregulation," *Acta Physiologica*, vol. 210, pp. 498–507, 2014.

[46] O. Jones, "Venous drainage of the lower limb," Webpage, TeachMeAnatomy.com, 2018, accessed on Jan. 11, 2020. [Online]. Available: https://teachmeanatomy.info/lower-limb/vessels/venous-drainage/

[47] S. Standring, *Leg*, 41st ed. Elsevier, 2016, ch. 83, pp. 1400–1417.

[48] S. Standring, *Pelvic girdle, gluteal region and thigh*, 41st ed. Elsevier, 2016, ch. 80, pp. 1335–1375.

[49] "Cardiovascular system of the leg and foot," Webpage, Anatomy Medicine, 2020, accessed Jan. 11, 2020. [Online]. Available: https://anatomy-medicine.com/cardiovascular-system/132-the-cardiovascular-system-of-the-leg-and-foot.html

[50] H. Sandler, "Cardiovascular effects of weightlessness and ground-based simulation," NASA, Tech. Rep., 1988.

[51] W. E. Thornton, T. P. Moore, and S. L. Pool, "Fluid shifts in weightlessness," *Aviation, Space, and Environmental Medicine*, vol. 58, pp. A86–A90, 1987.

[52] A. R. Hargens and L. Vico, "Long-duration bed rest as an analog to microgravity," *Journal of Applied Physiology*, vol. 120, pp. 891–903.

[53] G. Clement, *The Cardio-Vascular System in Space*, 2nd ed. Springer, 2011, ch. 4.

[54] C. S. Leach, L. D. Inners, and J. B. Charles, "Changes in total body water during space-flight," *Jounral of Clinical Pharmacology*, vol. 31, no. 10, pp. 1001–1006, 1991.

[55] R. S. Johnston and L. F. Dietlein, Eds., *Biomedical Results from Skylab*. NASA Johnson Space Center, Scientific and Technical Information Office, 1977, no. NASA SP-377.

[56] G. W. Hoffler, S. A. B. Jr., and A. E. Nicogossian, "In-flight lower limb volume measurement," pp. 63–68, 1977.

[57] T. P. Moore and W. E. Thornton, "Space shuttle inflight and postflight fluid shifts measured by leg volume changes," *Aviation, Space, and Environmental Medicine*, vol. 58, pp. A91–A96, 1987.

[58] J. B. Charles and S. W. Boettcher, "Extended duration orbiter medical project countermeasure to reduce post space flight orthostatic intolerance (lbnp) - sts-50/usml-1 ," in *Joint "L+1" Review for USML-1 and USMP-1*, no. N95-14224, 1993.

[59] F. Louisy, P. Schroiff, and A. Guell, "Changes in leg vein filling and emptying characteristics and leg volumes during long-term head-down bed rest," *Journal of Applied Physiology*, vol. 82, no. 6, pp. 1726–1733, 1997.

[60] D. E. Watenpaugh, J. C. Buckey, L. D. Lane, F. A. Gaffney, B. D. Levine, S. J. W. W. E. Moore, and C. G. Blomqvist, "Effects of spaceflight on human calf hemodynamics," *Journal of Applied Physiology*, vol. 9, no. 4, pp. 1552–1558, 2001.

[61] N. Y. Panferova and T. A. Kabesheva, "Dynamics of fluid turnover in human extremities as related to different body positions," *USSR: Space Biology and Aerospace Medicine*, vol. 21, no. 2, pp. 57–64, 1987.

[62] "Sts-50 usml-1 onboard photograph," Webpage, NASA, 1992, accessed on Jan. 8, 2020. [Online]. Available: https://ntrs.nasa.gov/search.jsp?R=MSFC-9402320&qs=t%3D0%26N%3D125%2B4294955194%2B4294965987

[63] F. J. Baisch and G. Petrat, "Body fluid distribution in man in space and effect of lower body negative pressure treatment," *The Clinical Investigator*, vol. 71, pp. 690–699, 1993.

[64] D. E. Watenpaugh, "Analogs of microgravity: head-down tilt and water immersion," *Journal of Applied Physiology*, vol. 120, p. 9, 2016.

[65] T. N. Krupina, B. M. Fyodorov, L. M. Filatova, N. I. Tsyganova, and E. I. Matsnev, "Effect of antiorthostatic bed rest on the human body," *Life Sciences and Space Research*, vol. 14, pp. 285–287, 1976.

[66] L. I. Kakurin, V. I. Lobachik, V. M. Mikhailov, and Y. A. Senkevich, "Antiorthostatic hypokinesia as a method of weightlessness simulation," *Aviation, Space, and Environmental Medicine*, pp. 1083–1086, 1976.

[67] H. Sandler and A. I. Grigoriev, "Joint u.s./u.s.s.r. study: Comparison of effects of horizontal and head-down bed rest," 1990.

[68] N. M. Navasiolava, M.-A. Custaud, E. S. Tomilovskaya, I. M. Larina, T. Mano, G. Gauquelin-Koch, C. Gharib, and I. B. Kozlovskaya, "Long-term dry immersion: review and prospects," *European Journal of Applied Physiology*, vol. 111, pp. 1235–1260, 2011.

[69] Y. Barr, G. Clement, and P. Norsk, "Human health countermeasures–partial-gravity analogs workshop," 2016.

[70] A. Merla, L. D. Donato, and G. L. Romani, "Infrared functional imaging: analysis of skin temperature during exercise," in *Proc. of 2nd Joint EMBS/BMES Conference*, 2002, pp. 1141–1142.

[71] J. E. Gold, M. Cherniack, and B. Buchholz, "Infrared thermography for examination of skin temperature in the dorsal hand of office workers," *European Journal of Applied Physiology*, vol. 93, no. 1-2, pp. 245–251, 2004.

[72] C.-L. Huang, Y.-W. Wu, C.-L. Hwang, Y.-S. Jong, C.-L. Chao, W.-J. Chen, Y.-T. Wu, and W.-S. Yang, "The application of infrared thermography in evaluation of patients at high risk of lower extremity peripheral arterial disease," *Journal of Vascular Surgery*, vol. 54, no. 4, pp. 1074–1080, 2011. [Online]. Available: https://reader.elsevier.com/reader/sd/pii/S0741521411008391?token=01119D78CB2BBD84516C6B1CBD87BE515C7E5D29070712D0DA4D611E8ED2A417F79486E95110

[73] A. Cholewka, A. Stanek, A. Klimas, A. Sieron, and Z. Drzazga, "Thermal imaging application in chronic venous disease," *Journal of Thermal Analysis and Calorimetry*, no. 115, pp. 1609–1618, 2014. [Online]. Available: https://link.springer.com/article/10.1007/s10973-013-3356-0

[74] S. Sivanandam, M. Anburagan, B. Venkatraman, M. Menaka, and D. Sharath, "Medical thermography: a diagnostic approach for type 2 diabetes based on non-contact infrared thermal imaging," *Endocrine*, vol. 42, pp. 343–351, 2012.

[75] D. G. Moreira, J. T. Costello, C. J. Brito, J. G. Adamczyk, K. Ammer, A. J. Bach, C. M. Costa, C. Eglin, A. A. Fernandes, I. Fernandez-Cuevas, J. J. Ferreira, D. Formenti, D. Fournet, G. Havenith, K. Howell, A. Jung, G. P. Kenny, E. S. Kolosovas-Machuca, M. J. Maley, A. Merla, D. D. Pascoe, J. I. P. Quesada, R. G. Schwartz, A. R. Seixas, J. Selfe, B. G. Vainer, and M. Sillero-Quintana., "Thermographic imaging in sports and exercise medicine: A delphi study and consensus statement on the measurement of human skin temperature," *Journal of Thermal Biology*, vol. 69, pp. 155–162, 2017.

[76] L. Beckmann, S. Hahne, G. Medrano, S. Kim, M. Walter, and S. Leonhardt, "Monitoring change of body fluids during physical exercise using bioimpedance spectroscopy," in *31st Annual International Conference of the IEEE EMBS*, 2009.

[77] J. C. B. Marins, A. A. Fernandes, S. P. Cano, D. G. Moreira, F. S. da Silva, C. M. A. Costa, I. Fernandez-Cuevas, and M. Sillero-Quintana, "Thermal body patterns for healthy brazilian adults (male and female)," *Journal of Thermal Biology*, vol. 42, pp. 1–8, 2014.

[78] T. Matsukawa, M. Ozaki, T. Nishiyama, M. Imamura, and T. Kumazawa, "Comparison of infrared thermometer with thermocouple for monitoring skin temperature," *Critical Care Medicine*, vol. 28, no. 2, pp. 532–536, 2000.

[79] O. Airaksinen and M. Narhi, "Reproducibility of infrared thermography measurements in healthy individuals," *Physiological Measurements*, vol. 29, pp. 515–524, 2008.

[80] FLIR Systems, Inc. (2018) Infrared camera accuracy and uncertainty in plain language. Accessed on March 2, 2020. [Online]. Available: https://www.flir.com/discover/rd-science/infrared-camera-accuracy-and-uncertainty-in-plain-language/

[81] C. Evans. (2011) Thermal sensitivity vs thermal accuracy. Accessed on March 2, 2020. [Online]. Available: https://forum.nachi.org/t/thermal-sensitivity-vs-thermal-accuracy/61851/2

[82] M. Mauch, S. Grau, I. Krauss, C. Maiwald, and T. Horstmann, "A new approach to children's footwear based on foot type classification," *Ergonomics*, vol. 52, no. 8, pp. 99–1008,

2009.

[83] J. Rosicky, A. Grygar, P. Chapcak, T. Bouma, and J. Rosicky, "Application of 3d scanning in prosthetic and orthotic clinical practice," 2016.

[84] R. Bibb, D. Eggeer, and P. Evans, "Rapid prototyping technologies in soft tissue facial prosthetics: current state of the art," *Rapid Prototyping Journal*, vol. 16, no. 2, pp. 130–137, 2010.

[85] O. Ciobanu, W. Xu, and G. Ciobanu, *Fiabilitate şi Durabilitate*, vol. 1, no. supplement, pp. 241–247, 2013.

[86] D. L. G. Hill, P. G. Batchelor, M. Holden, and D. J. Hawkes, "Medical image registration," *Physics in Medicine and Biology*, vol. 46, pp. R1–R45, 2001.

[87] J. B. A. Maintz and M. A. Viergever, *An overview of medical image registration methods*. Utrecht University: Information and Computing Sciences, 1998.

[88] V. R. S. Mani and S. Arivazhagan, "Survey of medical image registration," *Journal of Biomedical Engineering and Technology*, vol. 1, no. 2, pp. 8–25, 2013.

[89] G. L. Bichinho, M. A. Gariba, I. J. Sanches, H. R. Gamba, F. P. F. Cruz, and P. Nohama, "A computer tool for the fusion and visualization of thermal and magnetic resonance images," *Journal of Digital Imaging*, vol. 22, no. 5, pp. 527–534, 2009.

[90] M. L. Brioschi, I. Sanches, and F. Traple, "3d mri/ir imaging fusion: a new medically useful computer tool," in *InfraMation*, 2007.

[91] R. F. M. van Doremalen, J. J. van Netten, J. G. van Baal, M. M. R. Vollenbroek-Hutten, and F. van der Heijden, "Infrared 3d thermography for inflammation detection in diabetic foot disease: a proof of concept," *Journal of Diabetes Science and Technology*, 2019.

[92] A. Chromy and O. Klima, "A 3d scan model and thermal image data fusion algorithms for 3d thermography in medicine," *Journal of Healthcare Engineering*, 2017.

[93] C. Rye, R. Wise, V. Jurukovski, J. DeSaix, J. Choi, and Y. Avissar. (2019) Types of skeletal systems. LibreTexts Biology. Accessed on Feb. 16, 2020. [Online]. Available: https://bio.libretexts.org/Bookshelves/Introductory_and_General_Biology/Book%3A_General_Biology_(OpenStax)/7%3A_Animal_Structure_and_Function/38%3A_The_Musculoskeletal_System/38.1%3A_Types_of_Skeletal_Systems

[94] FLIR, *User's Manual FLIR Exx Series*, 2016.

[95] FLIR Systems, Inc., "Flir t650sc 25 degrees (incl. wi-fi)," 2019.

[96] O. T. Imaging, "Microbolometers," Webpage, 2018, accessed on Nov. 13, 2019. [Online]. Available: https://www.optotherm.com/microbolometers.htm

[97] Y. Li, Y. Ma, C. Wei, H. Luan, S. Xu, M. Han, H. Zhao, C. Liang, Q. Yang, Y. Yang, K. E. Crawford, X. Feng, Y. Huang, and J. A. Rogers, "Thin milimeter scale fingernail sensors for thermal characterization of nail bed tissue," *Advances Functional Materials*, vol. 28, no. 30, 2018.

[98] Artec 3D, "Artec 3d scanning applications in healthcare," Webpage, accessed on June 12, 2019. [Online]. Available: https://www.artec3d.com/cases/medical

[99] "Artec space spider," Webpage, Artec 3D, 2019, accessed on June 12, 2019. [Online]. Available: https://www.artec3d.com/portable-3d-scanners/artec-spider

[100] "5 factors influencing radiometric temperature measurments," Webpage, 2016, accessed Feb. 19, 2020. [Online]. Available: http://www.cvl.isy.liu.se/education/undergraduate/tsbb09/lectures/Guidebook_Cores_5_Factors_Influencing_Radiometric_Temperature_Measurements.pdf

[101] A. Richards and T. Hoelter, "Thermal imaging: how far can you see with it?" Webpage, accessed on Feb. 19, 2020. [Online]. Available: https://www.flirmedia.com/MMC/CVS/Tech_Notes/TN_0002_EN.pdf

[102] pulsarnv, "Understanding thermal specifications and features," Webpage, 2018, accessed on Feb. 19, 2020. [Online]. Available: https://articles.pulsarnv.com/index.php/2018/04/25/understanding-thermal-specifications-and-features/

[103] A. Chromy, "High-resolution multispectral 3d scanning and its medical applications," Ph.D. dissertation, 2017.

[104] R. Fernando and M. Pharr, *Octree Textures on the GPU*. Addison-Wesley Professional, 2005, ch. 37.

[105] MathWorks, "Technique to improve performance," Webpage, The MathWorks, Inc., 2019, accessed on Feb. 17, 2020. [Online]. Available: https://www.mathworks.com/help/matlab/matlab_prog/techniques-for-improving-performance.html

[106] MPI, "Rr hut tilt table," Webpage, MPI, accessed on Feb. 11, 2020. [Online]. Available: https://medicalpositioning.com/products/tilt-studies/rr-hut-table/

[107] J. Brownlee. (2019) A gentle introduction to statistical power and power analysis in python. Machine Learning Mastery. Accessed on March 4, 2020. [Online]. Available: https://machinelearningmastery.com/statistical-power-and-power-analysis-in-python/

[108] S. Holmes. (2004) Power and sample size. Standford University. Accessed on March 4, 2020. [Online]. Available: http://statweb.stanford.edu/~susan/courses/s141/hopower.pdf